1/1/2019

THE INFLUENCE OF MECHANICAL CONTRAST ON INDUSTRIAL AND NATURAL HYDRAULIC FRACTURING

REPORTING FOR THE PETROLEUM AND MINING INDUSTRY

Paul J.S.A. van Oosterhout
TECHNICAL UNIVERSITY OF DELFT

The Influence of Mechanical Contrast on Industrial and Natural Hydraulic Fracturing

By

Paul Josephus Segebertus Adrianus van Oosterhout

As fulfilment of

Master of Petroleum Engineering & Reservoir Geology

Commissioned by

Technical University of Delft

&

SCR-Sibelco N.V.

Revision Date: August 22, 2019

Supervisor:	Dr. A. Barnhoorn	– Technical University of Delft Geophysics
Thesis Committee:	Dr. R. Schmitz	– Sibelco NV Mining Engineer
	Dr. Mike Buxton	– Technical University of Delft Mining Engineer
	Dr. A.A.M. Dieudonné	- Technical University of Delft Geo Engineering

I. Preface

The research theme was inspired by geotechnical observations during my Bachelor thesis, where inter-beddings seemed to influence the stability of the quarry slopes. After many phone calls with my Bachelor supervisor Dr. R. Schmitz about the possible influences of inter-bedding, I decided not only to zoom into inter-bedding within one field but also to focus on the effect of inter-bedding in general. The most important reasoning is that soft soil inter-bedding is difficult to prepare for and subject to hydraulic fracturing. I believe that research in either the petroleum as the mining industry will give information on the mechanical boundaries and fluid dynamics to the other industry.

Firstly, I would like to thank Sibelco and my university supervisors Dr. R. Schmitz & Dr. A. Barnhoorn for their vision and guidance throughout the research and report writing. I would also like to thank them for their assistance in acquiring quarry rock and soil samples.

Secondly, I would like to thank my laboratory supervisors, namely Marc, Jens, Martin and Wim by helping me with the sample preparation and experiments.

Lastly, I would like to thank the University of Liege for giving me the opportunity to use their program *Stabilité*.

Many Thanks,

Paul J.S.A. van Oosterhout

Delft
August 5, 2019

II. Abstract

Natural and industrial hydraulic fractures are formed in response to effective stresses on a rock or soil formation. The heterogeneity of layered systems leads to variation in rock or soil mechanical properties, influencing the resistance to failure. A formation breaks by fracture propagation when the effective stress surpasses the formation strength. The propagation of a fracture through a mechanical interface depends on whether the formation strength of the second formation is overcome. This critical effective stress level could be trespassed by high natural or industrial induced pore pressures. Understanding fracture propagation in multi-layered systems with variable pore pressure regimes has important implications and applications to many industries such as quarrying and hydraulic stimulation.

The slope stability of Westerwald Clay Quarries is influenced by inter-bedding of thin sand layers. Surface and slope fractures within the clay formation originated from a high observed hydrostatic head within the sand layers and a reduced confining stress from mining activities. The slopes of the quarry are key in determining the volume of economically mineable clay, these slopes are in turn controlled by the size/extent of fractures and whether they extend through multiple formations. Therefore, ultimate mine planning can be improved by taking the effect of high pore pressures and inter-bedding into account.

This study examines the effect of fracture continuation from sand layers into the stiff Westerwald Clay Formation. The soil parameters (cohesion and friction angle) of the different lithologies within a Westerwald Clay Quarry are determined for slope stability analysis by shearbox testing. Soil classification has been done in terms of plasticity, grain size and mineralogy by Atterberg Limits, Sieving and XRD & XRF respectively.

The results show that fracture initiation within the Westerwald quarries is a combination of mining activities lowering the confining stress and a constant natural hydraulic head. The hydraulic head within the small sand formation lowers slope stability by causing fracture initiation and water infiltration into the clay formation. Slope stabilisation occurs by artificial water pumping or natural water dissipation lowering the hydraulic head. Slope stability is decreased by embankments of low permeability backfill and increased by high permeability backfill.

Due to increasing demand for hydrocarbons, a shift to more complex unconventional reservoir systems for exploration and production can be observed. Inter-bedded systems are common target locations for an unconventional reservoir system. Inter-bedded systems can be found both within source rocks as well as in conventional geological traps. Improvement in recovery from these tight systems often depends on the extent and continuity of fractures through heterogeneous interfaces.

This study examines the propagation and continuity of the fractures in an artificial heterogeneous layered system depending on the mechanical properties of the layers. The fractures will be initiated by hydraulic fracturing in a dried layered system via water injection in a triaxial cell. Fracture propagation is analysed through Micro-CT scans. The mechanical properties such as acoustic wave velocities, unconfined & confined compressive strength and tensile strength are all determined for the analysed layered systems.

The results show that hydraulic fractures initiated within the weakest layer are arrested at the interface between a mechanically weak and strong formation, whereas fractures initiated within mechanically stronger layers prograde through the interface. Hydraulic fractures are initiated when local pressure difference at the interface exceeds the formation's critical tensile stress, the formations critical tensile strength is dependent on the confining pressure.

III. Nomenclature

$A_o =$ initional cross − sectional area (average)
$A = Cross - sectional\ area\ [m^2]$
$B = 0.5 * aparture\ [m]$
$c' = effective\ cohesion\ [kPa]$
$D = sample\ diameter\ [m]$
$E = Young's\ Modulus\ [dimensionless]$
$F_d = Driving\ Force\ (sum)\ [dimensionless]$
$FoS = Factor\ of\ Safety\ (Force)[dimensionless]$
$F_n = normal\ force\ on\ sample\ [kN]$
$F_r = Resisting\ Force\ (Sum)$
$F_s = shear\ force\ [kN]$
$F = Force\ [N]$
$L_o = initial\ specimen\ length\ [m]$
$L = length\ [m]$
$M_c = mass\ of\ container\ [g]$
$M_{cds} = mass\ of\ container + oven\ dry\ specimen\ [g]$
$M_{cms} = mass\ of\ container + moist\ specimen\ [g]$
$M_d = Driving\ Moment\ (sum)[dimensionless]$
$M_r = Resisting\ Moment\ (Sum)[dimensionless]$
$M_s = Mass\ of\ oven\ dry\ specimen\ [g]$
$M_w = Mass\ of\ water\ [g]$
$m = mass\ of\ the\ sample\ [kg]$
$m = weigth\ [kg]$
$p_0 = pressure\ at\ Z = 0\ [Pa]$
$p_L = pressure\ at\ Z = L\ [Pa]$
$P = applied\ load\ [kPa]$
$Q = flow\ [\mathrm{m^3/sec}]$
$Re = Reynolds\ number\ [-]$
$R = inner\ radius\ [m]$
$u = pore\ pressure\ [kPa]$
$V_b = bulk\ volume\ [\mathrm{m}^3]$
$V_{ma} = volume\ of\ the\ matrix\ [m^3]$
$V_p = compressional\ wave\ velocity\ \left[\frac{m}{s}\right]$
$V_s = shear\ wave\ velocity\ \left[\frac{m}{s}\right]$
$v = Poisson's\ Ratio\ [dimensionless]$
$W = width\ [m]$
$\varepsilon_1 = axial\ strain\ [dimensionless]$
$\rho_b = bulk\ density\ \left[\frac{kg}{m^3}\right]$
$\rho_{ma} = density\ of\ the\ matrix\ \left[\frac{kg}{m^3}\right]$
$\rho = density\ [kg/m^3]$
$\sigma' = effective\ stress\ [kPa]$
$\sigma_a = axial\ stress\ [kPa]$
$\sigma_c = true\ compressive\ strength\ [kPa]$
$\sigma_n = nominal\ normal\ stress\ [kPa]$
$\sigma_{normal} = normal\ stress\ [kPa]$
$\sigma_t = true\ tensile\ stress\ [Pa]$
$\tau_a = axial\ strain\ [dimensionless]$
$\tau_f = drained\ shear\ strength\ [kPa]$
$\tau = nominal\ shear\ stress\ [kPa]$
$\varphi' = internal\ friction\ angle\ [dimensionless]$
$\phi = porosity\ [-]$
$\mu = viscosity\ [Pa * s]$

Contents

1 Introduction

Extraction of minerals from Earth has been an ongoing process since the history of civilisation. Industrial advancement increases the ability of extraction and demand for minerals and hydrocarbons until today. The quote "*if you cannot grow it, it has to be mined"* is and will be true to future dates, since the ultimate origin of recycled mineral- and hydrocarbon-based materials are within the Earth, (Ellen Macarthur Foundation, 2013). Easiest and most profitable resources are depleted first, leaving recourses that are more challenging and less profitable to extract for our future (generations). As a result, the simplified homogenous rock and soil mechanical models will be less applicable for upcoming petroleum and mining engineering projects (Ellen Macarthur Foundation, 2013).

Natural and industrial hydraulic fractures are formed in response to effective stresses on a rock or soil formation. Effective stress is the net stress acting on a soil or rock by subtracting the pore pressure from the total stress, (Terzaghi, 1925). The heterogeneity of layered systems leads to variation in rock or soil mechanical properties, influencing the resistance to failure. A formation breaks by fracture propagation when the effective stress surpasses the formation strength. The propagation of a fracture through a mechanical interface depends on whether the formation strength of the second formation is overcome, (Regelink, 2018). This critical effective stress level could be reached by high natural or industrial induced pore pressures. Understanding fracture propagation in multi-layered systems with variable pore pressure regimes has important implications and applications to many industries such as quarrying and hydraulic stimulation.

An increase in German Westerwald clay production for the ceramic industry due to the newest techniques, machinery and moderate offering of high-quality ceramic clay can be observed since 1600 till today, (Kuntz, 1996). Slope stability simulations and mine planning increased the total amount of obtainable clay. As a result, a new interest in earlier not profitable and abandoned quarries and exploration was awaken. Modern slope simulations prove a stable and safe quarry environment. Nevertheless, surface and slope cracks (Figure 1) are observed within the Westerwald clay quarries. Thin inter-bedded sand clusters are observed in Cone Penetration Tests (CPT) data, as an observed high-pressure head in the boreholes for Inclinometer measurements.

Figure 1: Extreme Large Slope Crack Observation in the Christel Nord Quarry of Sibelco within the Westerwald

These pressured inter-beddings are not taken into account in modern slope simulations. The possibility that slope and surface cracks originate from a high hydraulic head pressures penetrating a mechanical boundary may be an important parameter for slope stability simulations. The fracture can be initiated within the Westerwald quarries as a combination of mining activities lowering the confining stress and a constant natural hydraulic head. Understanding of the influence of these parameters in respect to fracture formation is crucial for an ultimate mine planning.

The well-documented challenging Kimmeridge Clay Formation has generated oil and gas that, once expelled, migrates to accumulate in carbonate and sandstone reservoirs, (Munira, et al., 2015). Not all hydrocarbons will migrate out, a high percentage will remain in the source rock itself. Due to an increasing demand for hydrocarbons, a shift to more complex unconventional reservoir systems for exploration and production can be observed. Inter-bedded systems are common target locations for an unconventional reservoir system. The shale source rocks are low granular permeable fine-grained rocks, which were naturally fractured by the generation of large fluid pressures due to oil and gas formation. The natural fractures might be sealed-off by depositional processes and thus will contain organic-lean sandstone and siltstone inter-bedding within the source rock, forming a tight reservoir, (Turcotte, et al., 2016). Modern hydraulic fracturing reopens these fractures or creates new ones. Some of the key points for these unconventional systems are its storage capacity, thickness, recoverability and the possibility of capturing non-expelled hydrocarbons in the inter-bedded formation, (Munira, et al., 2015).

A difference between traditional and modern hydraulic fracturing, exist in terms of lithology as can be observed in Figure 2. In the case of traditional fracturing, a sandstone reservoir lies in an anticlinal fold below a low permeable seal. A vertical well is drilled into the sandstone reservoir and a hydraulic fluid with additives is used for fracturing. Modern fracturing;, the hydraulic fluid is pumped down in a horizontal production well within the tight inter-bedded strata allowing numerous fracturing injections to take place. A fluid with a low resistance to flow will create a large distribution of hydraulic fractures. Both fracturing techniques use a sand proppant to keep the fractured medium open and enable gas and oil to migrate out through this network (Turcotte, et al., 2016). For the oil & gas industry, the degree of improvement depends on the continuation of fractures.

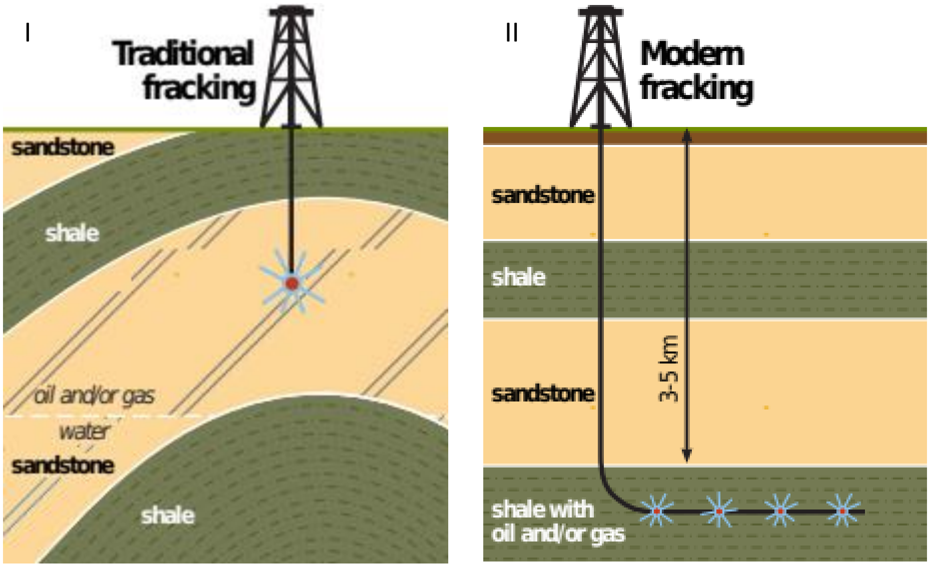

Figure 2: Traditional hydraulic fracturing (I) and Modern Hydraulic Fracturing (II), (Turcotte, et al., 2016). The Borehole is visualised by the Straight Black Line. Fracture initiation is visualised by the Blue Lines oriented in a Star-Like Shape. High hydraulic Pressures are visualised by the Red Dot within the Blue Star.

That said, for engineers originating from the petroleum as mining world, the following question might arrive: is it possible for a pressured regime within a tight or permeable formation to initiate a fracture throughout its mechanical interface boundaries? By pressurising formations, fractures can form and penetrate different lithologies. If such a fracture stops at the lithology transition depends on the mechanical properties and confining stress of the different lithological units. A high modulus material is related to a strong material with a high young's modulus value that defines the stiffness of a solid material. Generally, fracture propagation starts at low-modulus material and penetrates towards high-modulus material. The fracture can either propagate through or break at its interface, depending on the confining stress and mechanical properties, (Regelink, 2018).

The effect of induces pore pressure differences within the formation of interest due to a natural or industrial increased hydraulic head is one of the parameters that can advance soil and rock mechanical models. A pressure difference/hydraulic head can result in natural or induced hydraulic fracturing both in rock and soil formations. Hydraulic fracturing in soil types within a laboratory setup is possible, whereas imaging of the fracture propagation is difficult. Rock formations will fail at higher induced hydraulic pressures, whereas the imaging of the fracture propagation is easier due to a more fixed position of the grains.

This study examines the propagation and continuity of the fractures in an artificial heterogeneous layered system depending on the mechanical properties of the layers. The fractures will be initiated by hydraulic fracturing a dried layered system via water injection in a triaxial cell. Fracture propagation is analysed through Micro-CT scans. The mechanical properties such as acoustic wave velocities, unconfined & confined compressive strength and tensile strength are all determined for the tested layered systems.

The aim is to generate a better understanding of fracture propagation of inter-bedded systems for the mining and petroleum sector by studying the mechanical properties in laboratory setup by creating local stress differences. A second aim is to use the results on fracture propagation of an inter-bedded laboratory setup to update the inter-bedded Westerwald quarries by implementing a slope stability analysis with obtained geotechnical and mechanical data. The mechanical soil parameters cohesion and friction angle of the different Westerwald lithologies are determined by shearbox testing. Soil classification has been done in terms of plasticity, grain size and mineralogy by Atterberg Limits, Sieving and XRD & XRF respectively.

2 Method and Materials

This chapter describes the area of sampling, geotechnical observations, geology, sample preparation and methodology.

2.1 Sampling Area for Westerwald Clay Specimen

The Sibelco quarries in the Westerwald region of Germany has been taken as the sampling location for inter-bedded formations. The choice of the location has been determined based on geological setting, hydrology and geotechnical influence of the inter-bedded system. Figure 3 shows the exact sample locations (red dots) with Delft as a reference location (blue dot).

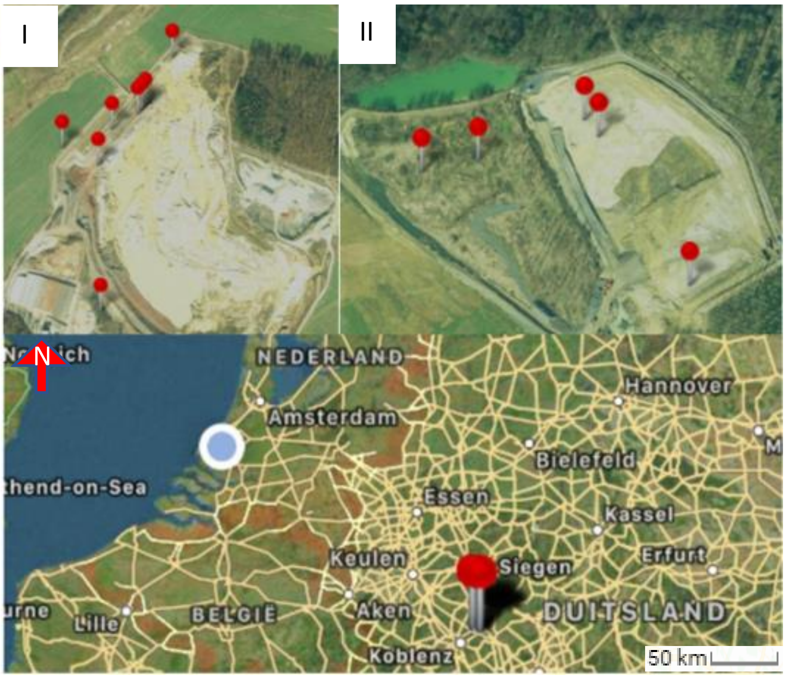

Figure 3: Field Sampling Locations of the Stemmer (Figure I) and Lieblich III (Figure II) Quarry

Figure 4 visualises Sibelco's Stemmer quarry in greater detail. The red dots in Figure 4 (I) visualises the sample location from above. The green rectangle shows the angle of view. Figure 4 (II) shows the side view, where A till E denotes the specific sample locations. Figure 4 (A till E) shows a close-up image of the gathering spot referenced by numbering 001 until 009 to the processed specimens. A description of the samples in terms of colour, hardness, brittleness and coarseness can be found in Appendix D – Sample Specification.

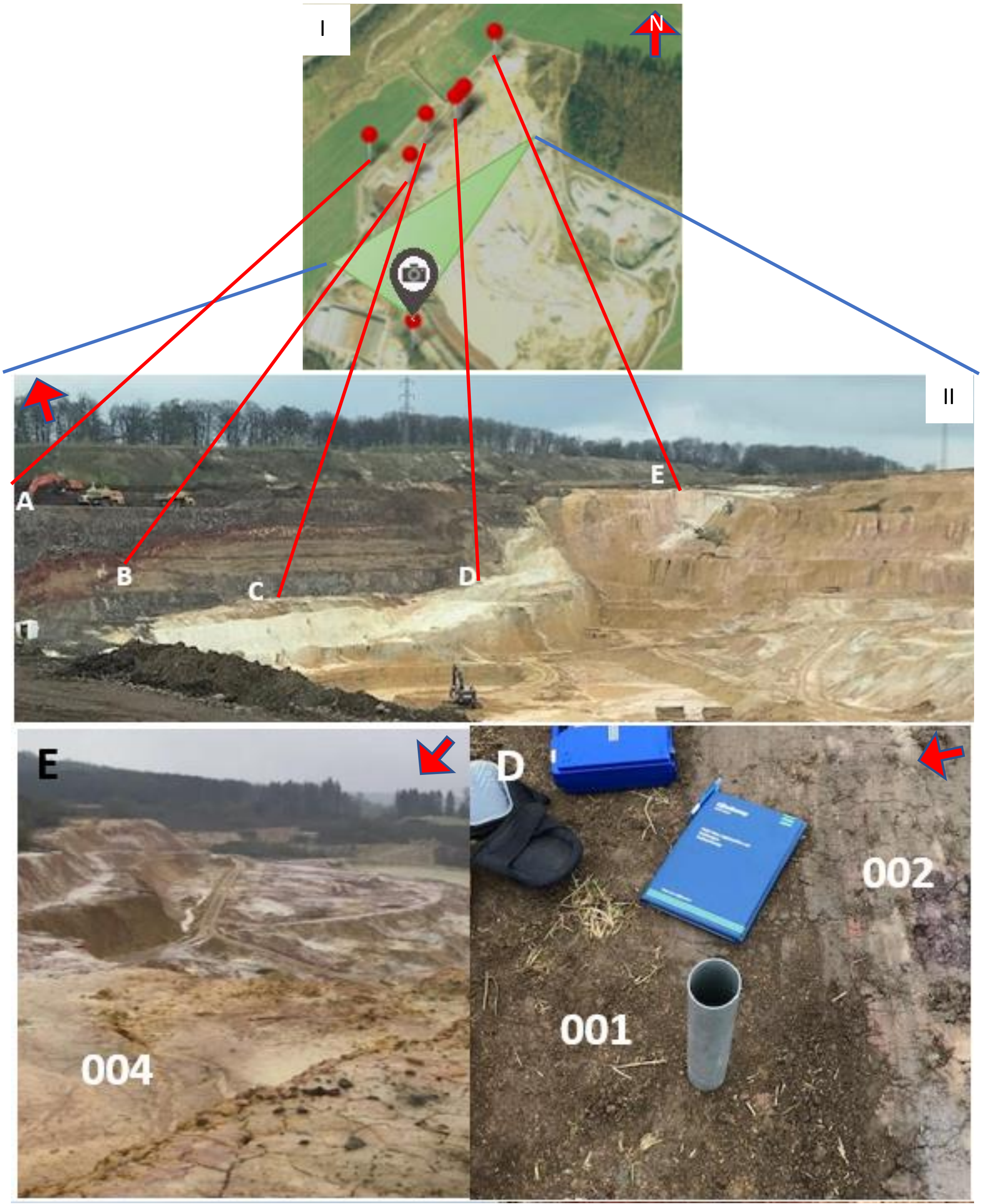
I
N
II
A
B
C
D
E
E
004
D
002
001

Figure 4: Sample Location within the Stemmer Quarry, (I) shows the Topview

2.1.1 Geological Setting

The geological and structural development of the Westerwald area is closely related to the Harz Mountains during the Variscan Orogeny[1]. The compressive regime uplifted and folded the Devonian and Carboniferous rocks. Hills and basins were formed, especially those basins are of great importance for the clay resources found today. The basins abled the deposition of sediments (Sibelco Deutschland GmbH, 2013).

The supercontinent began to break up between 50 and 60 million years ago. Volcanic activity increased significantly within Europa. The Westerwald region was no exception, Vulcans pinched through the deposited sediments and covered it by volcanic material. This volcanic tuff and basalt protected the sediments from erosion and are the reason why these sediments can still be found today (Sibelco Deutschland GmbH, 2013). Due to the pressure of the volcanic material, the clays are over-consolidated[2].

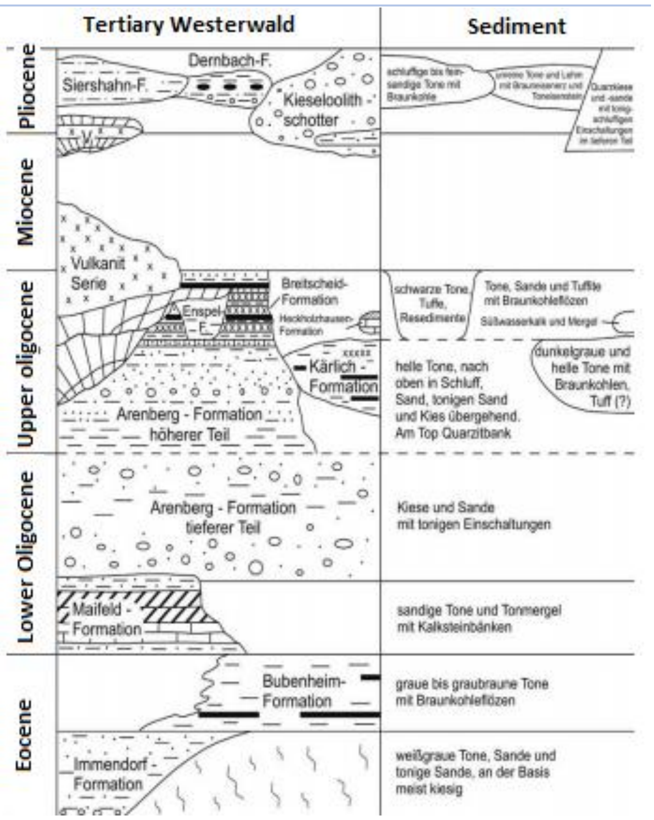

Figure 5: Geological & Structural Development of the Westerwald, (Sibelco Deutschland GmbH, 2013).

The Sibelco clay mines are composed of different clay types, which differ in terms of colour, chemical & structural properties and grain size. The value is mainly depending on the chemical properties, whereas the geotechnical aspect is mainly influenced by the structural property and grain size. This section focusses mainly on the geotechnical aspect influenced by an inter-bedded formation as a result of a change of grain size. The deposition of very fine and coarser sediments in the past is related to the difference in depositional energy.

2.1.2 Hydrological Setting

Earlier research by G.U.B. Ingenieur AG concluded that there is no available evidence of a continuous water table throughout the Sibelco Quarries due to low permeability clay barrier. Although a continuous water table cannot be found, the existence of a difference in pressure head within the Hohewieße quarry is visualised through inclinometer boreholes (G.U.B. Ingenieur AG, 2011). The difference in pressure head originates from thin confined inter-bedded sand aquifers pressured by compression. As a result, a piezometric surface[3] has been established. The water level in the

[1] The Variscan Orogeny took place during the late Palaeozoic geological period. This time period ranges from 390 to 300 million years ago. Especially the late Devonian and early Carboniferous phase of the orogeny are determined for the Westerwald and Harz region.

[2] Over-consolidation is the process where the sediment has experienced higher stress than the current state of stress. This process is mainly deterministic for the hydrological setting.

[3] An imaginary surface defining the water level a confined aquifer would rise to if it would have been pierced by wells. This surface normally lies above the layer's surface.

inclinometer is found at 305 metres, a hydraulic head difference of 33 metres is found at a pit depth of 272 metres. A water column of 33 metres equals to a pressure head of around 3.2 bar.

Rock mass will have surface and body forces. Body forces are essentially mainly related to gravity, whereas surface forces are caused by stresses from the surroundings. A model can be obtained taking the simplest way of describing a characteristic or manner and make it more complicated by adding exceptions and or characteristics. By assuming a perfect cube, three stress vectors are acting on the three planes of the cube. Each perpendicular to each other. Knowing these three stress vectors, a determination on the stress vector on the generated plane inside of the rock mass body can be made (Bertoti, 2018). An adjustment of this stress model to the factor of safety was offered by the University of Liege.

Inter-bedding does not affect the surrounding as long the stress conditions do not change; a harmonious system. However, with removal or addition of stress, the system starts to readjust to a new equilibrium. Figure 6 shows an inter-bedded sandy layer between clay surroundings, red and blue arrows are indicating three major stress vectors assuming sigma two and three are equal. Pore pressures are indicated by blue arrows, while the red arrows indicate the total stress exposed to the layer. As observed by Inclinometers in one of the Westerwald quarries, the more permeable layer holds a higher pore pressure.

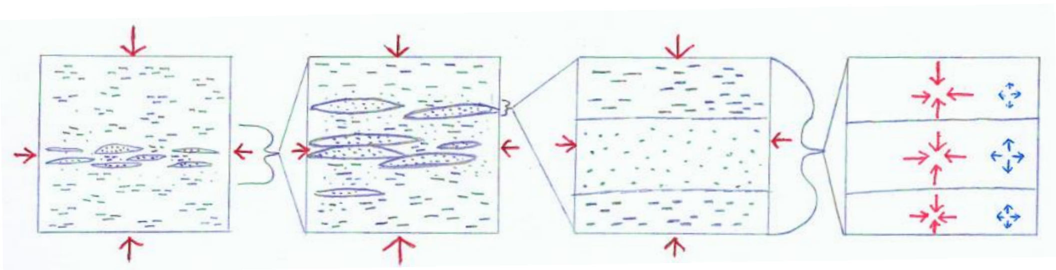

Figure 6: Inter-bedded Formation in Equilibrium

By removing soil, as in the Sibelco Lieblich III quarry, the stress conditions inside the subsurface change and start to readjust itself. A landslide in the slopes of the quarry was the result of this readjustment, as can be observed in 2.1.1 Geotechnical observations. All landslides originate from material failure as a result of gravitational forces moving material to a more stable position. Resistance against this movement can be expressed by the theory of Mohr-Coulomb by materials' shear strength (Skels & Bondars, 2015). Figure 7 shows the stress readjustment of the Lieblich quarry. A sandy clay inter-bedded formation has been found at the point of interface.

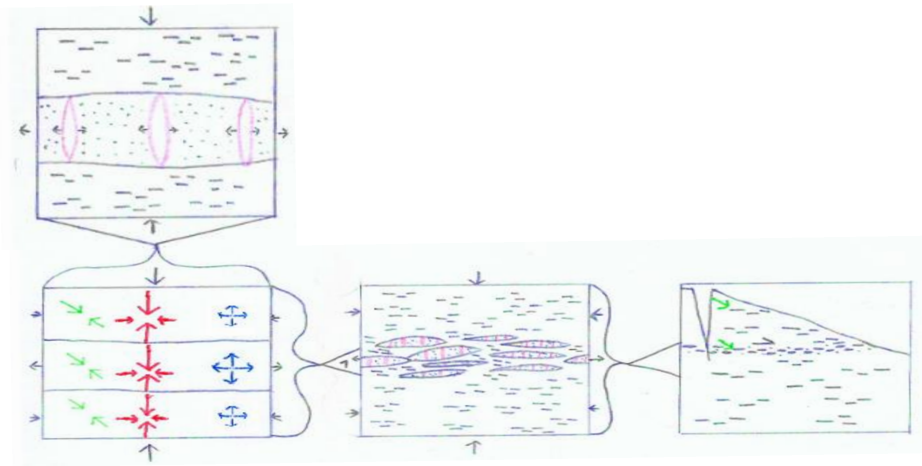

Figure 7: Stress readjustment. Green Arrows; Shear Stress, Red Arrows; Total Stress. Blue Arrows; Pore Pressure.

2.1.1 Geotechnical observations

After the slope failure occurred within the Lieblich III quarry of Sibelco during the dry summertime, a water holding layer could be observed which felt sandier between the fingers. A cracked open surface was observed as well. These observations are shown in Figure 8 on the left and right side respectively. Layer A has been sampled during summer condition and winter conditions, whereas layer B only could be sampled during summer conditions just after failure.

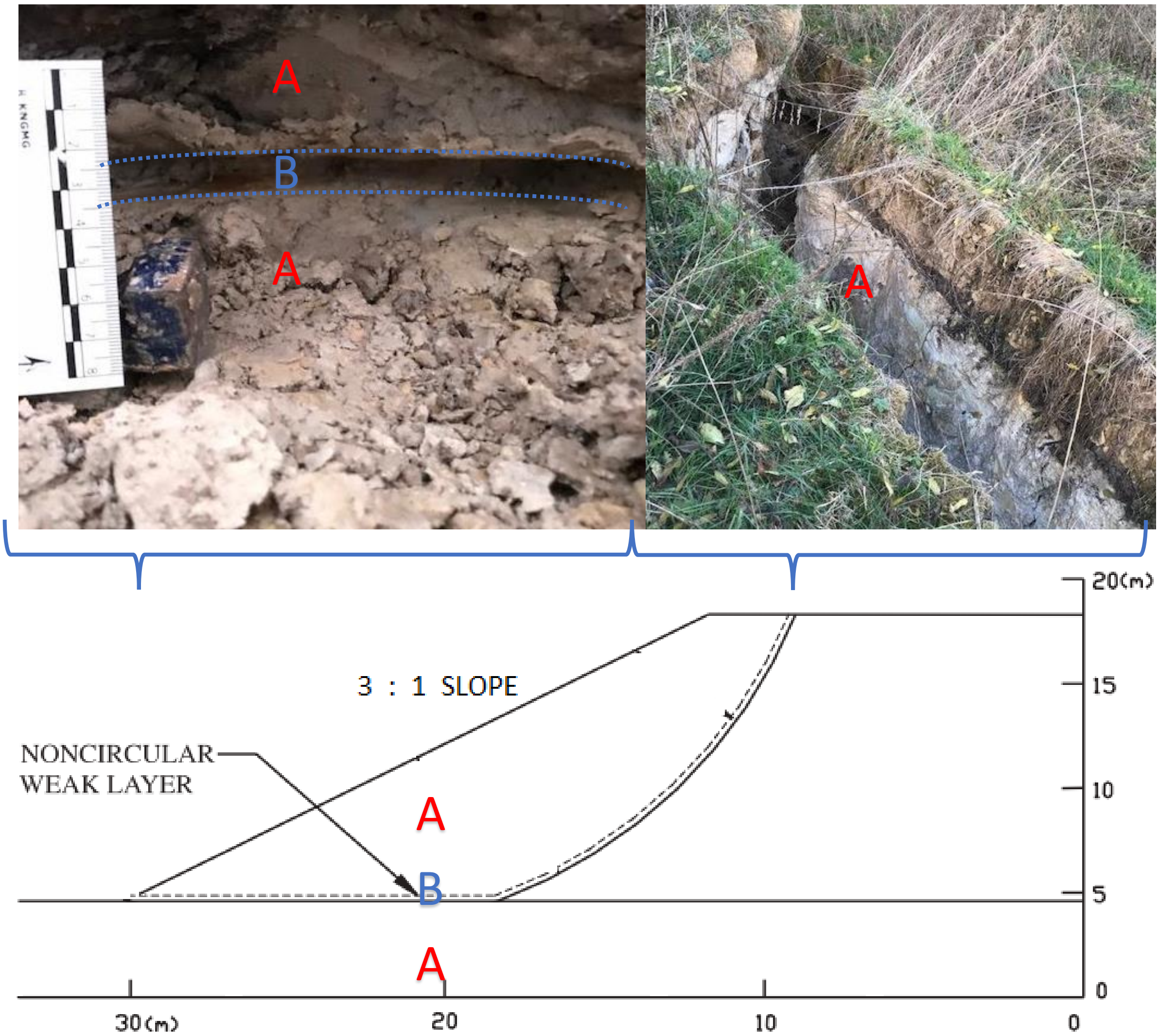

Figure 8: Geotechnical observations in the Lieblich III quarry

A non-circular slip failure resulting from weak layer could be simulated by Janbu's Simplified method, where only the overall horizontal force equilibrium is considered or by the Bishop's method (Zuyu, et al., 2011). The method of Janbu is similar to Bishop's Simplified method except that Bishop satisfies overall moment equilibrium and considers normal interslice forces while ignoring interslice shear forces. Both methods ignore the lambda parameter. The lambda parameter is a soil constant, describing the appropriate compressibility index of the soil. The factor of safety obtained by Janbu's method is underestimated in comparison to Bishop (GEO-SLOPE International, 2012). Bishop's method has been chosen since environmental and human risks are already taken into account within the factor of safety.

2.2 Sample Preparation

Soil specimens of the Westerwald clay quarries have been used to determine the mechanical soil parameters cohesion and friction angle for slope stability analysis by shearbox testing. Soil classification on these samples has been done in terms of plasticity, grain size and mineralogy by Atterberg Limits, Sieving and XRD & XRF respectively.

A remoulded oven-dried sample LI006 and LI007 of the Lieblich III quarry were created to measure UCS and acoustics. Clay was remoulded to a sample of approximately 9 and 4.5 centimetres in length and diameter respectively, whereas the wet alternation has been remoulded to 8 and 4 centimetres sample. A ratio of 1:2 in terms of diameter to length have been used as prescribed by the American Society for Testing and Materials (ASTM). Both samples have been sanded with 125 µm grit to obtain straight and equal surfaces.

To investigate the degree of continuation of the fractures in an artificial heterogeneous layered system, four difference lithologies are sampled. These layered systems consisted of 10 different configurations (Table 1) are fractured by hydraulic water injection in a triaxial cell. The fractured samples will be scanned with a Micro-CT scanner. The mechanical properties such as acoustic wave velocities, unconfined & confined compressive strength and tensile strength will be determined to conclude the mechanical contrast between the tested layered systems.

Large not-fractured rock fragments were cored in 29.7 millimetres diameters samples by a hydraulic water-cooled drill. A prescribed diameter-length ratio of 1:2 has been used, where the diameter is set to equipment dimensions minus two times the plastic sleeve thickness (ASTM International, 1995). A diamond blade cut the specimen into samples of 60 and 20 millimetres in length. Three 20 millimetres samples were combined to fulfil as a synthetic layered sample for educational purpose, whereas the mono-lithologic 60 millimetres sample were used for referentially and characteristically purpose. To exclude roughness as a parameter and obtaining straight surfaces with a 90-degree angle to the length, samples were sanded with a 125 micrometres grit. Moisture content is excluded as a parameter by oven drying the samples at fifty degrees Celsius for at least 24 hours. All cored and cut specimens are measured on matrix density to exclude or include porosity as a parameter.

The 17 experimental synthetic layered samples were established by three ±20 millimetres samples of which the bottom and top one originates from the same rock type. The contrast ratio between the middle and outside rock samples in term of tensile stress will be called "Mechanical Contrast" (M.C.). The synthetic layered configuration is a possible combination of four different lithologies as visualised in Table 1 and Figure 9.

Figure 9: Synthetic Layered Samples used for CCS Water Injection.

Table 1: Configuration of Synthetic Layered Samples. HFB: High Porosity Fontaine Bleau Sandstone, LFB: Low Porosity Fontaine Bleau Sandstone, AIN: Ainsa Sandstone, BEN: Bentheimer Sandstone, M.C.: Mechanical Contrast.

Layer 1	HFB	HFB	AIN	AIN	LFB	LFB	LFB	AIN	HFB	BEN
Layer 2	LFB	AIN	BEN	LFB	BEN	HFB	AIN	HFB	BEN	AIN
Layer 3	HFB	HFB	AIN	AIN	LFB	LFB	LFB	AIN	HFB	BEN
M.C.	2.25	3.7	0.3	0.6	0.4	0.4	1.6	0.3	1	3.7
Tested Amount	1	2	2	3	2	2	1	1	2	1

2.3 Test Descriptions

Several tests are carried out to obtain rock and soil mechanical parameters and soil conditions at testing.

2.3.1 Dimensional Parameters

Dimensional sample sizes are measured three times with a calliper and averaged to increase the accuracy to the range of ± 0.05 millimetres. Samples are measured in height and diameter for the volumetric bulk (Equation 1) & density calculations (Equation 2).

$$V_b = \pi * \left(\frac{D}{2}\right)^2 * L \tag{1}$$

$$V_b = bulk\ volume\ [m^3]$$
$$\mathrm{D = sample\ diameter\ [m]}$$
$$\mathrm{L} = length\ [m]$$

$$\rho_b = \frac{m}{V_b} \tag{2}$$

$$\mathrm{\rho_b = bulk\ density\ [kg/m^3]}$$
$$m = weigth\ [kg]$$

In order to define the porosity of every individual rock sample, a "*Quantachrome ultrapycnometer 1000*"[4] has been used. This device determines porosity by making use of helium gas injection at a set temperature of 27.0 °C. The volume of gasses are in a relationship with the temperature, therefore the device is turned on one hour before testing for an acceptable accuracy. The accuracy is in the range of 0.03% if the sample volume is exceeding 50% of the cell volume, (Quantachrome Corporation, 2019). The porosity can be determined by volumetric density (Equation 3) and matrix density (Equation 4).

$$\rho_{ma} = \frac{m}{V_{ma}} \tag{3}$$

$$\rho_{ma} = density\ of\ the\ matrix\ [kg/m^3]$$
$$\mathrm{m = mass\ of\ the\ sample}\ [kg]$$
$$\mathrm{V_{ma}} = volume\ of\ the\ matrix\ [m^3]$$

$$\phi = \frac{V_b - V_{ma}}{V_b} \tag{4}$$

$$\phi = porosity\ [-]$$
$$\mathrm{V_{ma}} = volume\ of\ the\ matrix\ [m^3]$$
$$\mathrm{V_b} = volume\ of\ the\ bulk\ [m^3]$$

Bulk volume and mass were determined by hand measurements. Density and matrix volume are determined by a the Quantachrome ultrapycnometer 1000. The principle of determination of matrix volume is based on the law of Boyle. This special case of the ideal gas law states that a constant volume of an injected gas in a known volumetric cell has a different pressure than when an object is placed within this known volumetric cell. The volumetric matrix of the placed objected is calculated by the change in pressure since helium occupies and pressurizes the matrix pore space.

2.3.2 Acoustic Measurements

Ultrasonic compressional and shear wave travel times are material's characteristic. Shear wave transducers and receivers were used. Within the shear wave, the compressional wave is visible.

[4] The Quantachrome ultrapycnometer 1000 is the property of the laboratory of CITG faculty of TU Delft.

However, if the compressional wave could not be visible, transducers and receivers were changed for compressional ones. A Yokogawa oscilloscope visualizes the propagating waves. The obtained data was saved and reconstructed in Matlab (Figure 10), for accuracy improvement. Figure 10 shows the first acoustic response of compressional wave origin and a second response from shear wave origin. The compressional and shear wave velocities have been used to characterize the dynamic Poisson's Ratio of the material, Equation 5.

$$v = \frac{1}{2} * \frac{(V_p^2 - 2V_s^2)}{(V_p^2 - V_s^2)} \tag{5}$$

$$V_p = compressional\ wave\ velocity\ \left[\frac{m}{s}\right]$$
$$V_s = shear\ wave\ velocity\ \left[\frac{m}{s}\right]$$
$$v = Poisson's\ Ratio\ [dimensionless]$$

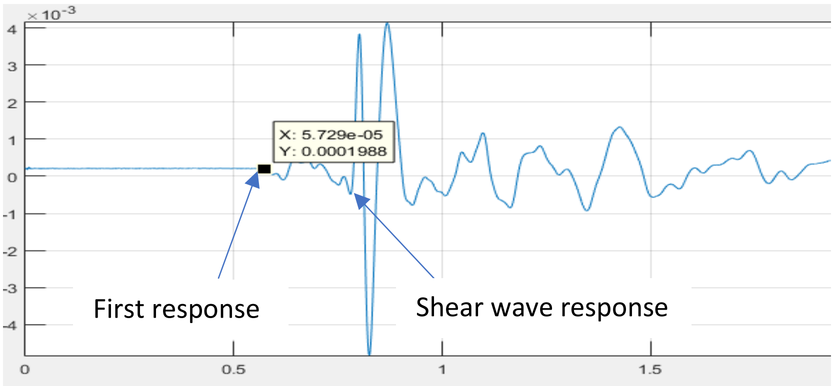

Figure 10: Reconstruction of Ultrasonic Compressional and Shear Waves by Shear Wave Transducers and Receivers

2.3.3 Atterberg Limits by Penetrometer

Atterberg limits are primarily based on the measurement of critical water contents of clayey soil separated in the liquid and plastic limit. As the term says, the liquid limit can be defined by the change of plastic to liquid behaviour at an increased water content, whereas the plastic limit can be defined as the lowest limit the specimen behaves plastic (Bardet, 1997). The liquid limit was determined by the Control's Penetrometer test, where different water contents [ratio] and related compressibility [mm] are measured and plotted. The test is fulfilled at least four times, with two measurements below, one around and one above a penetration of 20 millimetres, to have a satisfying data density for the line fit. The penetrometer is dropped per moisture content until a compressibility difference of fewer than 0.5 millimetres is observed. The penetration measurement has a precision of 0.01 millimetres (Controls Group, 2019). The liquid limit will correspond to the water content related to a compressibility of 20 millimetres by trend line plotting (Tanzen, et al., 2016). The plastic limit is obtained by rolling at least 30 grams of clay to a diameter of 3 millimetres until it starts to crumble (ASTM International, 2000).

Primarily use of the test is to characterise clay based on the plasticity chart[5], correlation to other clays can be established on this chart (Oosterhout, 2017). A plasticity index is characterized by an upper and lower bound (Equation 6), a value towards zero corresponds to a more non-plastic specimen, whereas a value towards 17 can be defined as a plastic specimen (Bardet, 1997).

$$Upper\ bound\ plasticity\ index = 0.9 * (liquid\ limit - 8) \tag{6}$$
$$Lower\ bound\ plasticity\ index = 0.73 * (liquid\ limit - 20)$$

[5] Basic soil types could be distinguished by the Atterberg limit, a plasticity chart with the liquid limit on the x-axis and the plasticity index on the y-axis visualizes those basic soil types clearer.

2.3.4 Consolidation

Consolidation determines the rate and magnitude of consolidation of sandy clay during lateral restrainment and axial drainage, while applied controlled stress loads the system. Each stress load is maintained until all excess pore water pressures are dissipated. Measurements in terms of changes in specimen height at different times are made during consolidation, to determine the effective stress and void ratio relationship (ASTM International, 2014).

Test results are depended on the magnitude and duration of the applied load. This procedure is valid for the disturbed and undisturbed specimen. Fulfilling the test, the soil has to be saturated and therefore exhibit homogenous properties. Consolidation of the soil is measured continuously in vertical height difference and time by a shearbox apparatus. Change in vertical height is plotted against time in square root. Consolidation is observed as stabilization of height (Figure 11).

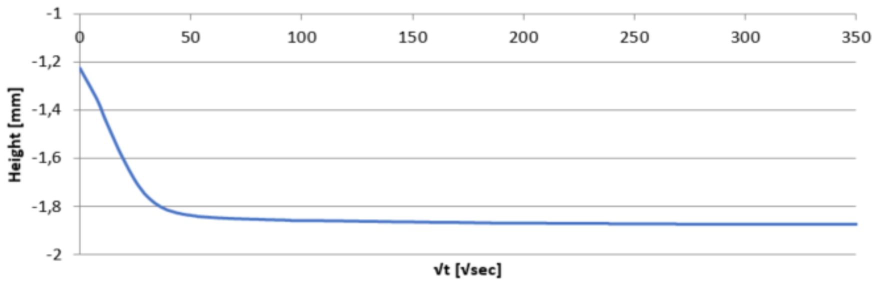

Figure 11: Consolidation Curve of Sample 006 by a Normal Load of 15 Kg or 50 kPa

2.3.5 Grain size distribution by sieves and Hydrometer

Particle-size distribution was obtained by separating particles into size ranges and determining quantitatively the mass in those ranges. Sieves have been used from 0.6 millimetres until a sieve size of 0.063 and 0.054 millimetres for sample Li007 and Li006 respectively. Both samples have been sieved wet. A total mass of 100 gram was sieved through 0.6, 0.3, 0.15, 0.125, 0.054 and 0.063 millimetres grid. A hydrometer test was carried out at sample Li007 since less than 50% mass was retained after sieving.

A hydrometer test is carried out at 50 gram of specimen covered with 125 millilitres of sodium hexametaphosphate. The soaked specimen is dispersed further by a stirring apparatus for at least 1 hour of stirring. A glass sedimentation cylinder is filled with the dispersed sediment and filled with demineralised water till 1000 millilitre. A Second cylinder is filled with 125 and 875 millilitres of sodium hexametaphosphate and demineralised water respectively to ensure accuracy. Hydrometer measurements are taken at 0.5, 1, 2, 4, 8, 30, 120, 480 and 1440 minutes, (ASTM International, 1998).

2.3.1 Moisture Content

The mass of the container without a specimen, including a moist specimen and an oven-dried specimen is measured three times and recorded within two decimals. The specimens are dried at a temperature of 105 degrees Celsius. The water content ratio of the specimen is calculated by the measured masses as stated in Equation 7, (ASTM International, 2014):

Equation 1: Moisture Content of the specimen

$$water\ content\ [\%] = \left[\frac{M_{cms} - M_{cds}}{M_{cds} - M_c}\right] * 100 = \left(\frac{M_w}{M_t}\right) * 100 \qquad (7)$$

$$M_{cms} = mass\ of\ container + moist\ specimen\ [g]$$
$$\mathrm{M_{cds}} = \text{mass of container + oven dry specimen } [g]$$
$$\mathrm{M_c} = mass\ of\ container\ [g]$$
$$M_w = mass\ of\ water\ [g]$$
$$M_s = mass\ of\ oven\ dry\ specimen\ [g]$$

2.3.2 Shearbox Apparatus

Shearbox tests are performed three or more times per sample, each test is done under a different normal load. Several tests are required to determine the Mohr strength envelope (ASTM International, 2014). The rate of displacement is taken to be 0.02 mm/min. Lieblich III and Hohewieße block samples are taken by a hammer & chisel and cut into cylinders with a 63 mm diameter. The stronger and more brittle Stemmer samples are gathered by a heavy sampling ring kit E of Eijkelkamp with an internal diameter of 50 mm, (Eijkelkamp, 2019). The Lieblich and Hohewieße samples have been carried-out on a 63 mm mould, whereas the Stemmer samples are carried-out on a 50 mm mould. The sample's lengths are between two to three centimetres.

The red Hohewieße overburden has been carried-out on two different average densities, namely $1.440 * 10^3$ and $1.660 * 10^3\ \mathrm{kg/m^3}$. The lower and higher remoulded density specimen is created by putting lose saturated overburden into the shearbox and adding a normal force of 1018 Kilo Newton for approximately 10 minutes and 3545 Kilo Newton for approximately 3 hours respectively. Five different stages in the stress envelope could be distinguished during the test, namely:

- **Failure** – Stress condition at failure, often this is the maximum shear stress.
- **Nominal Normal Stress** – The applied normal force over the shear box area.
- **Nominal Shear Stress** – The applied shear force over the shear box area.
- **Relative Lateral Displacement** – The ratio of soil displacement to the lateral dimension.
- **Pre-shear** – state of the specimen after stress stabilisation due to consolidation.

The test is suited for remoulded or intact specimens. Rotation of principal stresses occurs during the test. The nominal shear stress per stage can be calculated by a series of calculations (Equation 8 & Equation 9), (ASTM International, 2014):

$$\tau = \frac{F_s}{A} \tag{8}$$

$$\tau = nominal\ shear\ stress\ [kPa]$$
$$\mathrm{F_s} = \text{shear force [kN]}$$
$$\mathrm{A} = Cross - sectional\ area\ [m^2]$$

$$\sigma_n = \frac{F_n}{A} \tag{9}$$

$$\sigma_n = nominal\ normal\ stress\ [kPa]$$
$$\mathrm{F_n} = \text{normal force on the sample [kN]}$$

2.3.2.1 Rate of Displacement of the Shearbox Apparatus

Rocks and soils will dilate or compress during shear stresses, during dilation and compression the shear zone is subjected to a net inflow and outflow of water respectively. If the permeability is high enough, this process will be rather quick. At low permeable formations, this process could take months or weeks. Depending on the ability for water to move in or out of the shearing zone, a drained or undrained shear strength can be observed for short or long term periods (Frederick University, 2017).

Figure 12 shows the shear stress characteristics of undrained and drained formations. It can be concluded that a very impermeable formation will not shear until the deformation stress is surpassed. A change in the pore water pressure inside the permeable formation will affect the shearing and breaking stress by the following formula proposed by Karl von Terzaghi in 1925:

$$\sigma' = \sigma_{normal} - u \tag{10}$$

$$\sigma' = effective\ stress$$
$$\sigma_{normal} = normal\ stress$$
$$u = pore\ pressure$$

Figure 12 shows the effect of the displacement rate in terms of a drained and undrained shearing test. An undrained shearing test (I), experiences no volume change and an increase in pore pressure respectively to the increase in total normal stress. Whereas a drained shearing test (II), experiences volume changes and an increase in effective stress.

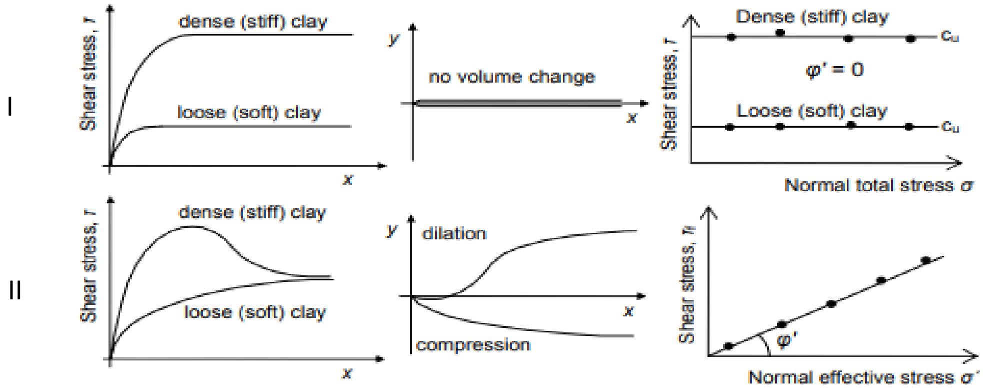

Figure 12: (I) Undrained Shear Box (II) Drained Shear Box Test (Frederick University, 2017)

As mentioned earlier a certain time is needed for the sample to reach the equilibrium stress state. It has been found that an increase in shear rates on over-consolidated clays higher than 100 mm/min results in a loss of strength up to 60%. This loss of strength can be linked to complex shearing features due to the incapability of water dissipation, (Li, et al., 2017). The rate of displacement has been taken 0.02 mm/min, which is way lower than 100 mm/min, to ensure drained behaviour without complex shearing features. The rate was advised based on experience by the head of the TU Delft Laboratory Wim Verwaal.

2.3.3 Tensile Strength

Tensile testing predicts how the specimen will behave under loading. Tensile strength is a measurement of the required force to "pull" a specimen until the breaking point. Tensile strength is the maximum amount of tensile stress a specimen can endure before failure. A hydraulic press with a maximum force of 50 MPa is used for testing. The results are visualised in terms of true stress calculated with Equation 11, (ASM International, 2004).

$$\sigma_t = \frac{\mathrm{F}}{A} \tag{11}$$

$$\sigma_t = true\ tensile\ stress\ [Pa]$$
$$\mathrm{F} = \mathrm{Force\ [N]}$$
$$\mathrm{A} = cross - sectional\ area\ [m^2]$$

2.3.4 Unconfined Compression Strength

The unconfined compression strength test determines the compressive rock strength. A hydraulic press with a maximum force of 500 MPa is used for testing. The shear strength is calculated to be 0.5 times the failure compressive stress. The compressive failure stress can be calculated as a series of calculation (Equation 12, 13 & 14), (ASTM International, 2014):

$$\varepsilon_1 = \frac{\Delta \mathrm{L}}{\mathrm{L_o}} \tag{12}$$

$$\varepsilon_1 = axial\ strain$$
$$\Delta\mathrm{L} = \mathrm{change\ of\ specimen\ length}$$
$$\mathrm{L_o} = initial\ specimen\ length$$

$$A = A_o/(1 - \varepsilon_1) \tag{13}$$

$$\mathrm{A} = \mathrm{cross - sectional\ area\ (average)}$$
$$\mathrm{A_o} = \mathrm{initional\ cross - sectional\ area\ (average)}$$

$$\sigma_c = \frac{P}{A} \tag{14}$$

σ_c = true compressive strength
P = applied load [kPa]

A well-known elastic constant is Young's modulus, describing the material's stiffness. This modulus is determined from the linear-elastic regime of the recorded stress and strain obtained by UCS testing. Non-linearity at low stress and strain is caused by the closure of already existing micro-cracks, whereas at high-stress conditions the non-linearity is caused by the initiation of new fractures. These regimes are visible in Figure 13.

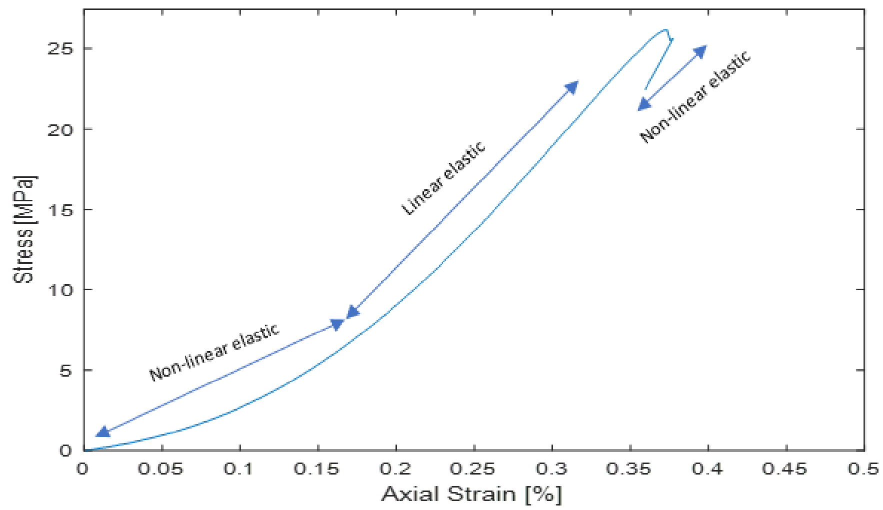

Figure 13: Axial Strain vs. Stress of Mono-lithologic Sample BEN-001

Material stiffness is determined by the average relation between strain and applied stress, which is given by Hooke's Law (Equation 15), (Roylance, 2008).

$$E = \frac{\sigma_a}{\tau_a} \tag{15}$$

$E = Young's\ Modulus\ [dimensionless]$
$\sigma_a = axial\ stress\ [MPa]$
$\tau_a = axial\ strain\ [dimensionless]$

The Young's Modulus has been determined in Matlab by data selection within the linear elastic regime of stress-strain curves (I) and calculating the gradient at every step size. Those gradients (II) are plotted into a histogram, visualised in Figure 14. The modulus has been determined as the largest bin in value.

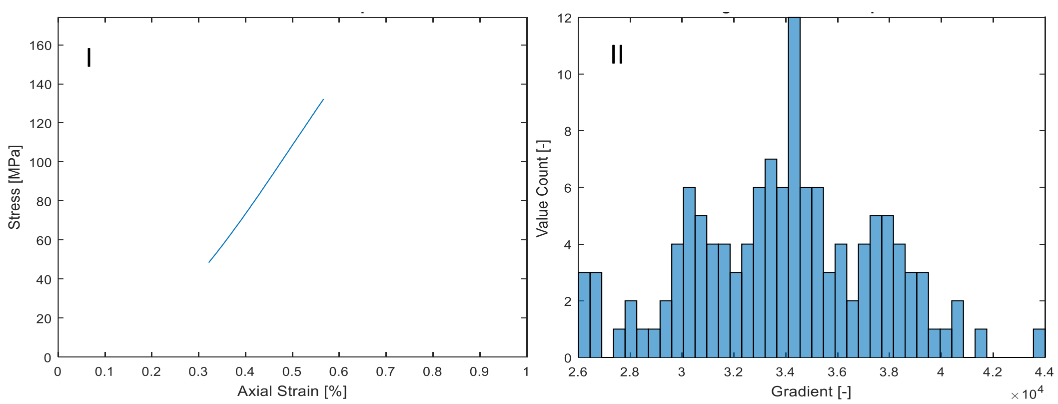

Figure 14: (I) Linear Elastic Regime of Mono-lithologic Sample AIN-004 and (II) the Plotted Gradient Histogram of Mono-lithologic Sample AIN-004

2.3.1 Confined Compressive Strength Test

Figure 9 shows the configured and mono-lithologic samples which are carried-out in the Confined Compressive Strength test setup. Testing has been done to investigate the influence of mechanical contrast on fracture behaviour by hydraulic fracturing. These fractures may or may not propagate through the interface of the configured samples and will be visualised with a micro-CT scanner[6].

Figure 15 (I) visualizes a Confined Compressive Test using a Triaxial Hoek cell, where a chamber pressure of 10 Mega Pascal (MPa) is set as default and delivered by a Teledyne ISCO pump. A hydraulic ram pressurises the mono-lithologic sample until breaking point. LVDT sensors measure vertical movement. Figure 15 (II) visualises a Fracking experiment using a Triaxial Hoek cell, constant chamber pressure of 10 MPa and two Teledyne ISCO pumps. A second pump with valve was used for quick water injection of 100 millilitres per minute for the fracking of the configured samples.

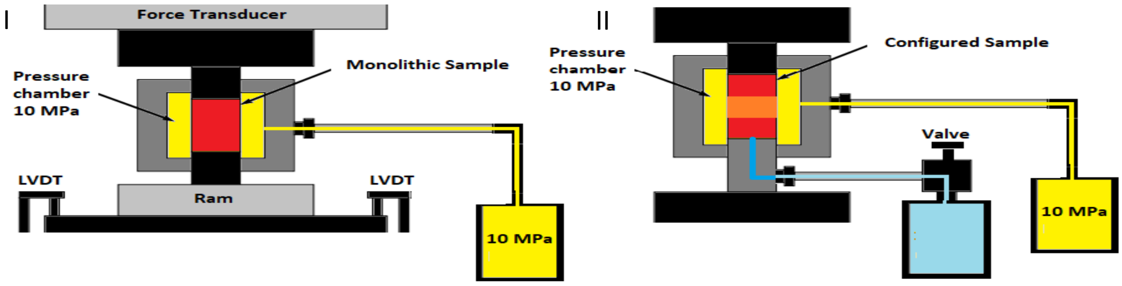

Figure 15: Confined Compressive Test (I) and Fracking at Confined Pressure (II)

2.3.1 Micro Computed Tomography (Micro-CT) Scanner

The Nanotom X-ray Micro-CT scanner of the Technical University of Delft was used in order to visualize obtained fractures at a resolution of 30 micrometres. X-rays are used to create cross-sectional 2D images. A 3D dataset is automatically obtained by stacking 2D cross-sectional images. Fracture propagation analysis is fulfilled by the use of myVGL 3.0 SP4 software by Volume Graphics, (Volume Graphics, 2019).

2.3.2 Chemical XRF and XRD Analysis

The XRF as the XRD analysis is conducted by the laboratory of Sibelco Belgium in Dessel. The tests are conducted as stated by the ASTM test specification. The chemical analysis is only fulfilled on the samples of the Lieblich III quarry to investigate the effect of oven drying on the Atterberg Limit and the difference in sand content.

Chemical Analysis using wavelength Dispersive X-Ray Fluorescence (XRF) spectrometry is able to show the following ten major elements SiO_2, Fe_2O_3, MgO, Al_2O_3, CaO, Na_2O, K_2O, TiO_2, P_2O_5, MnO and LOI. Firstly, the specimen is ignited. Secondly, the specimen is fused with Lithium-Tetraborate resulting in a glass disc. This disc is introduced into the XRF and irradiated with X-Rays. The emitted X-ray photons are counted, where the concentration determines the 10 major elements and the gravimetric loss due to ignition (ASTM International, 2009).

Chemical Analysis using X-Ray Diffraction (XRD) will determine only the following main minerals: Quartz, Kaolinite, Palygorskite, Smectite and Goethite. The X-rays are diffracted by the atoms' electrons into many specific directions, angle and intensity measurements determine the different main minerals and their quantity.

[6] A Nanotom X-ray micro computed tomography scan, for the computation of a three-dimensional dataset by stacking two-dimensional image datasets.

2.4 Slope Stability Simulation

After the observation of slope cracks within the Hohewieße quarry, a slope stability simulation on this particular quarry has been fulfilled by a secondary company named Arthe. Concluding a stable slope environment. The simulation will be done in order to investigate the influence of inter-bedding on slope stability. The obtained Mohr-Coulomb parameters have been used as soil input parameters for simulation purposes. Simulation software Stabilité has been obtained through the University of Liege.

2.4.1 Influence Water Content on Clay Strength Parameters

When over-consolidated clay have been excavated, negative pore pressures might exist, due to stress changes during earthworks. These two factors increase the likelihood of swelling over long term stability. If the moisture content increases by water seepage or an intensively period of rain, the likelihood of failure increases. If the structures or buildings exceed the undrained shear stress, deformation will occur, (Nowak & Gilbert, 2015). An increase in slope failures is reported to be increased during or after heavy rainfall. High rainfall or flooding causes unsaturated parts of the clayey soil to lose their apparent cohesion. During rainfall infiltration, pore-water pressure increases due to the suction forces of absorbing clay and an increase in the water table. The highest influence of pore-water pressure could be observed in the tau of the slope, where compressional strains could be observed in vertical as horizontal direction (Kaixi, et al., 2016).

An increase in the fresh clay's water content is accompanied by a decrease in shear strength. The degree of decrease in shear strength depends primarily on the respective plasticity characteristics of the clay. In other words, the clay's shear strength is inversely proportional to the water content ratio, (Kurakose, et al., 2017). The effect of the dry period is a lowering of pore-water pressure and shrinkage of the clay, (Yuen, et al., 1998).

As shown in Figure 16 where water content [%] is plotted against cohesion [kPa], an increase in water content is accompanied by an increase or decrease in cohesion. The soil cohesion can attribute to the compaction of the soil particles, electromagnetic & electrostatic forces and capillary potential. If the water content as seen in Figure 16 exceeds the cohesion's limit, the separation between particles increases causing the electromagnetic & electrostatic forces and capillary potential to decrease and the cohesion will decrease as well, (Dong, et al., 2011). Note that Figure 16 is for illustration purposes, meaning that the relation and critical limit between cohesion and water content will be different per type of soil.

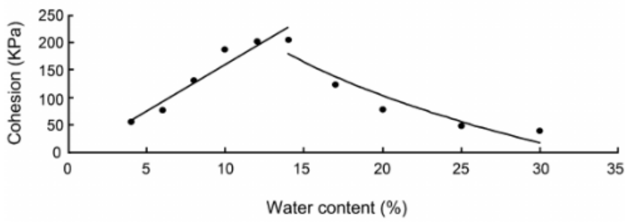

Figure 16: Increase and decrease of Cohesion with changing Water Content for Illustration purposes, (Dong, et al., 2011).

2.4.2 Mohr-Coulomb as Input Parameter

According to the Mohr-Coulomb formula (Equation 16), it can be stated that the drained shear strength will decrease linearly if the pore pressure increases. It all depends on the effective normal stress acting on the surface of failure (Abramson, et al., 2002).

$$\tau_f = c' + (\sigma_n - u) * \tan(\varphi') \quad [7] \qquad (16)$$

[7] (Abramson, et al., 2002)

$$\tau_f = drained\ shear\ strength$$
$$c' = effective\ cohesion$$
$$\sigma_n = normal\ stress$$
$$u = pore\ water\ pressure$$
$$\varphi' = internal\ friction\ angle$$

The theory is based on the assumption that failure depends only on σ_1 and σ_3. The shape of the failure envelope can be linear or non-linear, which is exhibited by many different rock types; Mohr's criterion allows a curved failure envelope, (Labuz & Zang, 2012). Figure 17 shows the theoretical Mohr-diagram and failure envelopes.

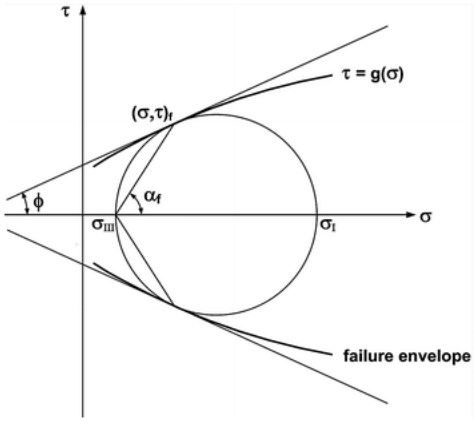

Figure 17: Mohr-Diagram and Failure Envelopes, τ = Shear Strength, σ = Normal Stress, ϕ = Angle of Internal Friction, (Labuz & Zang, 2012).

2.4.3 The factor of Safety as Output Parameter

The influence of effective normal stress on the slip surface can be denoted by the Factor of Safety (FOS), analysed by Frohlich (1953). This factor is normally expressed as a ratio and definable as the maximum shear strength divided by the mobilized shear strength at failure. The Factor of Safety could be denoted in an upper and lower boundary. Tests indicated that the lower boundary gives accurate Factor of Safety values, which correspond to a homogeneous circular failure. A constant Factor of Safety along the slip surface can be formulated in two major slip surfaces; with respect to a moment (Equation 17) or force (Equation 18) equilibrium (Abramson, et al., 2002). Equilibrium based on momentum can be used in order to simulate rotational landslides.

$$F_m = \frac{M_r}{M_d} \tag{17}$$

$$F_m = Factor\ of\ Safety\ (Momentum)$$
$$M_r = Resisting\ Moment\ (Sum)$$
$$M_d = Driving\ Moment\ (sum)$$

The centre of circular failure will be taken as the point of moment. However, if failure is not a circular movement, an arbitrary point can be taken for analysis or simulation. A changing arbitrary point can result in different results if horizontal force equilibrium is not satisfied at for instance within the Bishop's Method (Equation 17). Equilibrium based on force can be used in order to simulate or analyse rotational or translational failure (Abramson, et al., 2002).

$$F_m = \frac{F_r}{F_d} \tag{18}$$

$$F_m = Factor\ of\ Safety\ (Force)$$
$$F_r = Resisting\ Force\ (Sum)$$
$$F_d = Driving\ Force\ (sum)$$

Observations of the slope failure in the Sibelco Lieblich III quarry suggests a translational failure, which makes the Factor of Safety based on force equilibrium the most logical. A slope can be considerately safe if the determined safety factor > 1. However, factors around one are doubtfully safe. By taking heavy rainfall, consequences of failure and geological material characteristics into consideration, a recommended factor of safety can be established. The risk of human and economic losses is average within the Westerwald quarries, a recommended FOS of 1.3 is advisable as can be determined from (Abramson, et al., 2002)

Table 2: Risk of Human losses against Risk of Economic losses in Terms of Factor of Safety, (Abramson, et al., 2002)

Risk of Economic Losses	**Risk of Human Losses**		
	Negligible	**Average**	**High**
Negligible	1.1	1.2	1.4
Average	1.2	1.3	1.4
High	1.4	1.4	1.5

3 Results

The soil mechanical parameters are characterised by an Unconfined Compression Strength (UCS), Acoustic test and Atterberg Limits test on the oven-dried specimen at the Technical University of Delft. The usage of dried specimen for Atterberg Limits is not according to the ASTM guidelines, the effect of oven drying on mineralogy[8] have been determined in subsection 2.3.2: Chemical XRF and XRD Analysis. Characteristics of the mechanical properties can be obtained with two out of the four elastic constants (Brocks & Steglich, 2006). The static[9] Young's Modulus obtainable from the UCS and dynamic Poisson's Ratio has been chosen for mechanical property characterisation.

3.1 Material Characteristics

Subdivision in the material characteristics is made between the field (Table 3) and oven-dried conditions (Table 4). A complete sampling description will be given on Sample Specification on page 83.

Table 3: Field Conditions of obtained Material with Relevance to the Report

Material	Code [-]	Moisture [ratio]	Field Density [kg/m^3]	Description [Type, Colour, Friability, Other]
Clay	[GE-DE-LI-014]	0.29	$1.49 * 10^3$	Clay, dark red, weathered, extremely wet & coarse stiff clay red clay peddles
Clay	[GE-DE-LI-008]	0.18	-	Clay, Grey/brown, very sticky/plastic, plastic clay
Clay	[GE-DE-LI-007]	0.15	$1.80 * 10^3$	Clay, Grey/brown, sticky/stiff, plastic clay
Wet Alternation	[GE-DE-LI-006]	0.16	$1.71 * 10^3$	Sandy clay, brown/yellow, non-sticky, not plastic
Top Soil	[GE-DE-MA-001]	0.27	$1.68 * 10^3$	Sandy clay, brown/black, non-sticky, small peddles within the soil
Clay	[GE-DE-MA-002]	0.19	$2.04 * 10^3$	Clay, brown/beige, very sticky, plastic
Clay	[GE-DE-MA-004]	0.12	$2.20 * 10^3$	Clay, yellow/orange, stiff, brittle, feels very waxy
Clay	[GE-DE-MA-009]	0.04	$2.12 * 10^3$	Clay, white, stiff, brittle, breaks/powders easily during sampling
Clay	[GE-DE-MA-008]	0.12	$2.20 * 10^3$	Same sampling layer as [GE-DE-MA-004] but different location

The samples are dried at 105° Celsius for at least 24 hours to ensure all pore water is dissipated. Rock or soil shear strength originates from friction between particles. Greater normal stress results in greater shear stress between the grain particles. Pore pressure reduces the stress between the grains by pushing them apart. As a result, the shear stress will be reduced (Frederick University, 2017) (Skels & Bondars, 2015). Strength classification of the formation needs to be deducted from the dry uniaxial compressive strength (UCS), while the saturated strength and sensitivity to the water of the formation are needed for engineering designs (Vásárhelyi & Ván, 2006). These designs are based on shearbox

[8] Smectite is the first clay mineral to disperse under heating, therefore the effect of heating on the Atterberg limit is visible by looking at the XRD diffraction pattern of Smectite after heating.

[9] The elastic properties could be measured within the laboratory by triaxial stress tests (static measurements) and by acoustic travel time and bulk density, (Crain, 2015).

test data. Table 4 shows sample LI006 & LI007, which are closely related to each other in terms of field observation. As a result, their additional parameters were determined.

Table 4: Material Characteristics after being dried at 105° Celsius, Compression Wave Velocity & Shear Wave Velocity & Poisson's Ratio are based on Acoustic Measurements, Unconfined Compressive Strength & Young's Modules are based on Unconfined Compressive Strength.

Material	Compression wave velocity [m/s]	Shear wave velocity [m/s]	Unconfined Compressive Strength [Mpa]	Young's Modulus [GPa]	Poisson's Ratio [-]
Clay [GE-DE-LI-007]	$1.51 * 10^3$	$9.40 * 10^2$	0.51	0.31	1.32
Wet Alternation [GE-DE-LI-006]	$1.34 * 10^3$	$9.47 * 10^2$	0.49	0.17	1.57

3.1.1 Grain-size Distribution

Mass-Median-Diameter (MMD), an average particle diameter by mass is considered to be equal to a 50% passing rate. Figure 18 visualises the grain size versus the passing percentage of samples LI006 and LI007 from the Lieblich III Quarry. The volumetric amount of sample LI006 was lacking for measuring the grain sizes smaller than 80 micrometres. Recordings of the grain-size distribution till a passing rate of approximately 35 to 45% in mass are visible. It can be concluded from the Figure that sample LI006 has a better sorting than sample LI007 since at least 50% mass of specimen LI006 is passed between grain-sizes of 0.055 until 0.3 millimetres. For specimen LI007, 50% of the mass is between 0,005 until 0.6 millimetres in diameter. These findings are verified by the relatively fast consolidation of LI006 in comparison to LI007 and field observations. The wet alternated layer (specimen LI006) has a MMD value of 0.055 mm, whereas the more clayey specimen has a lower MMD value of 0.01 mm. Soils can be considered sand if the MMD grain-size is between 0.06 and 2 mm. Sample LI007 has a 34% sand content, whereas for sample LI006 a 48% sand content. Equal to a difference of 14%. This difference in sand content verifies that the failure plane indeed consisted out of a sandier specimen. The methodology can be found in 2.3.5 Grain size distribution by sieves and Hydrometer on page 26.

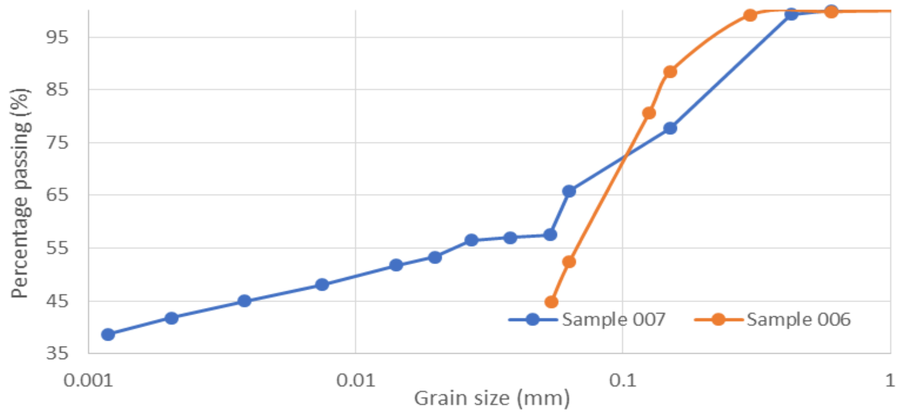

Figure 18: Grain-size Distribution of Specimen LI006 and LI 007

3.1.2 Mineralogy

Verification of the difference in the grain-size distribution of specimen LI006 and LI007 can be done by XRF and XRD analysis. Figure 19 visualises the chemical XRF compounds of samples LI006 until LI008 in logarithmic scale. Tests are done on oven-dried samples, in order to investigate the effect of heating to 105 degrees Celsius for at least 24 hours on the Atterberg Limits. Figure 20 visualises the Smectite content, which is around 7% for specimen LI007 and LI008. Smectite is the first clay mineral to disperse under heating. Effect of dispersion will be visible by a shifted diffraction pattern of the Smectite. No forms of dispersion have been found and the effect of heating can be neglected, meaning that the Atterberg Limit can be fulfilled on oven-dried material or fresh material.

Important compounds are SiO_2 relating to the quartz (sand) content and Al_2O_3 relating to the clay Kaolinite clay content. The XRD and XRF tests are checked by comparing the percentages of SiO_2 to quarts and Al_2O_3 to Kaolinite in Figure 19 and Figure 20 respectively. It can be assumed that the quartz is linkable to the sand content since both specimens have the same deposition origin. Figure 19 shows a 86% SiO_2 content for LI006, whereas for sample LI007 a 69% SiO_2 content. Equal to a difference of 17%, relative close as to the difference of 14% found by sieving.

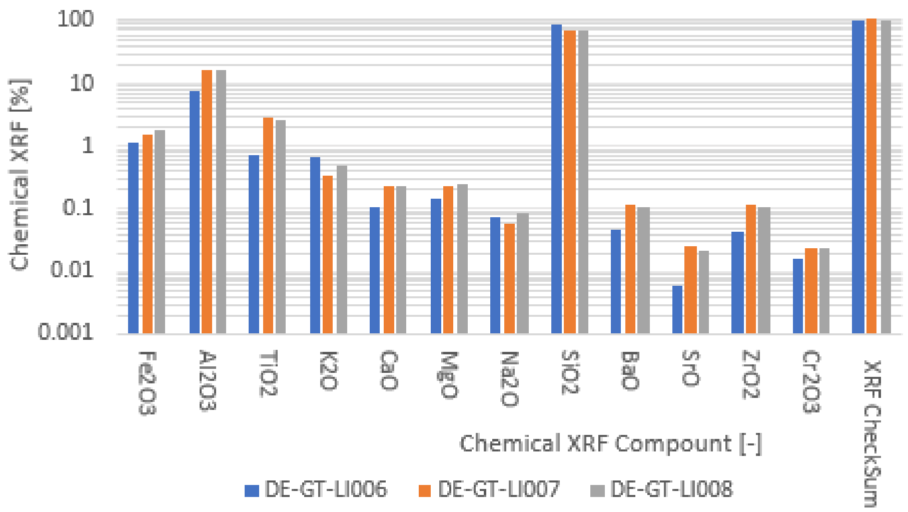

Figure 19: Chemical XRF on Lieblich III Specimen

Table 5: Chemical XRF Analyse Data, (Hollanders, 2019).

Chemical XRF Compound	DE-GT-LI006 [%]	DE-GT-LI007 [%]	DE-GT-LI008 [%]
Fe2O3	1.18	1.61	1.78
Al2O3	7.69	17.09	15.93
TiO2	0.75	2.83	2.58
K2O	0.66	0.34	0.48
CaO	0.11	0.23	0.23
MgO	0.15	0.24	0.25
Na2O	0.07	0.06	0.09
SiO2	85.69	69.27	70.08
BaO	0.05	0.12	0.11
SrO	0.01	0.03	0.02
ZrO2	0.04	0.11	0.11
Cr2O3	0.02	0.02	0.02
XRF CheckSum	102.37	106.57	105.20
Loss at ignition	2.99	7.34	6.81

Figure 20 (I) visualises the XRD compounds of samples LI006 until LI008. It can be observed that the quartz content of LI007 and LI008 are very close to each other, which is logical since both samples have the same soil origin but are sampled in a different season. Figure 20 clearly shows that the wet alternation layer (LI006) has a significant different Quartz content, a difference of 29% to LI007. All three methods are verifying a sandy failure plane. Figure 20 (II) visualises the diffraction pattern of specimen LI006, in order to show how the data of Figure 20 (I) is established. Compounds percentage of specimen LI007 and LI008 are acquired by similar diffraction patterns.

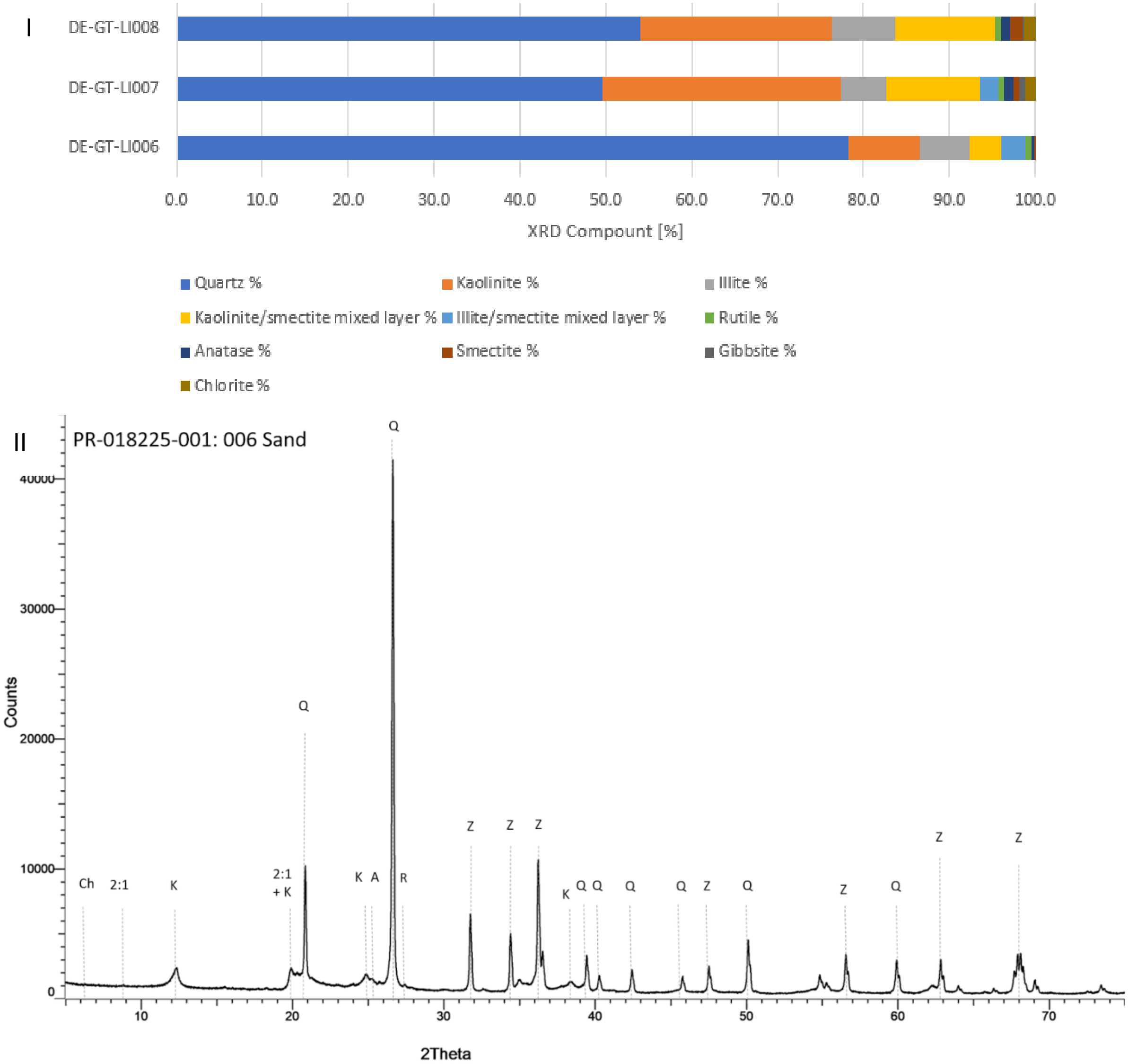

Figure 20: (I) Chemical XRD on Lieblich III Specimen, (II) Diffraction Pattern of LI-006. The Main Minerals that contribute to the most Important Reflections are indicated, Z: Zincite, Q: Quartz, A: Anatase, R: Rutile, K: Kaolonite and 2:1 are Al-clays, (Hollanders, 2019).

3.1.3 Plasticity

Plasticity of the clay specimen determines the range of water contents while the clay exhibits plastic behaviour. Figure 21 shows the plasticity index versus the liquid limit of the relevant clay specimens, the different characteristic regions for correlation are depicted by black lines, where clays of different regions could not be correlated with each other. Although the clays of Lieblich III and Hohewieße have been sampled at different moisture contents, similar plastic characteristics could be found. This report uses clay plasticity for characterisation purposes only.

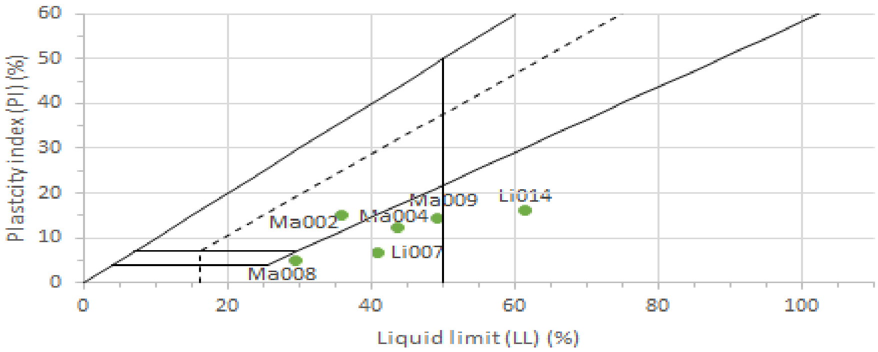

Figure 21: Plasticity Index of the Different Clay Samples. MA001 was observed to be too Non-Plastic while testing, whereas LI006 and LI008 was assumed to be Equal to LI007

3.2 Rock Mechanical Parameters

Rock mechanical parameters are established on dried (50 ^oC) specimens of approximately 6 and 3 centimetres in length and diameter respectively. Samples have been kept for at least 24 hours on the dried condition to ensure that all pore fluids were dissipated. Samples were prepared for the usage of Unconfined and Confined Compressive Tests.

3.2.1 Material Characteristics

The density values of Table 6 are obtained by arithmetic averaging[10] of dimensional and weight data. The table shows the material characteristics of the different materials used in terms of density and appearance.

Table 6: Material Characteristics of Sandstones based on Averaging.

Material	Code [-]	Density [kg/m^3]	Description [Type, Colour, friability, other]
Low porosity Fontaine Bleau	LFB	$2.40 * 10^3$	Sandstone, beige with red stains, slightly friable, low porosity
High porosity Fontaine Bleau	HFB	$2.50 * 10^3$	Sandstone, beige with red stains, moderate friable, high porosity
Ainsa Sandstone	AIN	$2.46 * 10^3$	Sandstone, grey, non-friable, small white veins, very low porosity, turbidite
Bentheimer	BEN	$2.01 * 10^3$	Sandstone, yellow-white, friable, high porosity

Table 7 shows the calculated rock characteristics, the data is obtained using UCS, Pycnometer and Acoustic methodologies. The compression wave velocity, shear wave velocity, UCS Strength, Young's Modulus and Poisson's Ratio have been averaged according to the Arithmetic mean methodology (University of Neuchâtel, 2008). The table shows that the Ainsa Sandstone will behave

[10] Arithmetic mean can be defined as an "average" which is calculated as the sum of the numbers divided by the total amount of numbers. Characterization of the centre frequency distribution can be calculated while affording each measurement or observation the same weight (University of Neuchâtel, 2008).

the strongest in tensile stress conditions, followed by the low porosity Fontaine Bleau, high porosity Fontaine Bleau and lastly by the Bentheimer sandstone. The porosity measurements are taken as an average of 22 specimens per material type. The porosity values between the materials are corresponding to the compression wave velocity of the materials respectively. Speed of sound is faster through rock than air, therefore a higher porosity will generally lead to a lower compression wave velocity. Remarkable is that the low porosity Fontaine Bleau behaves stronger in compressive stresses than the Ainsa Sandstone but more brittle during tensile stresses. Reason for this is that the Ainsa Sandstone is a turbidite formation, where the clay fabric of the fine-grained sequences increases the resistance to tensile stresses.

Table 7: Rock Mechanical Parameters of the Different Sandstones based on Averaging. UCS; Unconfined Compressive Strength, Av; Average. The values of Compression Wave Velocity and Shear Wave Velocity of the High Porosity Fontaine Bleau were tested Suspicious Low and therefore left out.

Material	Porosity [-]	Compression wave velocity [m/s]	Shear wave velocity [m/s]	UCS [MPa]	CCS at 10 MPa [MPa]	Young's Modulus [GPa]	Poisson's ratio [-]	Tensile Strength [MPa]
Low Porosity Fontaine Bleau	0.04 - 0.06 Av: 0.05	$4.45*10^3$	$3.06*10^3$	116-162 Av: 133	459	41.1 - 43.3 Av: 42.2	1.40	7.2
High Porosity Fontaine Bleau	0.09 - 0.11 Av: 0.10	-	-	48-73 Av: 61	233	13.5 - 21.3 Av: 17.8	1.21	3.2
Ainsa Sandstone	0.01 - 0.03 0.02 Av: 0.02	$4.95*10^3$	$3.16*10^3$	119-197 Av: 163	283	27.7 - 38.2 Av: 35.4	1.32	11.8
Bentheimer	0.20 - 0.26 Av: 0.25	$2.65*10^3$	$1.77*10^3$	18 - 26 Av: 21	120	6.3 – 9.1 Av: 7.7	1.40	3.2

3.3 Failure Envelopes & Shear Strength Parameters determined by Shearbox Data

Table 8 visualises the obtained shear strength parameters; cohesion and friction angle. The variation of data points towards the trendline is given as a ratio between zero and one, where one stands for a very low variation and zero for a large variation. A variation ratio of 0.91 is found within the test data of specimen MA004. This variation is the result of horizontal cracks within the specimen as visible in Figure 22. The surface of the crack feels sandy and non-waxy, whereas the surrounding material feels waxy[11]. In conclusion, the cracks are not induced by sampling equipment but from geological or mining origin.

Figure 22: Cracked Clay Plug MA-004 before Shearbox Testing

[11] A waxy feeling originates from a high aluminium percentage within the clay, (Sibelco Deutschland GmbH, 2013)

Table 8: Specimen Shear Strength Parameters determined by Shearbox Data, ϕ = Angle of Internal Friction R^2= Variation of Data Points towards Linear plotted line

Specimen	Cohesion	ϕ [°]	R^2 [Ratio]	Remarks
LI-006	0	36.5	0.88	Sheared after consolidation took place
LI-007	26.7	38.1	0.94	Sheared by dry and wet outside conditions
LI-008	46.5	18.9	0.96	-
HO-014	51.0	27.8	0.98	Densified to $1.440 * 10^3$ $\mathrm{kg/m^3}$ before shearing
HO-014	58.1	30.3	0.99	Densified to $1.660 * 10^3$ $\mathrm{kg/m^3}$ before shearing
MA-001	63.7	31.4	0.99	-
MA-002	70.6	21.3	0.99	-
MA-004	143	23.7	0.91	Horizontal cracks visible within specimen
MA-009	98.6	31.0	0.99	-

Figure 23 shows the failure envelope of fresh clay of the Sibelco Lieblich III quarry in the Westerwald region of Germany. The graph shows the normal stress versus the shear strength in kPa. The blue line shows the failure envelope of LI007, which resembles the sampling of fresh clay in the summer during a dry period of more than 8 weeks. The orange line resembles the failure envelope of fresh clay specimen LI008 sampled during the winter period, where the ground was frozen and covered by ice/snow. Sandy specimen LI006 is resembled by a green line. The dryer summer specimen LI007 with a moisture content of 15% is observed to have a decreased cohesion and an increased angle of friction value in comparison to the comparable wetter specimen LI008 with a moisture content of 18%. This observation is explained by electromagnetic & electrostatic forces increasing the capillary potential elated to an increase in water content. This increase of cohesion exists until the increase of water content will increase the soil particle distance, which decreases the electromagnetic & electrostatic forces and capillary potential. This phenomenon is illustrated in Figure 16.

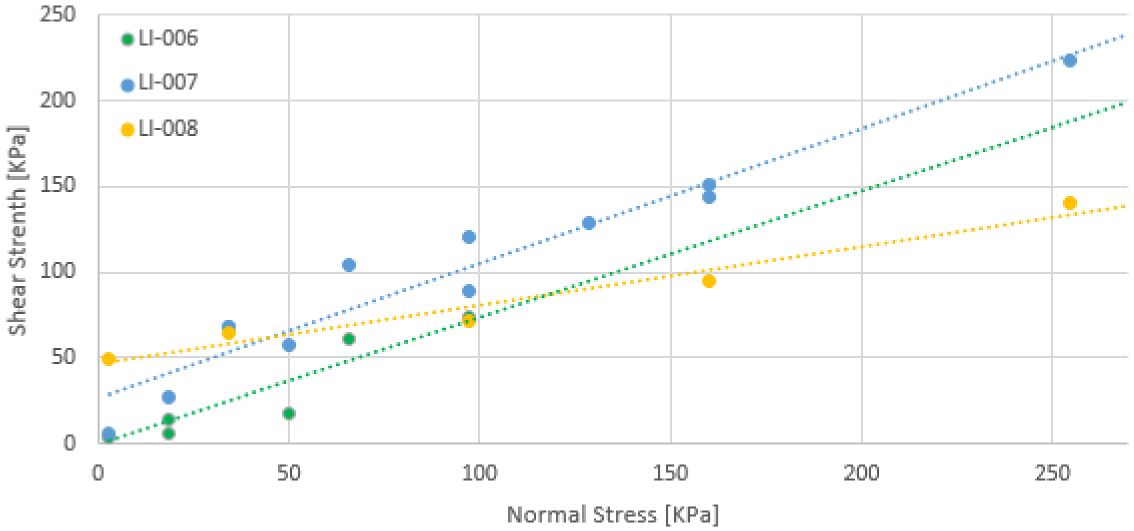

Figure 23: Failure Envelope of Sample LI-006 (Green), LI-007 (Blue) & LI-008 (Orange)

Figure 24 visualises the failure envelopes of the different clay lithologies within the Stemmer. The graph shows the normal stress versus shear strength in kPa. Remarkable is that the topsoil (specimen MA001) exhibits roughly the same failure envelope as over-consolidated clay specimen MA009. This may be due to compaction related by heavy equipment driving on the topsoil.

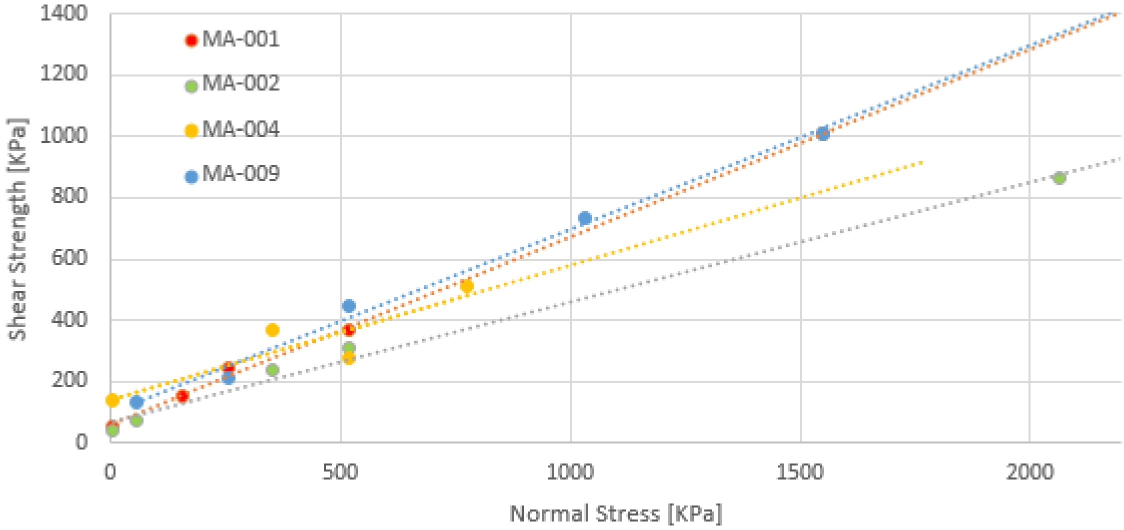

Figure 24: Failure Envelope of the Different Lithologies within the Stemmer Quarry

Figure 25 visualises the effect of the compaction of the red Hohewieße overburden in order to invest the soil suitability for compacted backfill. The graph shows the normal stress versus the shear strength in kPa. Two possible field densities have been sheared, with an average value of $1.440 * 10^3$ and $1.660 * 10^3 \ \mathrm{kg/m^3}$ respectively. The graphs visualise that the difference in field density does not change much in terms of shear resistance. A difference of approximately 6% in shear resistance is observed by a change of 13% in field density. The compaction strength of the least compacted red Hohewieße overburden is just 8% lower in strength than the over-consolidated sample MA-006. The overburden is in terms of strength related to the over-consolidated clays and suitable for backfill if compacted correctly.

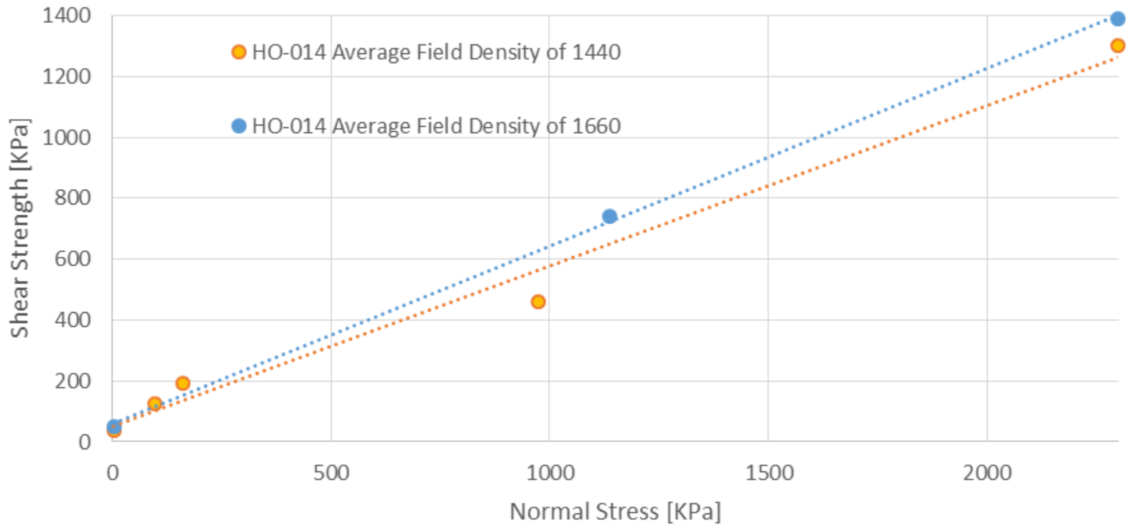

Figure 25: Failure Envelop of the Red Hohewieße Overburden at Different Average Field Densities

3.3.1 Slope Simulation based on Obtained Parameters and Observations

Earlier slope simulation has been done on the Hohewieße quarry, which concluded a stable environment. However, surface and slope cracks with very minor slope displacement were observed. These slope cracks are observed in the stiff clay. Field observation and test results showed a wet sandy slip-surface at the failed Lieblich III slope. A cracked open surface was observed in the Lieblich III quarry. Three simulation scenarios are established on these observations across cross-section A-A' of the Hohewieße quarry visualised in the figure below.

Figure 26: Cross-Section of the Slope Simulation of the Hohewieße Quarry. Red Line marks the Cross-Section and the Blue Arrow indicates the Mining Direction.

- Simulation 1, slope simulation with shear strength parameters (Table 9) obtained from earlier research, (Arthe, 2017). Figure 27(I) shows the slope simulation with multiple possible circular failure surfaces. Figure 27(II) visualises a schematic version of the simulated slope failure.

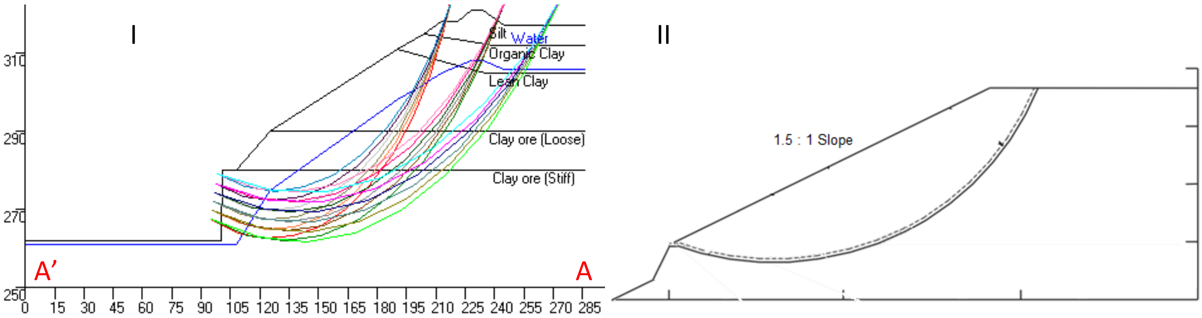

Figure 27: (I) Multiple Possible Circular Slope Failures (shown in Different Colouring), where Blue Line is the Hydrostatic Water Level. Figure (II) shows a Schematic Circular Slope Failure with a 1.5 : 1 (Horizontal : Vertical) Slope

Table 9: Geotechnical Units with Friction Angle and Cohesion, (Arthe, 2017)

Geotechnical Unit	Friction Angle [°]	Cohesion [kPa]f
Silt	21	200
Organic Clay	15	0
Lean Clay	22.5	5
Clay ore (loose)	17.5	25
Clay ore (stiff)	27	2

Earlier slope stability simulation done by the company Arthe resulted in a factor of safety of 1.37, which is acceptable in terms of stability as discussed in 2.4.3: The factor of Safety as Output Parameter. A factor of safety between 1.32 and 1.45 has been obtained by using Bishops' method and the geotechnical parameters of Table 9.

- Simulation 2 uses the same strength parameters as in simulation 1. Pressured sand clusters are able to change the hydraulic head within the clay slope. This simulation assumes that the fracture propagation is induced by a pressure difference at the interface of the sand inter-bedding and less permeable clay formation. The water level in the inclinometer that can possible perforates the sand layer is found at 305 metres true vertical. Therefore, the hydraulic head is updated to 305 metres unless a higher hydraulic head can be assumed. The hydraulic head decreases in value when the sand inter-bedding is thinned-out. The maximum required horizontal distance between the sand inter-bedding and clay slope surface is 9.0 metres, this value is calculated in subparagraph 4.4: Minimum Thickness of Clay Formation for Fracture Initiation. The shear plane is forced to start at the observed surface cracks and slide along the pressured sand bar. Figure 28(II) visualises a schematic non-circular slope failure as should be established within the field.

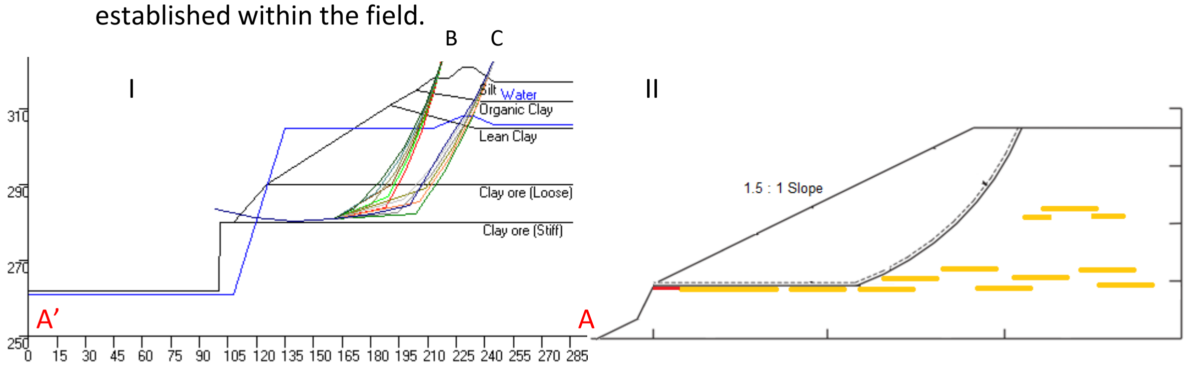

Figure 28: (I) visualises simulated Slope, where a Horizontal Fracture is initiated, the Failure Surfaces are indicated as A and B and the Blue Line represents the Hydraulic Head. (II) Schematic Non-Circular Face Slope Failure used for Slope Stability Analysis of an 1.5 : 1 (Horizontal : Vertical) Slope, where the Yellow Bar is a pressured Sand Cluster and the Red Bar is a Natural Hydraulic Fracture caused by a pressured Sand Inter-Bedding.

A factor of safety of around 0.9 and 1.1 is found for the non-circular failure plane starting in the surface fractures B and C respectively. These surface fractures are visualised in Figure 28(I). An average factor of safety of 1.0 for simulation 2 has been calculated. The slope can be considerately unstable if the possible economic and human losses are taken into consideration.

- Simulation 3 uses the same strength parameters of simulation 1 and the same hydraulic head as simulation 2. The shear plane is forced to start at the observed surface cracks and slide along the pressured sand bar. The simulation assumes that the high pressured fluid infiltrates into the clay formation. The infiltrated pore fluid weathers the clay formation and reduces the shear resistance against failure. The reduced shear resistance is simulated by back analysis. Back analysis calculates the factor of safety for different shear parameters of the clay formation surrounding the sand bar. Figure 29(II) visualised a schematic non-circular slope failure as should be established within the formation.

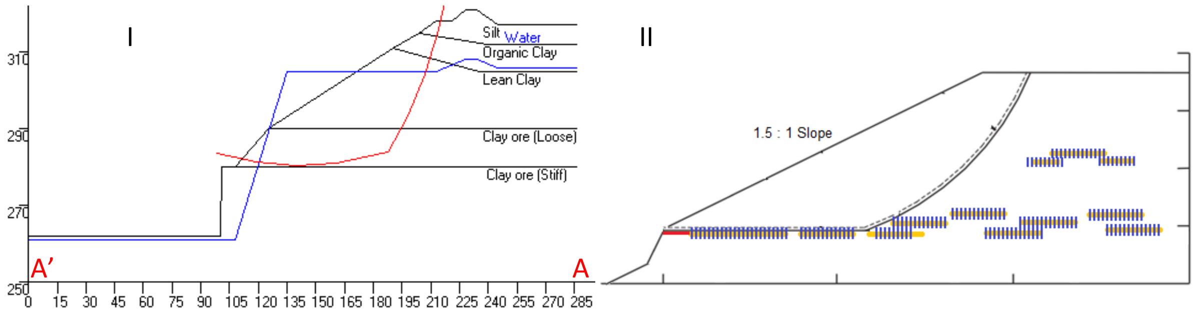

Figure 29: (I) visualises simulated Slope, where a Horizontal Fracture is initiated, the Failure Surface is indicated by the Redline and the Blue Line represents the Hydraulic Head. (II) Schematic Non-Circular Face Slope Failure used for Slope Stability Analysis of an 1.5 : 1 (Horizontal : Vertical) Slope, where the Yellow Bar is a pressured Sand Cluster, the Red Bar is a Natural Hydraulic Fracture caused by a pressured Sand Inter-Bedding and the Blue Bars are Weathered Clay Formations by Water Penetration.

Pressured pore fluid penetrates into the less permeable clay increasing the clay water content over time. The less permeable clay formation is denoted as the loose clay ore formation in Figure 29. More pore fluid will penetrate the less permeable clay if the confining stress decreases by mining activities. The clay’s friction angle will be lowered by an increase in water content. The clay’s cohesion value will decrease or increase by an increase in water content depending on the threshold value as explained in Figure 16. This threshold value is expected to be higher than a moisture content of 18%, which can be determined from the mineralogy and shearbox data of specimen LI007 and LI008. The mineralogy of these two samples shows that they are (almost) identical. An increase in moisture content from 15 to 18% of the Lieblich III clay results in an increase of cohesion and a decrease in friction angle as observed in Figure 23.

The factor of safety related to a decrease of clay shear strength and cohesion of the loose clay ore formation that surrounds the sand inter-bedding is determined by back analysis[12]. Table 10 visualises the different factor of safety values related to a decrease in friction angle and cohesion value.

Table 10: Cohesion and Friction Angle Back Analysis. Red is considered Unstable and Orange to be likely Unstable.

C(kPa)\phi(ø)	10	12.5	15	17.5
0	0.47	0.56	0.64	0.72
5	0.55	0.63	0.71	0.79
10	0.62	0.70	0.78	0.86
15	0.69	0.77	0.84	0.92
20	0.76	0.83	0.91	0.99
25	0.83	0.90	0.98	1.05

The failure surface propagates through the weakened clay due to a decreased resistance against failure by water infiltration. A decrease in friction angle and cohesion value has a high impact on the stability of the slope. A safety factor of 1.05 at normal conditions can already be considered non-stable if you take human and economic losses into consideration.

[12] Slope simulation program Stabilité offers the option back analysis to perform calculation on layer with decreasing friction angle and cohesion value.

3.4 Minimum Thickness of Clay Formation for Fracture Initiation

The minimum horizontal and vertical clay thickness for fracture initiation by hydrostatic pressure is based on data provided by the company Arthe and made visible within Figure 30. The sand aquifer has been made visible by cone penetration tests. The hydraulic head is found at 305.7 and 302.5 meters true vertical within the inclinometers. The shear surface is found at 285.2 meters true vertical. A maximum hydraulic head of 20.5 meters is able to pressure the sand inter-beddings. A hydraulic head of 20.5 meter equals to an isotropic pressure of 201 kPa.

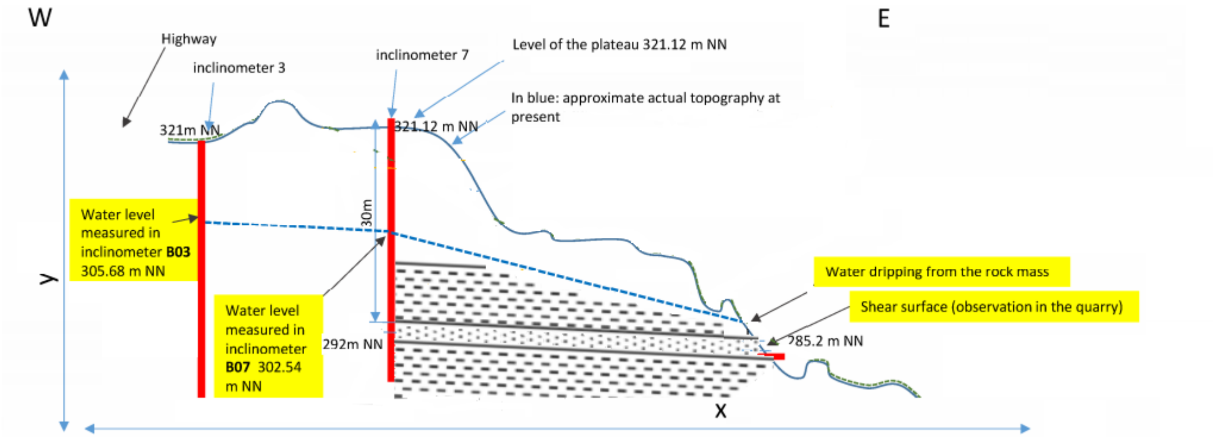

Figure 30: Geotechnical Data of the Hohewieße Quarry, (Arthe, 2017)

Figure 31 provided a close up of the Hohewieße slope lithology at the place of the fracture observation. The following assumptions are applicable within this schematic lithology and are based on structural geology (Bertoti, 2018), namely:

- The confining pressure resisting the initiation of the fracture is perpendicular to the fracture and has the shortest distance towards the outer surface.
- The fracture comes to the surface perpendicular to the slope surface.

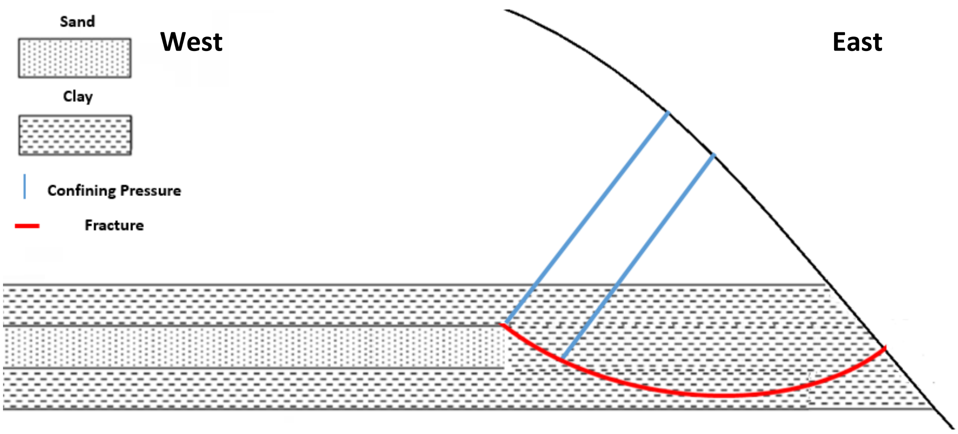

Figure 31: A Schematic Close Up of the Hohewieße Slope Lithology at the Place of Fracture Observation

The confining pressure resisting fracture initiation can be calculated by a series of equations, where Equation 19 is proposed by Karl von Terzaghi in 1925.

$$\sigma' = \sigma_{Confining} - u \qquad (19))$$

$\sigma' = effective\ confining\ stress$ [kPa]
$\sigma_{confining} = confining\ stress$ [kPa]
$u = pore\ pressure$ [kPa]

The confining stress exists out of a horizontal and vertical component. The cohesion of the soil has been taken as the horizontal component because the resistance against movement at a normal pressure of zero equals the cohesion value according to the Mohr diagram, (Labuz & Zang, 2012). The vertical component is calculated by using the shear resistance and slope ratio parameters. The horizontal axis of the slope ratio equals approximately the possible fracture length. The equations are based on a laboratory study of hydraulic fracturing in clay by R.A. Decker and S.P. Clemence, (1981).

$$\sigma_{Confining} = formation\ height * \sigma_{Normal} * TAN(\phi) + C \tag{20}$$

$$\sigma_{confining} = confining\ stress\ [KPa]$$
$$\phi = friction\ angle\ [°]$$
$$\sigma_{normal} = Normal\ Stress\ [KPa/m]$$
$$C = Cohesion\ [KPa]$$

Equation 19 has been solved with equation 20 & 21 for an effective stress that equals zero, resulting in equation 22. Effective stress of zero can be assumed due to the failure of the soil by fracture initiation.

$$\Phi_{pore} = H_{water} * 9.8 \tag{21}$$

$$\sigma_{pore} = pore\ pressure\ [KPa]$$
$$H_{water} = height\ of\ the\ water\ collumn\ [m]$$

$$formation\ height * \sigma_{Normal} * TAN(\phi) + C = H_{water} * 9.8 \tag{22}$$

Figure 32 has been established based on Equation 22 with the parameters from Figure 30. By solving Equation 22 for formation height, the fracture length can be calculated by using the slope ratio (vertical : horizontal), as shown in Equation 23. A slope ratio of 1:3 and an isotropic pressure of 201 kPa have been assumed based on inclinometer and volumetric data obtained by Arthe, (Arthe, 2017). The same geotechnical parameters of Table 9 have been used to determine the confining stress. A fracture can propagate through the interface if the horizontal distance between the sand inter-bedding and clay slope surface is within 9.0 meters.

$$Maximum\ Fracture\ Length = Formation\ Height * \frac{1}{Slope\ Ratio} \tag{23}$$

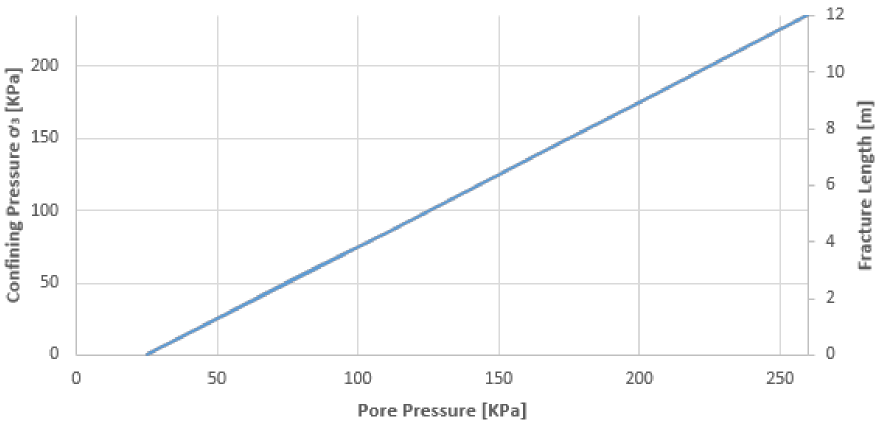

Figure 32: Fracture Length by increasing Pore and Confining Pressure for the Hohewieße Quarry

3.5 Hydraulic fracturing of Synthetic Layered Sample for Fracture Propagation

This sub-paragraph shows the propagation and continuity of the fractures in an artificial heterogeneous layered system depending on the mechanical properties of the layers. The fractures will be initiated by hydraulic fracturing in a dried layered system via water injection in a triaxial cell. Fracture propagation is analysed through Micro-CT scans. The mechanical properties such as acoustic wave velocities, unconfined & confined compressive strength and tensile strength of the tested layered systems are all determined.

3.5.1 Pressure Loss in Tubing while Using the CCS Injection Set-Up

Real-time pressure measurements are taken at the location of the pump. The pressure loss over a 2 metres tube of 2 mm inside diameter needs to be calculated to take it into account or to exclude it from the results. The following assumption hold for pressure drop calculations, (Byron Bird, et al., 2013):

- Steady-state laminar flow (Reynolds Number less than 2100)
- Newtonian fluid (water)
- Incompressible flow (constant density)
- Constant viscosity
- End effects are neglected
- No slip conditions at the wall
- The tube is in the horizontal direction

By assuming the above conditions the Hagen-Poiseuille equation (Equation 24) can be used, (Byron Bird, et al., 2013).

$$\mu = \frac{(\pi * (p_o - p_L) * R^4)}{8QL} \tag{24}$$

$$\mu = viscosity\ [Pa * s]$$
$$p_0 = pressure\ at\ Z = 0\ [Pa]$$
$$p_L = pressure\ at\ Z = L\ [Pa]$$
$$R = inner\ radius\ [m]$$
$$Q = flow\ [\mathrm{m^3/sec}]$$
$$L = tube\ length\ [m]$$

Which can be rewritten to

$$P = \frac{8 * \mu * L * Q}{\pi * R^4}$$

The viscosity of the injected water is equal to $8.90 * 10^{-4}\ Pa * s$. The pressure at the inlet is equal to 500 bar or $5 * 10^7\ Pa$. An inner radius of 0.002 m, length of 2 m and a constant maximum flow of 0.0000017 m/sec are measured within the set-up. By rewriting Equation 24, the pressure loss can be found.

$$\Delta p = \frac{8.90 * 10^{-4} * 8 * 0.0000017 * 2}{0.002^4 * \pi} = 482\ Pa$$

This means that at a maximum inlet pressure of $5 * 10^7$ Pa, an outlet pressure of approximately $4.99995 * 10^7$ can be observed. This is a loss of less than 0.001%, meaning the pressure loss can be neglected. Reynolds Number (Re) is calculated by Equation 25, to ensure the assumption of laminar flow still holds on these flow conditions, (Byron Bird, et al., 2013).

$$Re = \frac{4Q\rho}{\pi D\mu} \tag{25}$$

$$Re = Reynolds\ number\ [-]$$
$$Q = flow\ [\mathrm{m^3/sec}]$$
$$D = inner\ diameter\ [m]$$
$$\rho = density\ [kg/m^3]$$
$$\mu = viscosity\ [Pa * s]$$

By taking the viscosity of water and the same parameter input as by Equation 24, a Reynolds number of 0.6 is found. This value is less than 2100 and therefore the assumption of the laminar regime still holds.

3.5.2 Pressure Loss within propagated Fracture

To calculate the pressure loss over the initiated fracture until the formation's interface, the same assumption as for pressure loss through tubing are applicable. Figure 33 visualise the fracture within the fractured circular specimen with a diameter of 2 cm. Largest observed fracture aperture is approximately 0.4 mm, which is visualised by the micro-CT scanner. Note that smaller apertures will lead to a smaller pressure loss. The length of the first layer of the layered fractured system is approximately 2 cm.

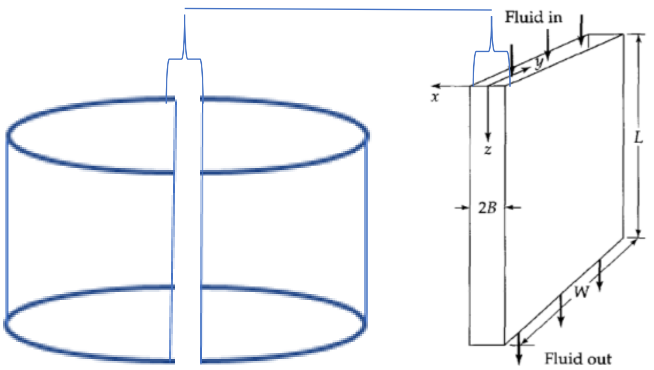

Figure 33: Laminar Flow in a Narrow Slit (Fracture)

Equation 26 is used to calculate the pressure drop over the fracture length, (Byron Bird, et al., 2013). A flow of 100 ml/min over a circular radius of 0.002m is recalculated over a squared slit area of 0.4 mm by 2 cm equalling to a total flow of 314 ml/min.

$$Q = \frac{2}{3}\frac{(p_o - p_L)B^3W}{\mu L} \tag{26}$$

$$Q = flow\ [\mathrm{m^3/sec}]$$
$$p_0 = pressure\ at\ Z = 0\ [Pa]$$
$$p_L = pressure\ at\ Z = L\ [Pa]$$
$$B = 0.5 * aparture\ [m]$$
$$W = width\ [m]$$
$$\mu = viscosity\ [Pa * s]$$
$$L = tube\ length\ [m]$$

Equation 21 can be rewritten to the pressure loss over the fracture:

$$(p_o - p_L) = \frac{3}{2} * \frac{Q\mu L}{B^3W} = 891\ Pa$$

A total pressure loss over the fracture of approximately 891 Pa is less than 0.002 % of the total pressure and is therefore neglected. A Reynolds number of nearly 4 has been determined by Equation 25. Assumption of laminar flow is correct since the calculated Reynolds number is less than 2100.

3.5.1 Confined Compressive Fracking on Mono-lithologic Specimen

The confined hydraulic fracture setup has been carried-out on the described mono-lithologic samples of Table 6 on page 39. Figure 34 visualises that the low porosity samples "LFB & S" have a quick pressure build-up due to a combination of a 100 millilitre per minute injection rate and a low permeability value. The Bentheimer Sandstone (B) has the highest permeability value, which is made visible by a relative slow pressure build-up due to sample saturation. After 7 seconds of running time, a pressure drop within specimen low Fontaine Bleau (LFB) originates from fracture initiation. After fracture initiation the fluid can dissipate through the created fracture, lowering the hydraulic fluid's pressure. The fluid will re-pressurize since it is a closed system. The other formations did not fracture since the local pressure difference did not surpass critical tensile stress values. The fluid dissipates too quickly through the sample due to high permeability (high porosity Fontaine Bleau and Bentheimer sandstone) or the fluid is not capable to act at critical levels within the sample due to very low permeable values (Ainsa sandstone).

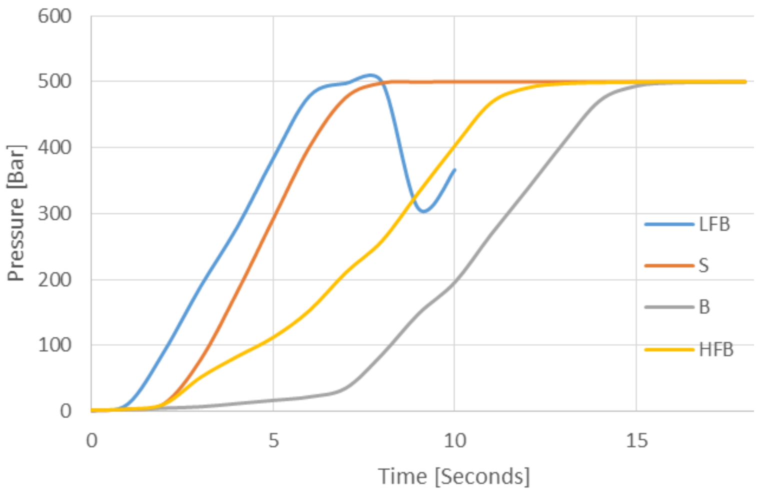

Figure 34: Pressure Build-Up by Fracking on Non-Adapted Mono-Lithologic Samples. LFB Sample Number Three of Low Porosity Fontaine Bleau Sandstone, HFB; Mono-lithologic Sample Number Two of High Porosity Fontaine Bleau Sandstone, S; Sample Number Two of Mono-lithologic Ainsa Sandstone, B; Mono-lithologic Sample Number Two of Bentheimer Sandstone.

Figure 35 shows the small perforation in the mono-lithologic Ainsa sandstone to create a local pressure difference in the volume of the sample instead of the specimen's surface.

Figure 35: The Specimen Left is the Mono-lithologic Fractured Low Porosity Fontaine Bleau and the Specimen Right is the Fractured Ainsa Sandstone by making use of a Small Perforation

Figure 36 (I) shows that the usage of a small perforation (as visible in Figure 35) makes it possible to fracture the low permeable Ainsa sandstone. Figure 36 (II) shows that with the addition of a perforation, critical tensile stress values are not yet surpassed within the two permeable formations.

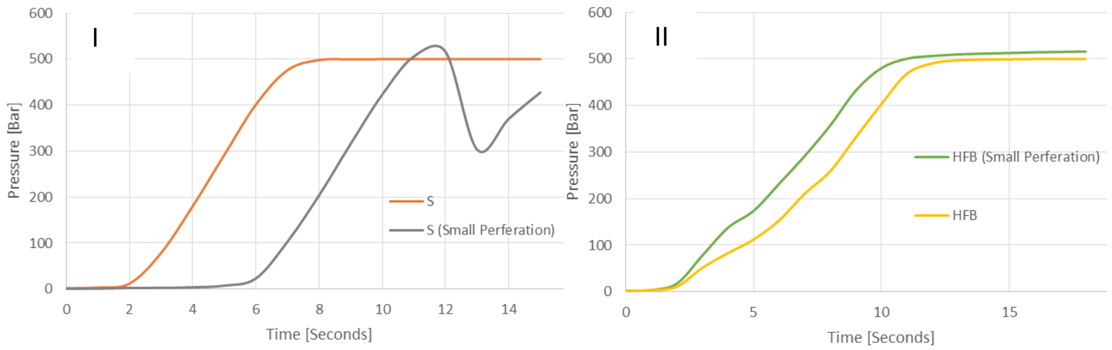

Figure 36: The use of a Small Perforation to Increase the Tensile Force on a Relative Low Permeability (figure I) and High Permeability (figure II) Specimen

A small layer of viscous oil on top of the permeable specimens was placed to decrease the rate of water dissipation into the specimen during pressure build-up. Figure 37 (I) visualises that the usage of a high viscose oil decreases the rate of dissipation and increases the local pore pressure difference. The critical tensile stress limit was surpassed in the high porosity Fontaine Bleau. Figure 37 (II) shows that the usage of a high viscose oil was not suitable to fracture the Bentheimer sandstone.

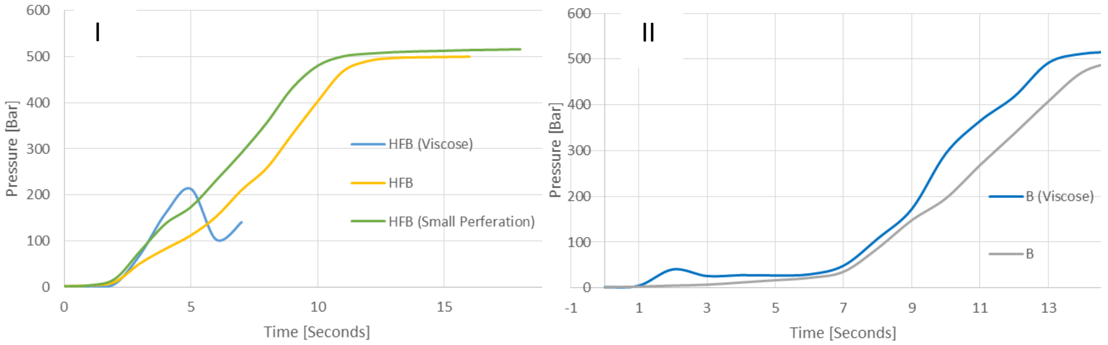

Figure 37: A Combination of a High Viscose Fluid to Lower Specimens Saturation Speed and Small Perforation to Increase the Tensile Force on a Relative Low permeability (figure I) and High Permeability (figure II) Specimen

Figure 38 visualises an injection fluid of 500 bar impacting the Bentheimer sandstone formation. The impact happened at around 50 seconds of experiment run time, after which an injection rate of 100 mL per minute dissipated into the specimen. The tensile stress limit of the Bentheimer sandstone was exceeded.

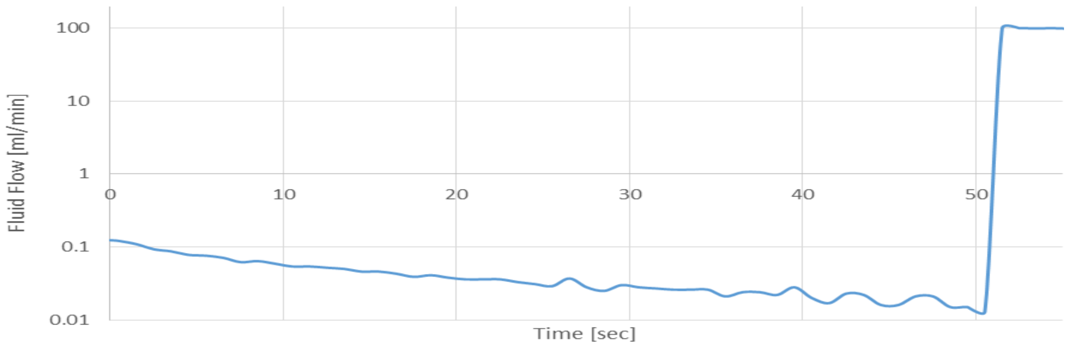

Figure 38: Pressures impact Fluid for Fracking Bentheimer Specimen

This series of experiments show that a very permeable formation needs a high pre-pressured impact due to a too large dissipation of hydraulic fluid. This high impact may originate from human-made equipment or fracture propagation reaching the permeable formation's interface.

3.5.2 Fluid Fracturing Pressures versus Time during the Hydraulic Injection Experiments

Figure 39 visualises a pressure versus time graph in logarithmic scale. The injection rate (100ml/min) is given above the graph, the hydraulic fluid flow holds at Shut-In conditions. Both pressure curves follow the same trend until the closure pressure is reached. After closure pressure, the pressure of the set-up increases again till Shut In, since the hydraulic fluid can't leave the closed system. After Shut In the pressure will decrease slowly due to fluid dissipation into the specimen. The specimen loses the ability to further prograde the fracture since the hydraulic fluid has partly dissipated into the formation and increased the confining and pore pressure. This ability loss was discovered within the set-up by re-injection of hydraulic fluid after fracture initiation.

The field conditions assume that between the closing and Shut In pressure; fracture, fluid and rock will all come to a balanced and stable condition. The existing pressure is exactly the required pressure for fracture propagation and injected volume equals the generated fracture volume. As soon as the Shut-In is initiated an immediate pressure drop occurs, fracture propagation will hold in the absence of the required pressure difference. The fractures will close and the fracturing fluid will decrease in pressure after Shut In due to fluid backflow into well and rock penetration, (Soltanzadeh, 2015).

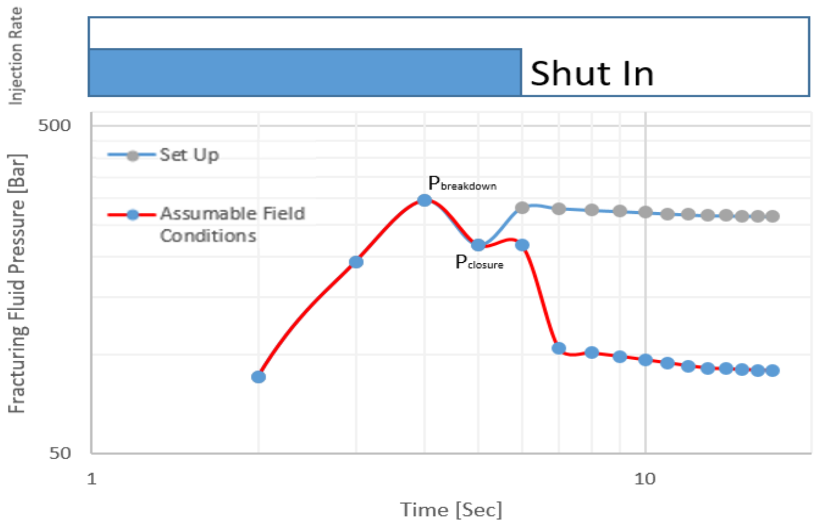

Figure 39: Fracturing Fluid Pressure versus Time for Set-Up and Field Condition for Layered Specimen 11

Figure 40 contains a graph with injection time versus hydraulic fracturing fluid pressure (I) and a table with corresponding breakout and axial pressures (II) of the Ainsa Sandstone. Related specimen number is given between brackets. Figure 40(I) shows that all specimens except layered sample two reach the maximum pumping pressure of 517 bar. Nevertheless, the specimen still breaks after some time due to a lower increase in local pressure difference.

Figure 40 (II) shows the breakout and closing pressure of each sample respectively at an axial pressure of 3 bar. An average breakout pressure of 514 bar has been found for the Ainsa sandstone at an axial pressure of 3 bar. The Ainsa layered samples with Bentheimer as middle layer have an average closing pressure of 123 bar, where a fracture propagated through the interface. Low porosity Fontaine Bleau as middle layer reached an average closing pressure of 208 bar, the fracture did not prograde through the interface. The closing pressure of a mono-lithologic Ainsa sandstone is found to be 303 bar. The closing pressure of the Ainsa sandstone without fracture propagation through the interface is lower than the closing pressure of the mono-lithologic Ainsa sandstone, due to fluid leak-off along with the interface.

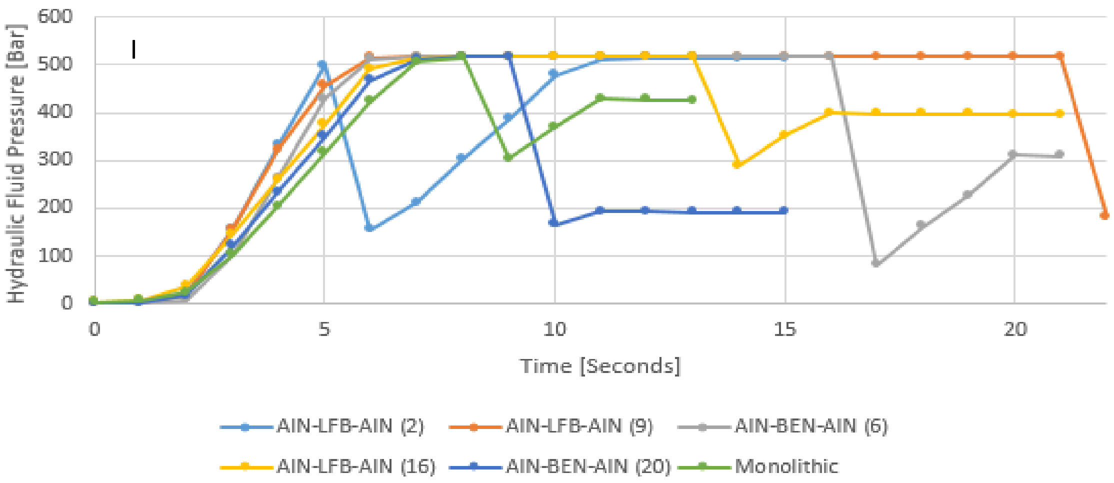

II	Fracture Pressure [bar]	Mechanical Contrast	Closing Pressure [bar]	Fractured Interface	Porosity [%]
AIN-LFB-AIN (2)	499.4	0.6	156	No	1.6
AIN-LFB-AIN (9)	517	0.6	180	No	2.9
AIN-BEN-AIN (6)	517	0.3	81	Yes	2.5
AIN-LFB-AIN (16)	517	0.6	289	No	1.8
AIN-BEN-AIN (20)	517	0.3	165	Yes	1.9
Mono-lithologic AIN	515.8		303		1.9
Average	514				

Figure 40: Experimental Injection Pressure Data of Ainsa Sandstone at an Axial Pressure of 3 Bar, (I) Time versus Hydraulic Fracturing Fluid Pressure of the Different Tested Sample Configurations, (II) Breakout and Closing Pressure of the Specimen corresponding to the Graph.

Figure 41 visualises the pressure difference between the injection and hydraulic piston pressure. The pressure difference equals a distance of approximately 2 centimetres, giving an indication of the local pressure difference. The Figure shows that when the porosity increases, the experiment run time till fracture initiation increases as well. When the fracture was initiated, the piston pressure equals the injection pressure causing the pressure difference to equal approximately zero, since the hydraulic injection fluid reaches the piston through the fracture instantaneously. The reason why the experiment's run time until fracture increases with increasing permeability can be explained by the relation between permeability and pressure build-up. An increase in porosity results in an increase in permeability. It takes approximately 4 seconds to build up a pressure of around 500 bar, the higher the permeability the further the pressured fluid will infiltrate the specimen within those 4 seconds. The pressure build-up goes faster than the fluid can dissipate the pressure through the specimen, resulting in a delayed local pressure difference that is able to fracture the specimen. The larger the permeability, the further the fluid dissipates throughout the sample till critical tensile stress values are surpassed. In conclusion, the pressure build-up is faster than the hydraulic fluid can dissipate throughout the sample, resulting in a delayed critical local pressure difference linked to the specimen's permeability.

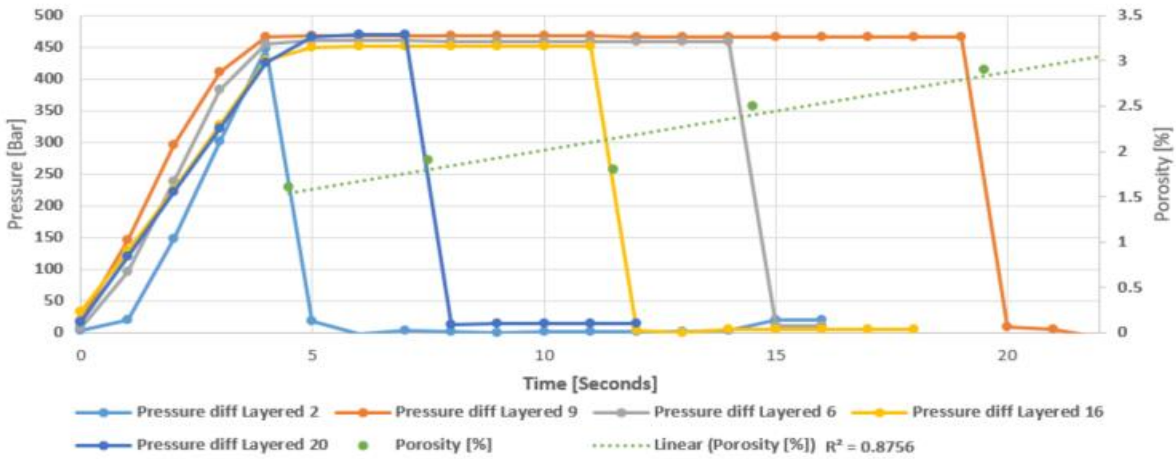

Figure 41: Pressure Difference between Injection Pressure and Sleeve Pressure of Specimens denoted in Figure 40 (II) and Porosity versus Experiment Run Time

Figure 42 visualises the hydraulic fluid and pore pressure measurements versus experiment run time for layered specimen AIN-LFB-AIN (2). A linear pore pressure build-up can be observed before and after fracture initiation at 4 seconds of experimental run time. Linear section I is obtained by a combination of hydraulic injection fluid dissipation throughout the specimen and the resistance against the hydraulic piston by a pressure build-up on approximately 1/10 of the specimen's surface due to the fluid injection. Linear section II is obtained through pressuring the hydraulic fluid in the newly created fracture. The hydraulic fluid pressure reaches the hydraulic piston and sleeve, resulting in a low-stress difference. The creation of new fractures within the fractured medium in the hydraulic injection setup is impossible due to too low-stress differences after fracture initiation.

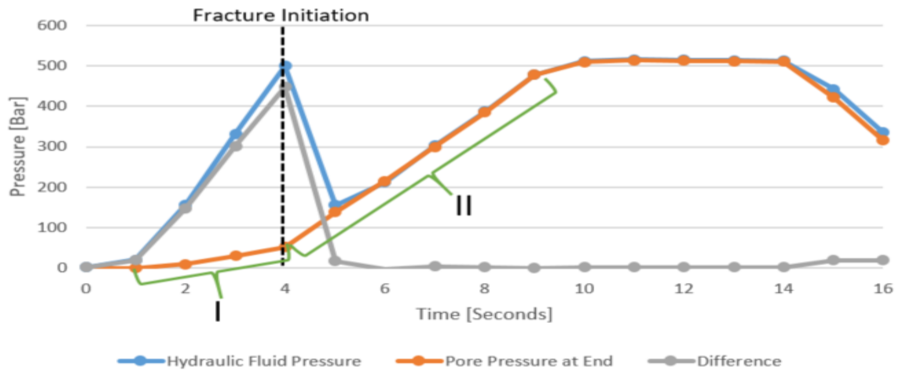

Figure 42: Hydraulic Fluid and Pore Pressure Measurements with Corresponding Pressure Difference versus Experiment Run Time

Figure 43 contains a graph with injection time versus the hydraulic fracturing fluid pressure (I) and a table with corresponding breakout and closure pressures (II). Figure 43(I) shows that a configuration with high porosity Fontaine Bleau, the fractures prograde through the interface with an average pressure of 440 Bar. The closing pressure of the sample where the fracture prograde through the interface is lower due to higher permeability values.

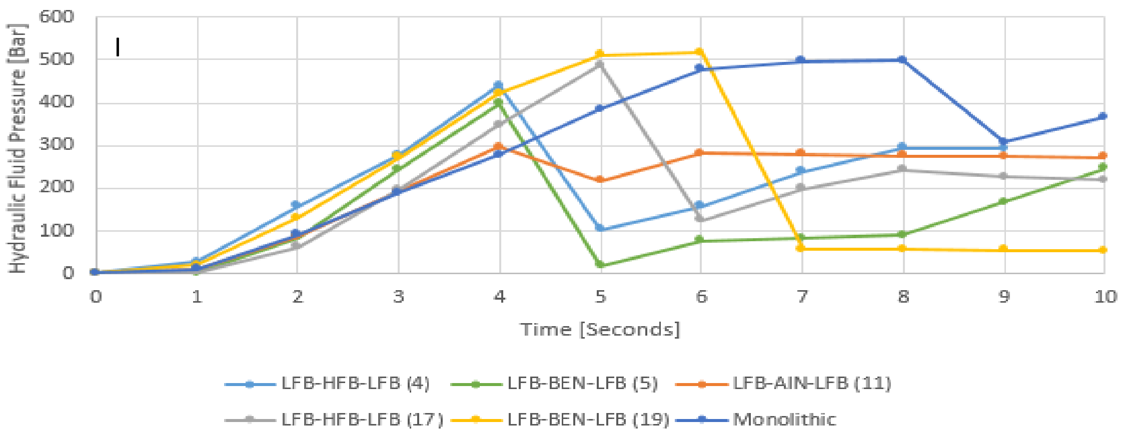

II	Fracture Pressure [bar]	Mechanical Contrast	closing pressure [bar]	Fractured through Interface
LFB-HFB-LFB (4)	440	0.4	104	Yes
LFB-BEN-LFB (5)	398	0.4	18	Yes
LFB-AIN-LFB (11)	296	1.6	217	No
LFB-HFB-LFB (17)	487	0.4	126	Yes
LFB-BEN-LFB (19)	517	0.4	57	Yes
Mono-lithologic LFB	499		307	
Average	440			

Figure 43: Experimental Injection Pressure Data of Low Porosity Fontaine Bleau Sandstone at an Axial Pressure of 2 Bar, (I) Time versus Hydraulic Fracturing Fluid Pressure of the Different Tested Sample Configurations, (II) Breakout and Closing Pressure of the Specimen corresponding to the Graph.

Figure 44 contains a graph with injection time versus hydraulic fracturing fluid pressure (I) and a table with corresponding breakout and axial pressures (II). Figure 44(I) shows that all layered samples experienced almost the same breakout pressure and closing pressure with the exception of sample number 1. The closure pressures are all very low, due to the high permeability of the Bentheimer and high porosity Fontaine Bleau.

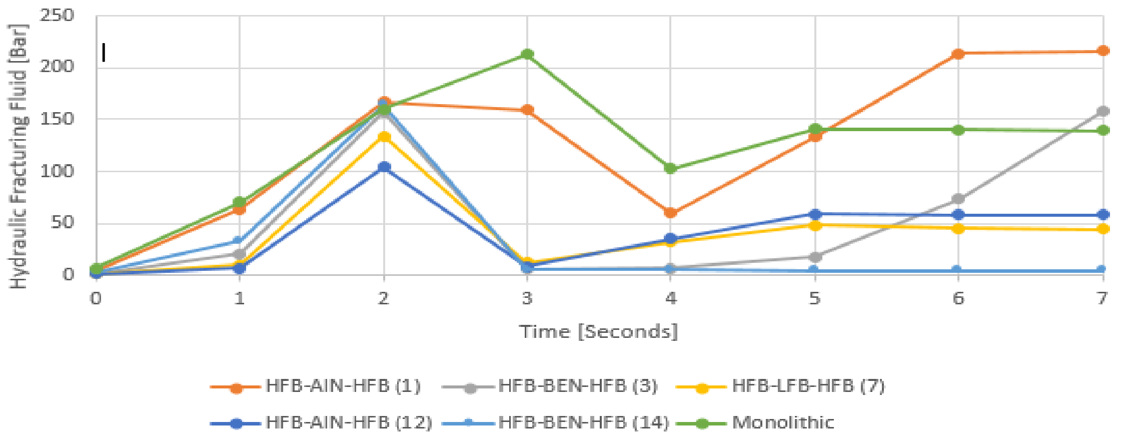

II	Fracture Pressure [bar]	Mechanical Contrast	closing pressure [bar]	Fractured through Interface
HFB-AIN-HFB (1)	167	3.7	60	No
HFB-BEN-HFB (3)	157	1	6	Yes
HFB-LFB-HFB (7)	134	2.3	12	No
HFB-AIN-HFB (12)	104	3.7	9	No
HFB-BEN-HFB (14)	164	1	6	Yes
Mono-lithologic HFB	213		103	
Average	156			

Figure 44: Experimental Injection Pressure Data of High Porosity Fontaine Bleau Sandstone at an Axial Pressure of 2 Bar, (I) Time versus Hydraulic Fracturing Fluid Pressure of the Different Tested Sample Configurations, (II) Breakout and Closing Pressure of the Specimen corresponding to the Graph.

Figure 45 visualises the hydraulic fluid and pore pressure measurements versus experiment run time for the mono-lithologic Bentheimer specimen during an on sample pressure build-up. The Figure shows that the pore pressure of the highly permeable specimen increases as fast as the hydraulic injection pressure. This results in a very low local pressure difference. To initiate a fracture within the Bentheimer sandstone a pre-pressured fluid is injected.

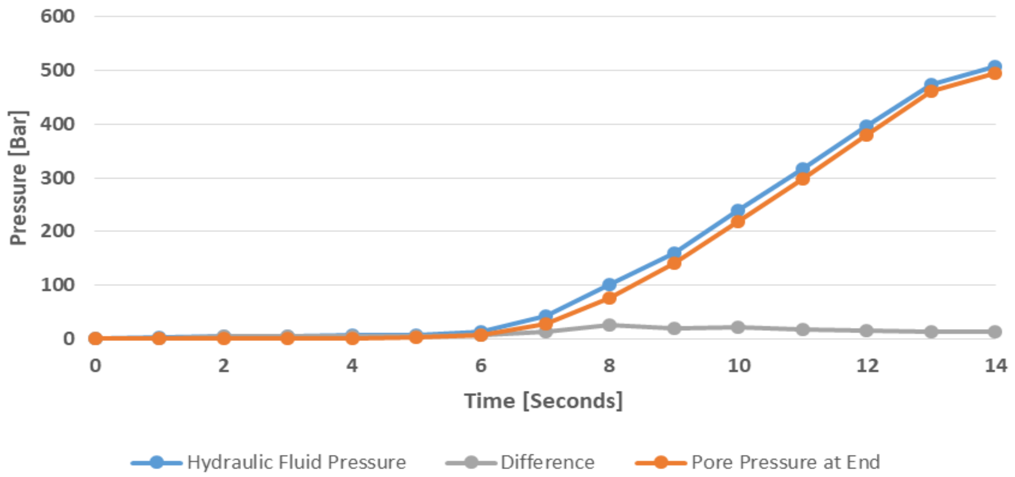

Figure 45: Hydraulic Fluid and Pore Pressure Measurements with Corresponding Pressure Difference versus Experiment Run Time of Mono-Lithologic Bentheimer Sandstone

3.5.3 Fracture Propagation and Containment Visualised by Micro-CT

Confined hydraulic fluid injections tests were carried out to create tensile stress-driven fractures in the synthetic layered rock samples. Micro-CT scans were used to visualise the different fracture propagations and patterns, these scans are shown within this paragraph.

Figure 46 (II) shows the non-interpreted micro-CT slice of the fracture area and the time versus hydraulic fluid pressure graph used for breakout and closing pressure of sample LFB-AIN-LFB (11). Figure 46 (I) shows an interpreted micro-CT slice by a red dashed line. The sample consists out of a layering in the order of low porosity Fontaine Bleau, Ainsa and low porosity Fontaine Bleau sandstone. The Fontaine Bleau being the weakest constituent and Ainsa the strongest in this combination, resulting in a mechanical contrast in tensile stress of 1.6. Two major fractures are formed within the weaker top layer at a breakout pressure of 296 bar, none of them prograde through the interface and are arrested before the interface.

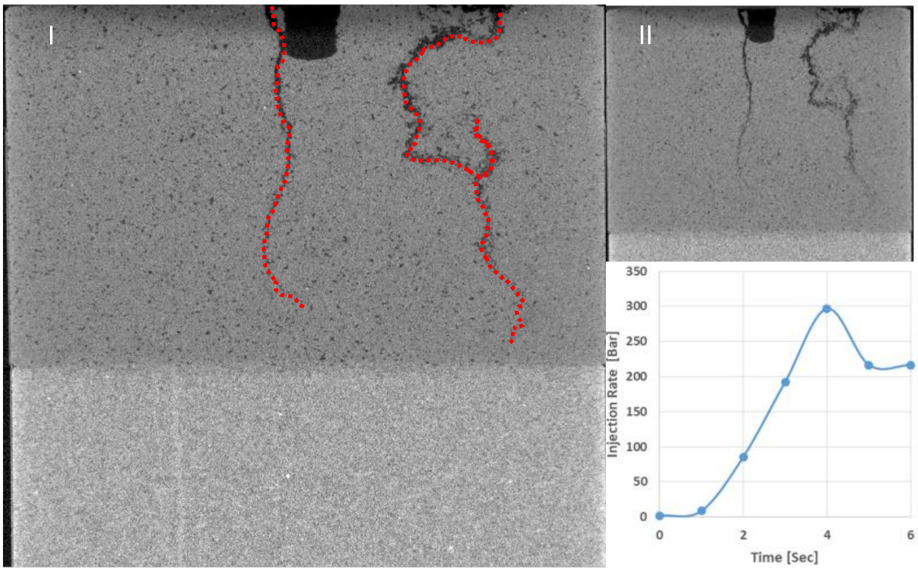

Figure 46: One Micro-CT Slice and Time versus Hydraulic Fluid Pressure Graph of Sample LFB-AIN-LFB (11), Figure (I) shows the Fracture Propagation Highlighted in Red and Figure (II) shows the non-Interpreted Fracture Propagation.

Figure 47, layered sample HFB-AIN-HFB (12) consists out of a layering in the order of high porosity Fontaine Bleau, Ainsa and high porosity Fontaine Bleau sandstone. The Fontaine Bleau being the weakest constituent and Ainsa the strongest in this combination, resulting in a mechanical contrast in tensile stress of 3.7. One major fracture is formed within the weaker top layer at a breakout pressure of 104 bar, which is arrested at the interface.

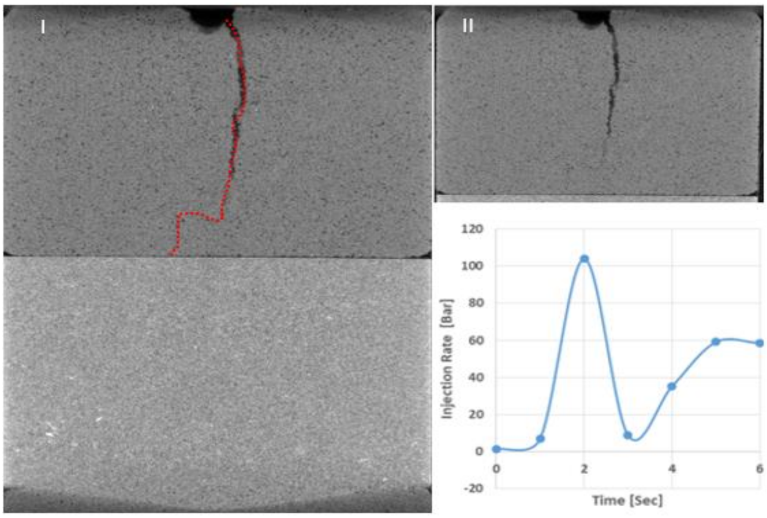

Figure 47: One Micro-CT Slice and Time versus Hydraulic Fluid Pressure Graph of Sample HFB-AIN-HFB (12), Figure (I) shows the Fracture Propagation Highlighted in Red and Figure (II) shows the non-Interpreted Fracture Propagation.

Figure 48, layered sample BEN-AIN-BEN (15) consists out of a layering in the order of Bentheimer, Ainsa and Bentheimer sandstone. The Bentheimer being the weakest constituent and Ainsa the strongest in this combination, resulting in a mechanical contrast in tensile stress of 3.7. A major fracture is formed within the weaker top layer at a breakout pressure of 106 bar, which does not prograde through the interface and is arrested at the interface.

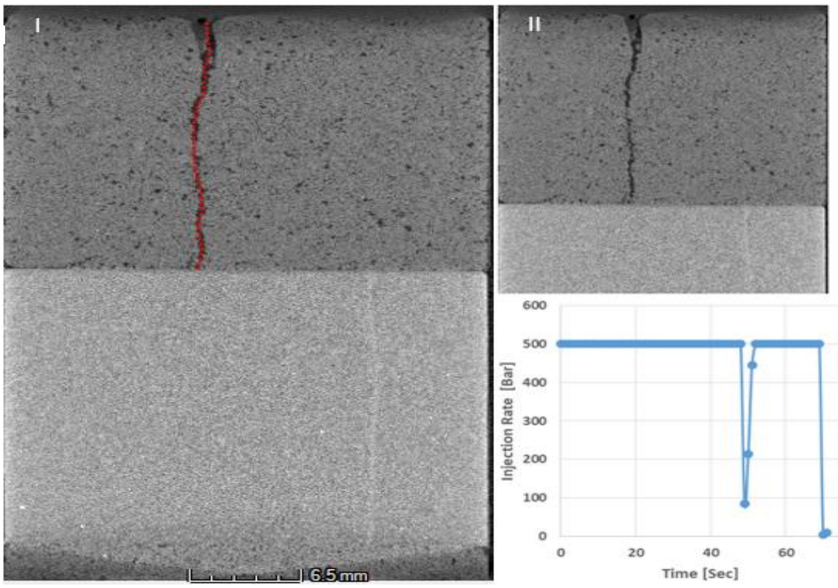

Figure 48: One Micro-CT Slice and Time versus Hydraulic Fluid Pressure Graph of Sample BEN-AIN-BEN (15), Figure (I) shows the Fracture Propagation Highlighted in Red and Figure (II) shows the non-Interpreted Fracture Propagation.

Figure 49, layered sample AIN-LFB-AIN (16) consists out of a layering in the order of Ainsa, low porosity Fontaine Bleau and Ainsa sandstone. The Fontaine Bleau being the weakest constituent and Ainsa the strongest in this combination, resulting in a mechanical contrast in tensile stress of 0.6. Two major shear fractured is formed within the weaker top layer at a breakout pressure of 517 bar. These fractures are combining into one major fracture which does not prograde through the interface and is arrested and deflected along with the interface.

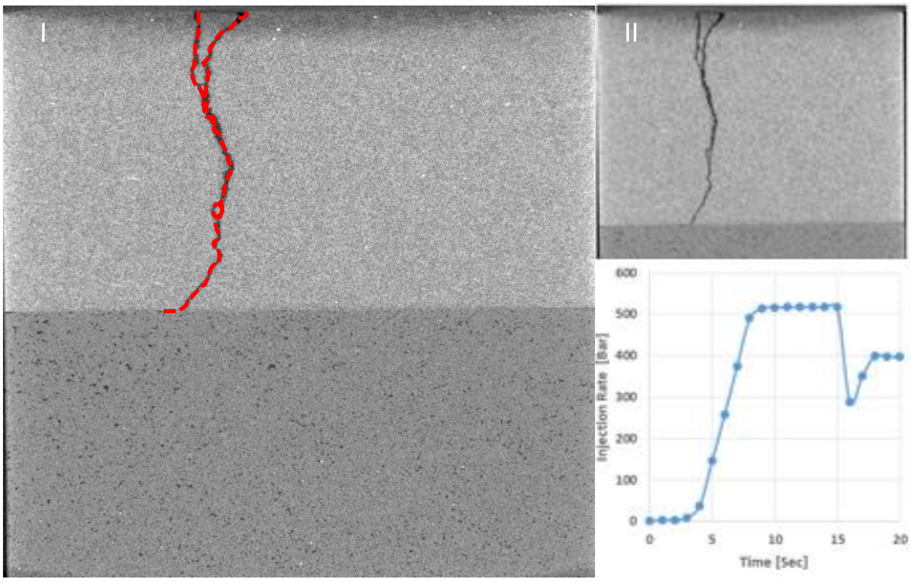

Figure 49: One Micro-CT Slice and Time versus Hydraulic Fluid Pressure Graph of Sample AIN-LFB-AIN (16), Figure (I) shows the Fracture Propagation Highlighted in Red and Figure (II) shows the non-Interpreted Fracture Propagation.

Figure 50, layered sample AIN-BEN-AIN (20) consists out of a layering in the order of Ainsa, Bentheimer and Ainsa sandstone. The Bentheimer being the weakest constituent and Ainsa the strongest in this combination, resulting in a mechanical contrast in tensile stress of 0.3. One major fracture is formed within the stronger top layer at a breakout pressure of 517 bar, which prograde through the interface and is arrested within the mechanically weaker layer.

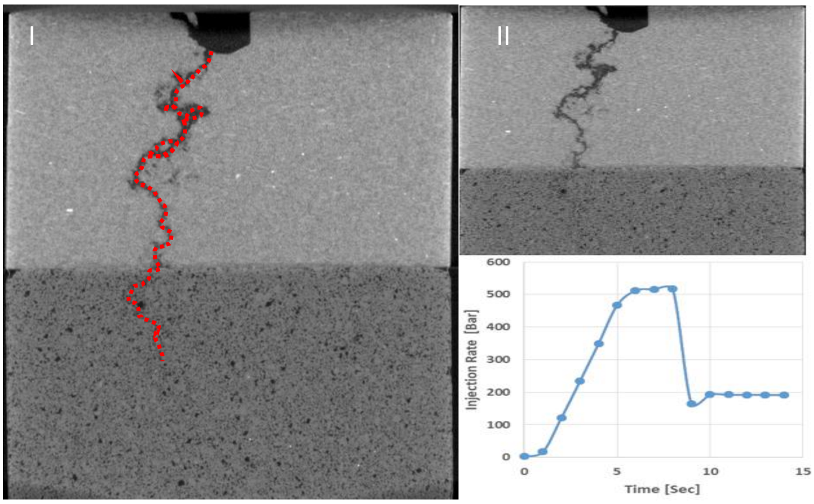

Figure 50: One Micro-CT Slice and Time versus Hydraulic Fluid Pressure Graph of Sample AIN-BEN-AIN (20), Figure (I) shows the Fracture Propagation Highlighted in Red and Figure (II) shows the non-Interpreted Fracture Propagation.

Figure 51, layered sample LFB-HFB-LFB (17) consists out of a layering in the order of low porosity Fontaine Bleau, high porosity Fontaine Bleau and low porosity Fontaine Bleau sandstone. The high porosity specimen being the weakest constituent and the low porosity specimen being the strongest in this combination, resulting in a mechanical contrast in tensile stress of 0.4. One major fractured is formed within the stronger top layer at a breakout pressure of 487 bar, which prograde through the interface and is arrested within the second layer.

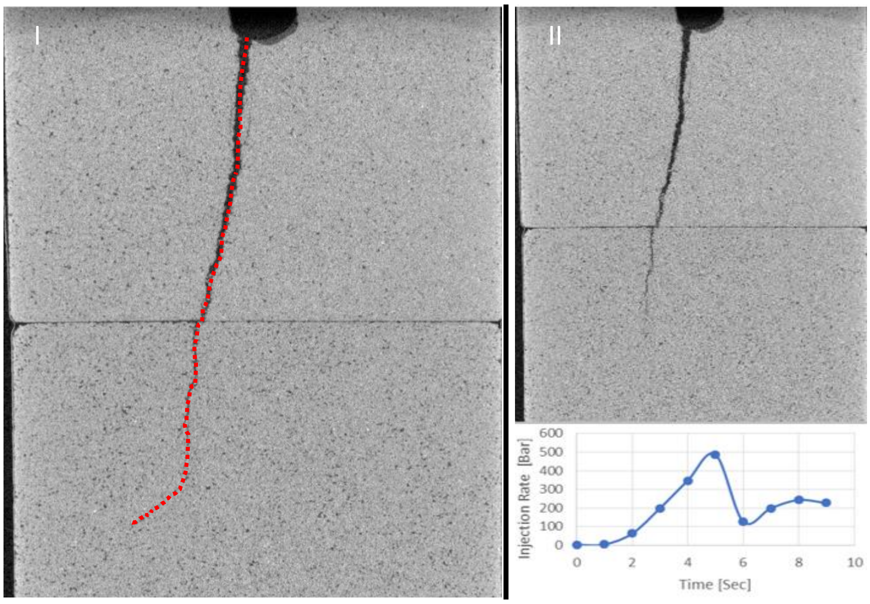

Figure 51: One Micro-CT Slice and Time versus Hydraulic Fluid Pressure Graph of Sample LFB-HFB-LFB (17), Figure (I) shows the Fracture Propagation Highlighted in Red and Figure (II) shows the non-Interpreted Fracture Propagation.

Figure 52, layered sample LFB-BEN-LFB (19) consists out of a layering in the order of low porosity Fontaine Bleau, Bentheimer and low porosity Fontaine Bleau sandstone. The Bentheimer being the weakest constituent and Fontaine Bleau the strongest in this combination, resulting in a mechanical contrast in tensile stress of 0.4. One major fracture is formed in the stronger top layer at a breakout pressure of 517 bar, which prograde through the interface and is arrested in the mechanically weaker layer.

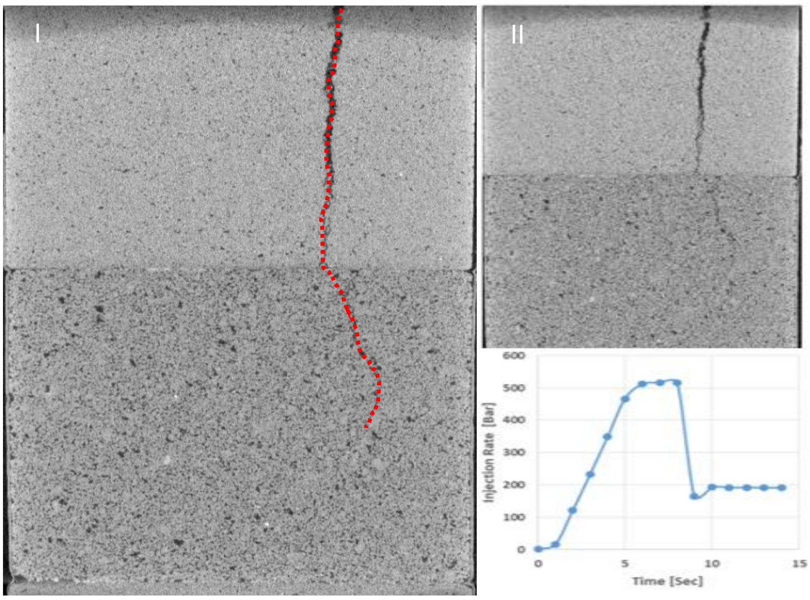

Figure 52: One Micro-CT Slice and Time versus Hydraulic Fluid Pressure Graph of Sample LFB-BEN-LFB (19), Figure (I) shows the Fracture Propagation Highlighted in Red and Figure (II) shows the non-Interpreted Fracture Propagation.

Figure 53, layered sample LFB-BEN-LFB (5) consists out of a layering in the order of low porosity Fontaine Bleau, Bentheimer and low porosity Fontaine Bleau sandstone. The Bentheimer being the weakest constituent and Fontaine Bleau the strongest in this combination, resulting in a mechanical contrast in tensile stress of 0.4. One major fracture is formed in the stronger top layer at a breakout pressure of 398 bar, which prograde through the interface and is arrested in the mechanically weaker layer.

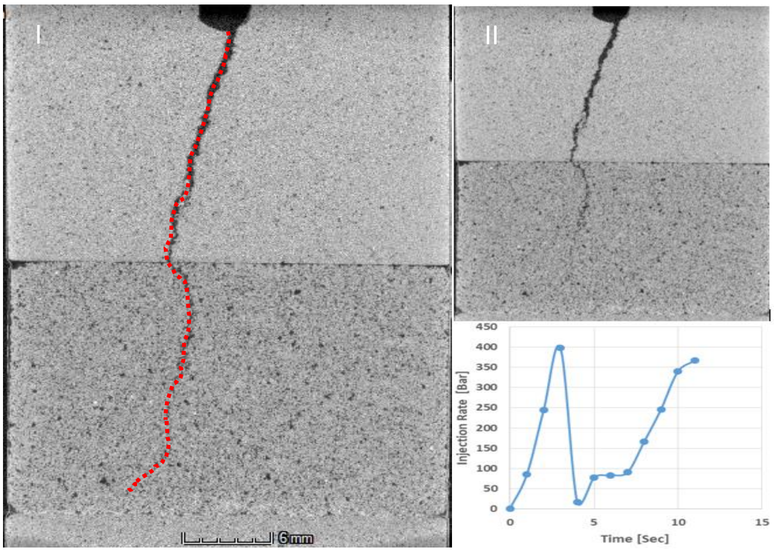

Figure 53: One Micro-CT Slice and Time versus Hydraulic Fluid Pressure Graph of Sample LFB-BEN-LFB (5), Figure (I) shows the Fracture Propagation Highlighted in Red and Figure (II) shows the non-Interpreted Fracture Propagation.

Figure 54, layered sample AIN-BEN-AIN (6) consists out of a layering in the order of Ainsa, Bentheimer and Ainsa sandstone. The Bentheimer being the weakest constituent and Ainsa the strongest in this combination, resulting in a mechanical contrast in tensile stress of 0.3. One major fracture is formed in the stronger top layer at a breakout pressure of 517 bar, which prograde through the interface and is arrested at the second interface.

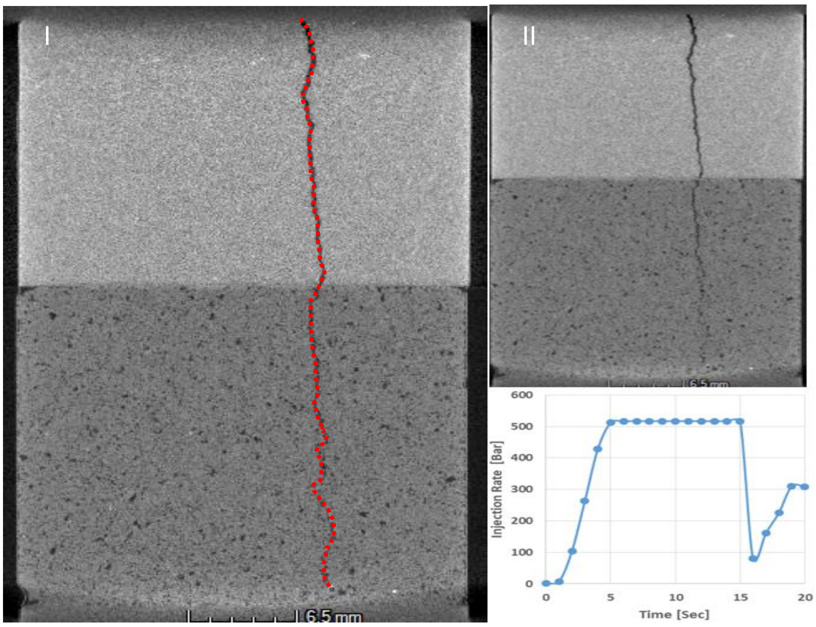

Figure 54: One Micro-CT Slice and Time versus Hydraulic Fluid Pressure Graph of Sample AIN-BEN-AIN (6), Figure (I) shows the Fracture Propagation Highlighted in Red and Figure (II) shows the non-Interpreted Fracture Propagation.

Figure 55, layered sample HFB-BEN-HFB (14) consists out of a layering in the order of high porosity Fontaine Bleau, Bentheimer and high porosity Fontaine Bleau sandstone. Both formations are equally strong in this combination, resulting in a mechanical contrast in tensile stress of 1. One major fracture is formed in the top layer at a breakout pressure of 164 bar, which prograde through the interface and is arrested in the mechanically weaker layer.

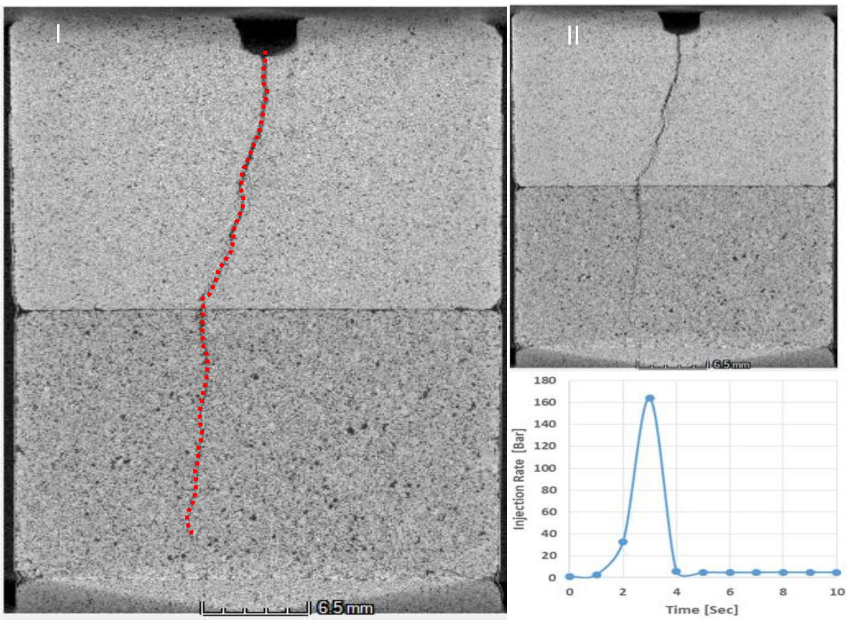

Figure 55: One Micro-CT Slice and Time versus Hydraulic Fluid Pressure Graph of Sample HFB-BEN-HFB (14), Figure (I) shows the Fracture Propagation Highlighted in Red and Figure (II) shows the non-Interpreted Fracture Propagation.

3.5.4 Fracture Propagation with increasing and decreasing Mechanical Contrast

Figures I till VI in Table 11 are shown with the corresponding pressure curve and non-interpreted Micro-CT scan slices in the corresponding figures in subparagraph 3.5.3 Fracture Propagation and Containment Visualised by Micro-CT. The Bentheimer and high porosity Fontaine Bleau are not possible to be fractured by an on sample pressure build-up due to the permeability. That means that the breakout pressure of figures I till III acts as a pre-pressured fluid injection at the interface. The first layer is fractured by the formation's critical pore pressure difference, the fracture will propagate through the formation's interface since the pressure difference exceeds the required pressure difference of the second layer. The second interface has never been propagated by the fracture since the fluid can dissipate or fracture the second layer easier than the mechanically stronger third layer. Pressure loss is neglectable as shown in sub-paragraph 3.5.2: Pressure Loss within propagated Fracture.

Table 11: Micro-CT Slices of Hydraulic Fractured Layered Specimen, where Propagation went through Interface. Figures I till VI are visualised in increasing Mechanical Contrast (M.C.), where B.P. = Breakout Pressure, LFB = Low Porosity Fontaine Bleau, HFB = High Porosity Fontaine Bleau, AIN = Ainsa and BEN = Bentheimer.

Length (mm)	(I) M.C. = 0.3 AIN-BEN (20) B.P. = 517 Bar	(II) M.C. = 0.3 AIN-BEN (6) B.P. = 517 Bar	(III) M.C. = 0.4 LFB-BEN (5) B.P. = 398 Bar	(IV) M.C. = 0.4 LFB-HFB (17) B.P. = 487 Bar	(V) M.C. = 0.4 LFB-BEN (19) B.P. = 517 Bar	(VI) M.C. = 1 HFB-BEN (14) B.P. = 164 Bar

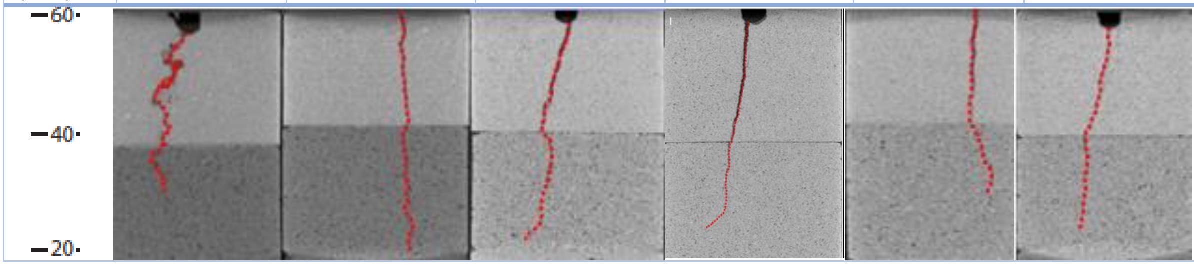

Figures I till IV in Table 12 show that if the fracture is started in a formation requiring a lower local pore pressure difference than the second layer, the fracture will be arrested at the interface. Figure IV is more remarkable, because the fracture did not propagate through the interface although the second layer is weaker in terms of critical tensile stress, but choose to continue along with the interface instead.

Table 12: Micro-CT Slices of Hydraulic Fractured Layered Specimen, where Propagation arrested at Interface. Figures I till IV are visualised in decreasing Mechanical Contrast (M.C.), where B.P. = Breakout Pressure, LFB = Low Porosity Fontaine Bleau, HFB = High Porosity Fontaine Bleau, AIN = Ainsa and BEN = Bentheimer.

Length (mm)	(I) M.C. = 3.7 HFB-AIN (12) B.P. = 104	(II) M.C. = 3.7 BEN-AIN (15) B.P. = 106	(III) M.C. = 1.6 LFB-AIN (11) B.P. = 296	(IV) M.C. = 0.6 AIN-LFB (16) B.P. = 517

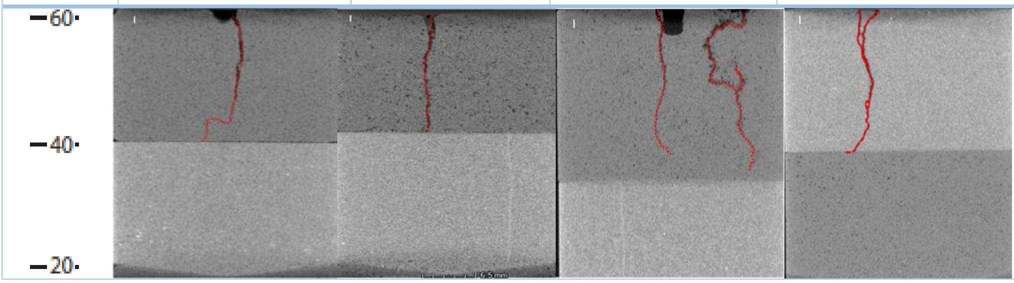

From the above observation, it can be concluded that a fracture initiated by a hydraulic fluid pressure build-up in a mechanically stronger rock will also fracture a mechanically weaker rock. By a hydraulic fluid pressure build-up in the mechanically weaker rock, the originated fractured will not propagate through the mechanically stronger rock since the required mono-lithologic fracture pressure is not met, a new pressure build-up is required in the fracture. However, if the fracture pressure is increased again, the fracture will preferably propagate in the mechanically weaker formation. Fracture propagation will take the path of least resistance. From the results it can be concluded that by pressuring of the more permeable formation, a high enough pressure difference at the interface can be created, resulting in the creation of a fracture into the lower permeable and mechanically stronger formation. However, this scenario could not be created by the hydraulic fluid injection set-up, since water saturated the entire closed system through the higher permeable specimen or created fracture. This saturation of the triaxial cell increases the confining pressure on the synthetic layered sample, resulting in a higher required pressure difference.

4 Discussion

This study examines the propagation and continuity of the fractures in an artificial heterogeneous layered system depending on the mechanical properties of the layers. This chapter will discuss hydraulic fracture initiation and propagation in subsurface conditions.

4.1 Hydraulic Fracture Initiation

The used hydraulic fluid injection setup initiates a fracture by point source injection. During point source conditions, the injected hydraulic fluid will penetrate the specimen into all directions at the location of injection. At these conditions, the local stress difference creates a tensile force into all directions, where the horizontal direction holds the least resistance due to the positioned pistons above and below and an expandable sleeve surrounding the specimen. The fracture will be initiated at the corner of the perforation, where the weakest critical horizontal tensile force exists. A vertical fracture is created. After fracture initiation, the pressure will build up at the interface. At the interface, the conditions will change from point to line source if the initial fracture propagation did not hold enough energy to propagate through the interface. Equal stress distribution over the specimen's cross-sectional area will exist. This phenomenon is verified by the observation in layered sample AIN-LFB-AIN (16) and is visualised in Figure 56. The fracture is initiated in the slightly mechanical stronger Ainsa sandstone. Due to line source conditions, it does not hold enough energy to fracture the mechanical weaker low porosity Fontaine Bleau sandstone. Fracture initiation is different during point and line sources conditions, due to the stress distribution over the specimen's cross-sectional area. During line source conditions, an equal stress distribution over the specimen's cross-sectional area exists. The injected hydraulic fluid will penetrate the specimen across the entire cross-sectional area at a similar rate. At these conditions, the global stress difference creates a tension force into the vertical direction, "pushing the secondary formation away". If this pressure difference is large enough to surpass critical values, the fracture will propagate through the interface. If this pressure difference is not larger enough, the fracture can propagate along with the interface as observed in Figure 50(I).

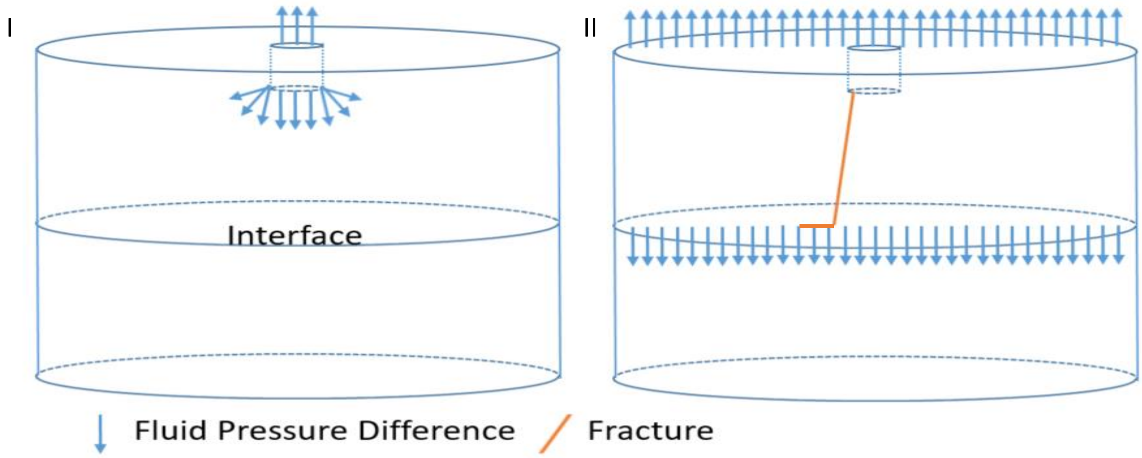

Figure 56: Schematic version of Local Pressure Difference in Layered Sample AIN-LFB-AIN (16) after (II) and before (I) fracture Initiation.

Verification of these findings can be found by another author, (Taheri-Shakib, et al., 2015). Figure 57 visualises that a critical local fluid pressure difference results in a fracture initiation perpendicular to the critical tensile stress. The fracture will stop if the tensile stress falls below critical values. The fracture will either propagate through or arrest at natural fractures or other mechanical contrasts. The fracture will propagate through the mechanical contrast if the required critical tensile stress level is surpassed. Otherwise, the fracture will arrest or deflect in different directions.

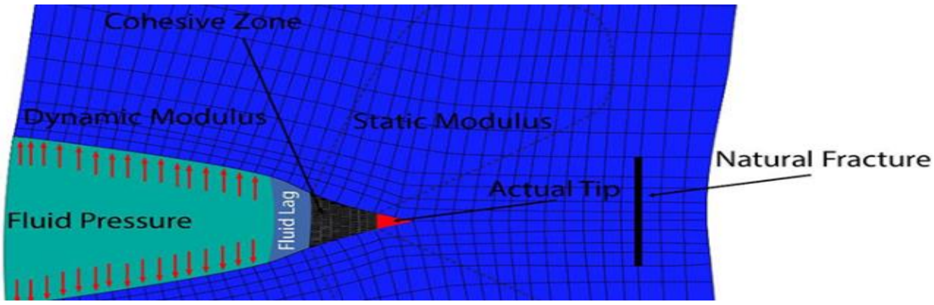

Figure 57: Fracture Initiation and Propagation by Local Pressure Difference, (Taheri-Shakib, et al., 2015)

4.2 Hydraulic Fracture Propagation at Interface

For the synthetic layered samples, it has been shown that a hydraulic fracture will initiate when the critical tensile pressure is surpassed. Additionally, it has been shown that a highly permeable specimen results in quick sample saturation by quick fluid dissipation, decreasing the local pore fluid pressure difference. In order to fracture permeable specimens, it was shown that a pre-pressured or higher viscose fluid was needed. Verification of these findings can be found by many other authors, (Chuprakov, et al., 2013; Kresse, et al., 2013). The ability of fracture propagation through the formation's interface is linked to the ability to exceed the critical tensile stress value of the second lithology.

The rock specimen will fracture if and only if the pressure difference surpasses the critical tensile stress. Results show that during hydraulic pressuring of the mechanical stronger formation, the critical tensile stress levels of the weaker formation will be surpassed. During hydraulic pressuring the mechanical weaker formation, only the critical tensile stress levels of the weaker formation will be surpassed. The fractures are arrested at the formation's interface. The ability for fractures to propagate through the interface relates to the mechanical contrast versus the tensile strength of the strongest formation and is visualised in Figure 58. Fracture propagation from a mechanically weak to strong formation is characterised by a mechanical contrast larger than 1. Fracture propagation from a mechanically strong to weak formation is characterised by a mechanical contrast smaller than 1.

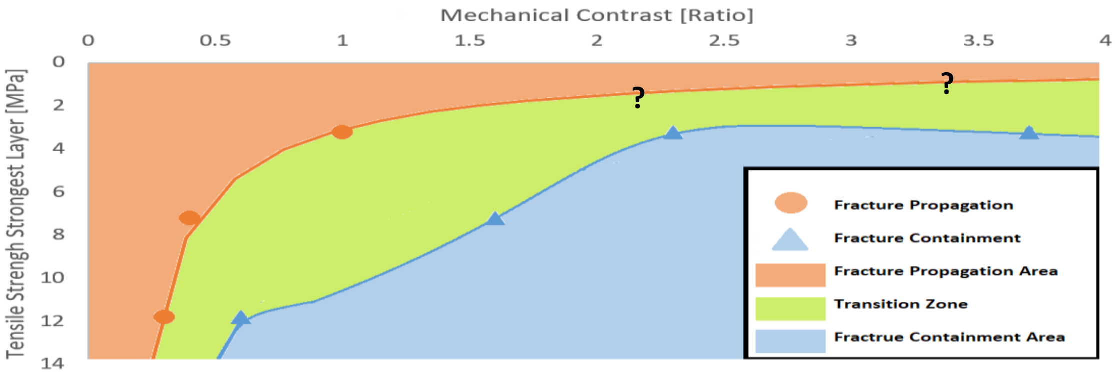

Figure 58: Ability for Fractures to Propagate through the Interface in relation with the Mechanical Contrast [Ratio] versus the Tensile Strength of the Strongest Layering [MPa] based on a Total of 15 Experiments. The Boundary of the Fracture Propagation Area at high Mechanical Contrasts is not yet defined and the question marks visualise the Possibility of New Data Points.

The arrested fractures will propagate through the interface of a weak to strong formation if and only if the pressure difference at the interface surpasses the critical tensile stress of the mechanically stronger formation. However, by creating a new pressure differences in the mechanical weaker formation, the fracture will preferably propagate in the formation itself. Fracture propagation will take the path of least resistance.

The experimental results suggest that fracture propagation from weak to strong formation is possible by pressuring the formation's global pore fluid of the mechanical weaker formation. This is possible if the mechanical weaker formation is significantly higher in permeability, resulting in a pressure build-up and difference at the interface. Verification is found by Chuprakov, et All (2013). Stating that at a T-shape fracture, the pressure initially drops quickly but after saturation is bound to grow. This rebound time is strongly depending on the permeability of the formation after the interface and to a much lesser extent by the fluid pressure at the interface, (Chuprakov, et al., 2013).

4.3 The Implication on the Hydraulic Fracturing of Petroleum Reservoirs

The results from the experiment have a couple of implications on the ability of hydraulic fracturing inter-bedded and traditional reservoirs:

- It has been found that a point source instead of line source conditions can be created by using a perforation in the lithology. A lower pressure difference is needed since the pressure difference is able to act in the direction of the lowest critical tensile stress value. Fracture initiation will be perpendicular to the lowest possible critical tensile stress value. The formation has the lowest resistance against failure at the borehole's interface. Therefore, fracture initiation is found to be perpendicular to the borehole. The usage of small perforations reduces the critical tensile stress value of the formation that surrounds the borehole.

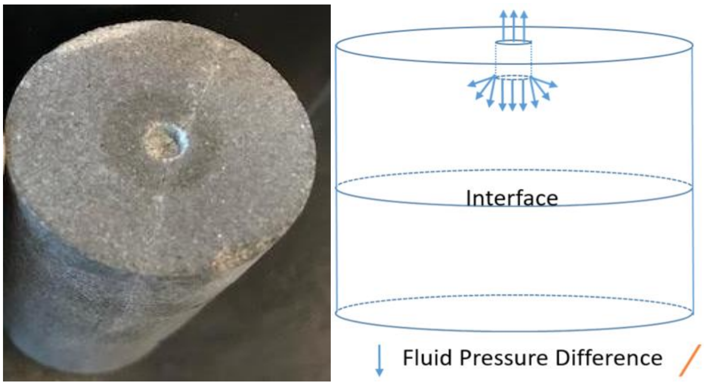

Figure 59: The usage of Perforations to create a Pressure Difference into the required Direction of the lowest Critical Tensile Stress Value.

- During traditional fracturing, a permeable sandstone reservoir lies in an anticlinal[13] fold below a low permeable seal. Fracture propagation will be kept in the mechanical weaker formation. Lower critical local pressure differences are required for the creation of new or propagation of fractures in the mechanical weaker formation. The experimental results suggest that fracture propagation from a weak to strong formation is possible by hydraulic pressuring the formation's global pore pressure, creating a pressure difference at the interface. It can be concluded that the mechanical stronger seal of a traditional reservoir can only be fractured if the reservoir's global pore pressure surpasses the critical tensile pressure value of the seal.
- The injection of a high pressured hydraulic fluid close to the seal is inadvisable since the dissipation rate in relation to the injection rate can be small, creating an interface pore pressure difference. This pore pressure difference will perforate the seal if the critical tensile stress value is surpassed.
- Multiple formations can be perforated in two ways; high energy pre-pressured injection (Figure 60) or by an on formation's global or local pore pressure build-up (Figure 61).

[13] Anticlinal folds are folds that can be characterised by older sediments in the middle and younger sediments on top of the fold.

Figure 60 (I); during a high energy pre-pressured injection, the fracture will instantaneously penetrate multiple layers if and only if the injection pressure surpasses the largest formation's critical tensile stress value. Figure 60 (II); a further hydraulic fluid injection will create a larger fracture network in the mechanical weaker and more permeable formations. Figure 60 (III); the mechanically stronger formation will be fractured if and only if the global pore pressure of the mechanically weaker formation surpasses the critical tensile stress value of the mechanically stronger formation.

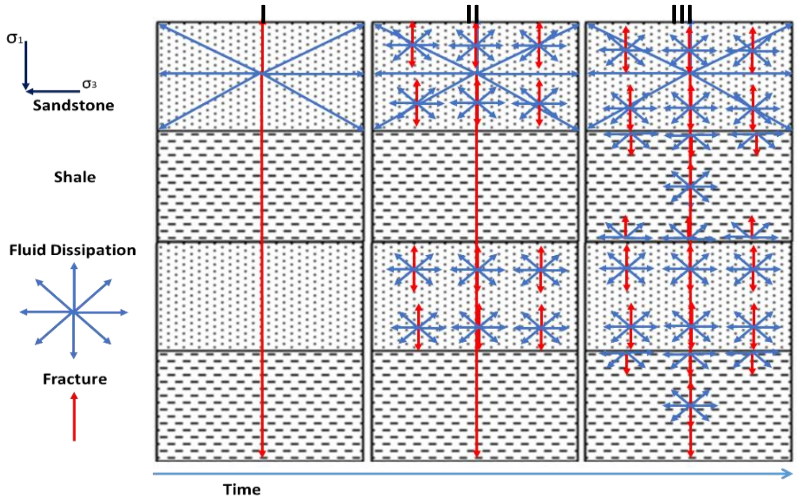

Figure 60: High Energy Pre-pressured Injection, where the Sandstone is the Mechanically Weaker and Shale the Mechanically Stronger Formation. (I) Long Stretched Vertical Fracture initiation by Pre-Pressured Injection, (II) Fluid and Fracture distribution in Mechanical Weaker Formation and (III) Fluid and Fracture distribution in the Mechanically Stronger Formation.

Figure 61 (I); during the formation's global pore pressure build-up, a fracture network will form in the injected formation until critical tensile stress conditions at the formation's interface are exceeded. Figure 61 (III); the fracture network will distribute itself in the newly perforated formation. It is advisable to aim to begin hydraulic fracturing in the mechanically strongest formation since an isotropic fracture network is created until the penetration of the interface. After interface penetration (Figure 61 II and V), hydraulic fluid needs to be injected until the critical stress levels of the stronger formation are exceeded again.

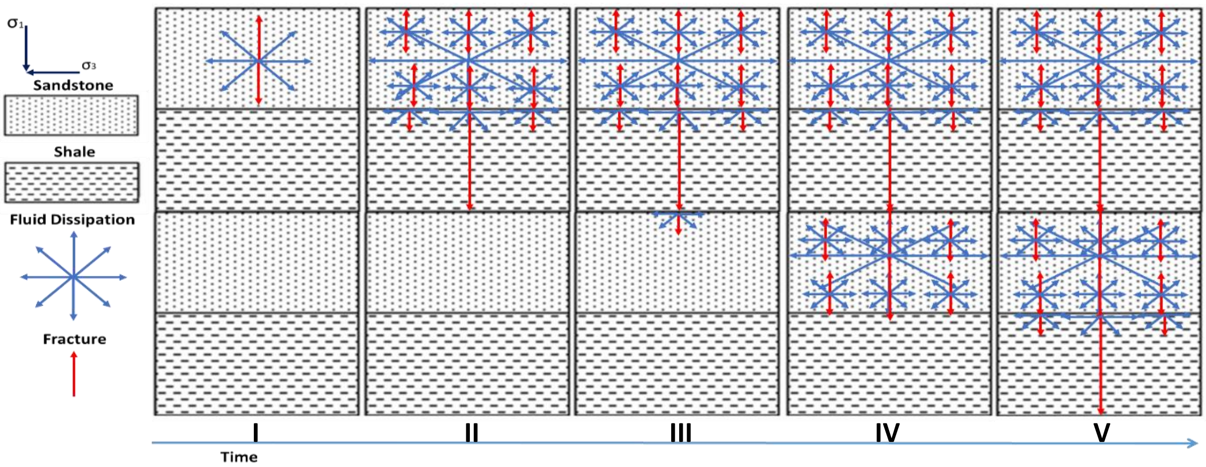

Figure 61: Formation's Global or Local Pore Pressure Build-Up, where the Sandstone is the Mechanically Weaker and Shale the Mechanically Stronger Formation. (I) Fracture and Fluid distribution contained in the Mechanically Weaker Formation by Hydraulic Fluid Injection. (II & III) Critical Tensile Strength of Formation is surpassed, resulting in Fracture and Fluid distribution in Second Formation. (IV) Fluid and Fracture distributes Preferable in the Weaker Newly reached Formation. (V) Distribution of Fractures in the Mechanically stronger Layers stops till Critical Tensile Stress values are reached again.

One of the two methods can be used depending on the desired fracture distribution. A high energy pre-pressured injection will target multiple layers at once. However, a high volume of hydraulic fluid is needed to enlarge the fracture network since multiple layers are targeted at once. The formation's global or local pore pressure build-up will have a large fracture network but will reach fewer layers. Note that to fracture the formation the fluid injection rate needs to be larger than the dissipation rate.

4.4 Slope Cracks and High Hydraulic Head observations

Surface and slope cracks with minor slope displacement were observed in one of the Westerwald clay Quarries. These slope cracks are observed by eye in the stiff clay without the observation of sand clusters. However, thin sand inter-bedded clusters are observed in the Cone Penetration Test (CPT) data as an observed high-pressure head in Inclinometer boreholes. The geotechnical observations in the Lieblich III quarry shows a sandy material at the slope failure plane. The sandy slope failure plane is verified by mineralogy (XRD &XRF) and grain-size distribution (sieving).

By combining the experimental results of the hydraulic fracture propagation at interface conditions, the geotechnical observation of high hydraulic pressured sand clusters and stiff clay crack formations. It can be stated that a fracture can be initiated if the pressure difference between a permeable sand cluster and stiff clay formation is large enough. Observations show that the fractures are initiated by removal of fresh clay from the slope. After removal, the vertical and horizontal pressure on the fresh clay is decreased, decreasing the axial stress. However, the sand's pore fluid pressure is not decreased, since the impermeable clay formation prevents or slows down dewatering. It can be stated that when the sand bar's global pore fluid pressure surpasses the critical tensile strength of the stiff clay, a fracture is initiated. Pore fluid dissipates through the fracture until the pressure differences at interface reach the fracture closing pressure of the confining clay formation. Removal of the clay formation lowers the confining stress and re-opens the fracture.

Hohewieße slope stability simulations show that slope failure is a combination of fracture initiation and a decrease in clay strength by water dissipation into the clay formation. Water dissipation is increased by a decrease in vertical pressure. Verification of in-situ clay weathering can be found by many authors, (Kaixi, et al., 2016; Frederick University, 2017; Skels & Bondars, 2015; Vásárhelyi & Ván, 2006).

Slope and surface cracks can be observed after slope failure. Water dissipates through the newly developed slope cracks. Decreasing the in-situ water pressure relates to an increase in the clay's shear strength parameters and stability. Water dissipation through slope cracks increases slope stability and holds slope movement. Artificial dewatering of the sand clusters will result in higher slope stability values and a better ultimate pit.

4.5 Minimum required Clay Slope Formation Thickness preventing Fracture Initiation

Equation series 20 until 23 are determined based on the following statements. The confining stress exists out of a horizontal and vertical component. The Cohesion of the soil has been taken as the horizontal component because the resistance against movement at a normal pressure of zero equals the cohesion value according to the Mohr diagram. The vertical component is calculated by using the shear resistance and slope ratio parameters. Figure 62 visualises the assumed fracture propagation initiated from the mechanically weak sandstone inter-bedding through the mechanically stronger clay formation under slope conditions.

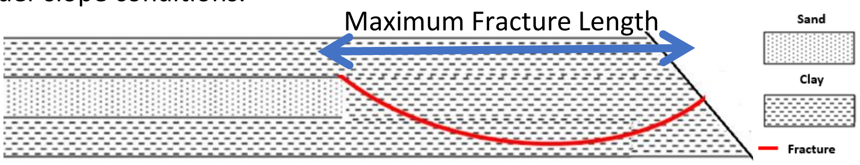

Figure 62: A Schematic Close-Up of an Inter-Bedded Slope Lithology with Fracture initiation

Verification of Equation series 20 till 23 as shown in Figure 63 (I & II) can be found by another author, (Decker & Clemence, 1981). The measured tensile strength of Figure 63 (I) was found to be in close agreement with the predicted values of the Mohr-Coulomb analysis in Figure 63 (II).

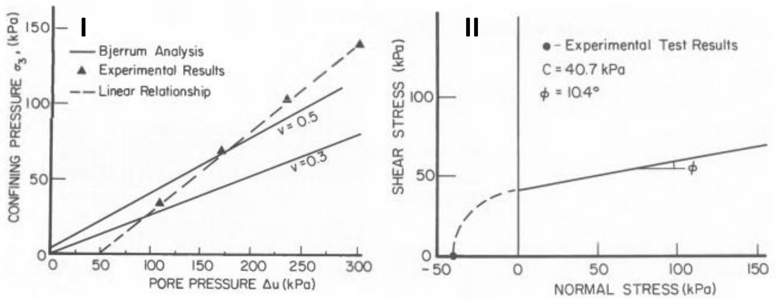

Figure 63: The Comparison of Average Experimental Test Results and Values Predicted by Theory (I) and Mohr-Coulomb Failure Envelope for the tested compacted Soil (II). The Tensile Strength of the Soil (Confining Pressure σ_3) has been determined by a Series of Hydraulic Fracture Tests, (Decker & Clemence, 1981).

Figure 64 visualises the sensitivity analysis on the maximum fracture length by changing the cohesion and friction angle respectively. The change in cohesion values shifts the linear relation right or left in the same magnitude as the change in cohesion value. The angle of the linear trendline towards the horizontal axes equals the friction angle. An increase in cohesion, slope ratio and normal stress results in a decrease of maximum fracture length. An increase in the hydrostatic head results in an increase of maximum fracture length. The constant parameters of Sibelco's Hohewieße quarry are taken as reference positions, with a confining yield stress of 19 kN/m^3, water column height of 20 metres, cohesion value of 25 and slope ratio of 1:3 (vertical : horizontal). A maximum fracture length of 9.0 metres is found. The sand inter-bedding is assumed to be in the economic loose clay ore.

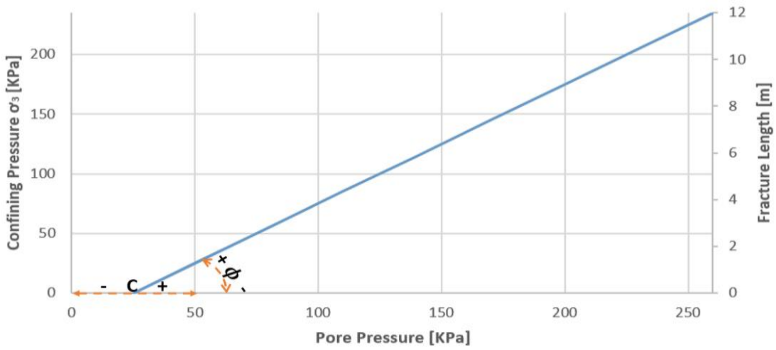

Figure 64: Sensitivity Analysis on the Maximum Fracture Length

4.6 Three Phases of Quarry Development based on the Factor of Safety

Quarry development will have three phases of mine design, namely an initial, work and final phase. During the initial phase, slope simulations will run until a stable factor of safety is reached. The shear parameters and lithologies are determined on borehole samples originating from the exploration stage. The non-active and active bench has a berm width of 4.5 and 24 metres respectively. An active overburden bench has a height of 7 metres and a slope angle of 60 degrees to the horizontal axis. An active clay bench has a height of 10 metres and a slope angle of 45 degrees to the horizontal axis. The slope angle of the active overburden and clay benches are updated until a stable factor of safety is reached.

Figure 65 shows the initial phase of the Stemmer Quarry. A slope angle of 60 and 45 degrees has been found for the overburden and clay benches respectively. The parameters of Table 13 are used as input parameters. The simulation based on Bishop's method resulted in a minimum factor of safety of 1.58. A clay refinery is located on basaltic bench 11. Table 2 suggests a minimum factor of safety of 1.5 since a high risk of economic and human losses are assumed due to the placement of the clay refinery.

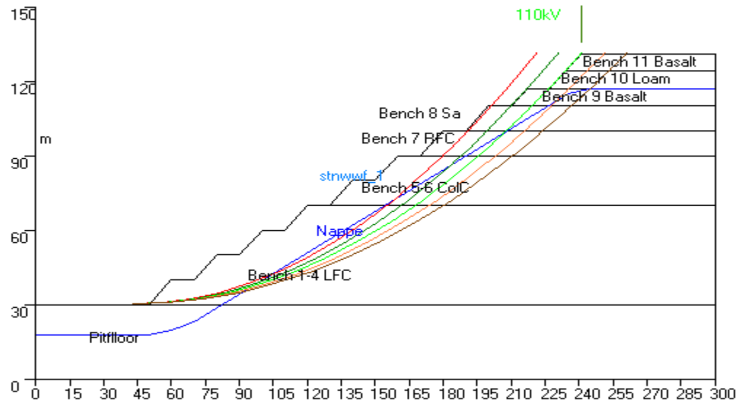

Figure 65: Initial phase of Sibelco's Stemmer Quarry

Table 13: The Lithology, Friction Angle, Cohesion and Sample Numbers of the simulated Stemmer Quarry. The Simulation Script can be found in Appendix B – Stemmer.

Bench	Lithology	Friction Angle [°]	Cohesion [kPa]	Specimen [Quarry#]	Remark
Pit Floor	-	25	0	-	Shear Parameters are assumed
1 until 4	Light Firing Clay	31	99	MA009	The formation does not reach the surface, sample MA009 has been collected just above the interface in a similar formation
5 and 6	Coloured Clay	23.7	143	MA004	-
7	Red Firing Clay	27.8	51	HO-014 Low Density	Red Firing Clay formation of the Hohewieße quarry is used as sample location.
8	Sand	25	0	-	Shear Parameters are assumed
9	Basalt	40	0	-	Shear Parameters are established by Arthe, (Arthe, 2017)
10	Loam	21	70	-	Shear Parameters are assumed
11	Basalt	40	0	-	Shear Parameters are established by Arthe, (Arthe, 2017)

During the work phase, the model is updated with geotechnical observations and calculations, namely: slope and surface cracks, hydrostatic head, sand inter-beddings and shear parameters. Sand inter-beddings can be observed by eye or cone penetration data. The hydrostatic head can be updated by boreholes and water seepage. Shear parameters can be updated by shearbox testing. New quarry dimension are measured by GPS locations.

Figure 66 visualises the initial and work phase of the Hohewieße quarry. The initial phase has been updated with the geotechnical observations of a high hydrostatic head, sand inter-bedding and slope and surface fractures. The simulation of the initial phase resulted in a factor of safety of around 1.35, which is stable by assuming moderate human and economic losses. The work phase simulation resulted in a factor of safety of around 1, which is unstable by assuming moderate human and economic losses. The factor of safety during the work phase can be increased by active or non-active[14] water dissipation or by the placement of embankments. During active water dissipation, the slope does not need the addition of an embankment to stabilise the quarry. During non-active water dissipation, the usage of an embankment is advisable depending on the acquired factor of safety.

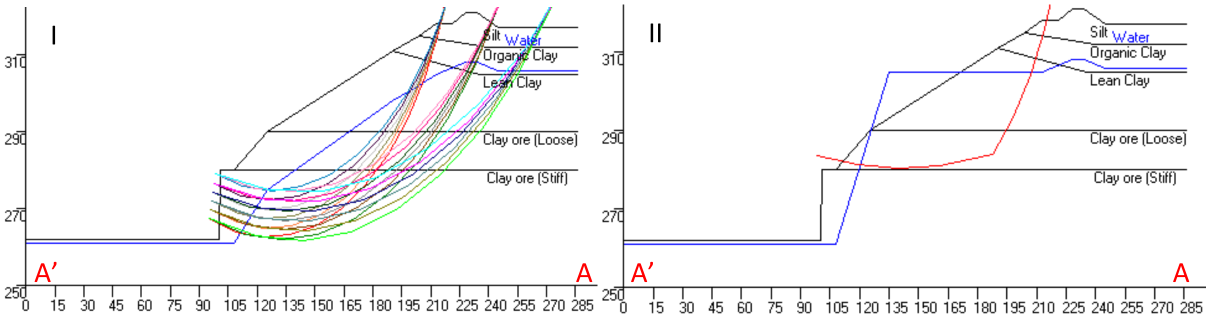

Figure 66: The Initial Phase (I) and Work Phase (II) of the Hohewieße Quarry. The Shear Parameters for Simulation can be found in Table 9. This Simulation is based on the Schematic Cross-Section A'-A as visualised in Figure 26.

Shearbox data of HO014 shows that compaction of the Hohewieße overburden is high enough in terms of strength to act as an embankment for slope stability increase. Embankments within the Westerwald clay pits are made from clay or basaltic overburden. The economic basaltic overburden shall be used if the clay slope shows water dissipation. The clay overburden is low in permeability. Therefore, dissipated water will not be able to leave the system and accumulate at the interface of the embankment and fresh clay slope. A new pressure difference will be created, decreasing shear parameters of the clay embankment.

Figure 67 visualises a gravel embankment placed for a stable quarry environment with non-active water dissipation. The visualised simulation holds a factor of safety of 1.4. This factor of safety is considered stable with moderate economic and human losses. The factor of safety will be increased in time by non-active water dissipation into the gravel embankment. The process of water dissipation lowers the hydraulic head in the sand layer.

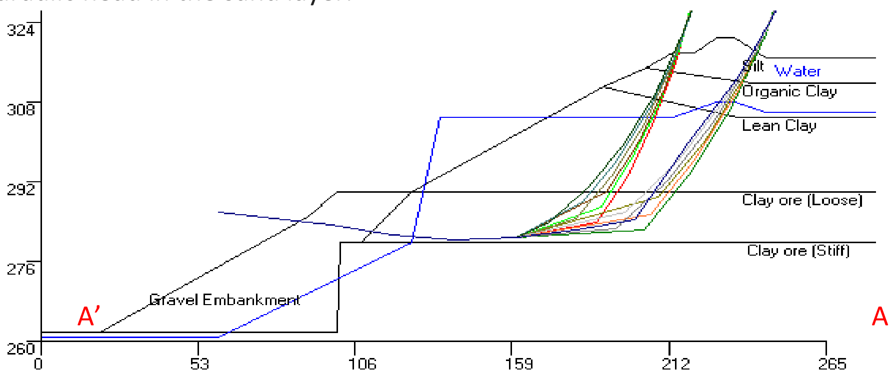

Figure 67: Placement of Embankment to increase the Stability. The Shear Parameters for Simulation can be found in Table 9. The Gravel Embankment holds a Friction Angle of 40 Degrees and a Cohesion Value of 0. This Simulation is based on the Schematic Cross-Section A'-A as visualised in Figure 26.

The final phase can be entered by using the clay overburden as backfill material. The clay overburden shall be compacted on top of the basaltic backfill. Dewatering of permeable basaltic

[14] Dissipation of water through initiated slope cracks is a slow process.

backfill is advisable as long the surface is not equalised to the level of the surrounding area. A schematic overview of the embankment placement for the final phase of the Hohewieße can be found in Figure 68, (Arthe, 2017). Good compaction of the clay backfill will increase the stability and the economic value of the area.

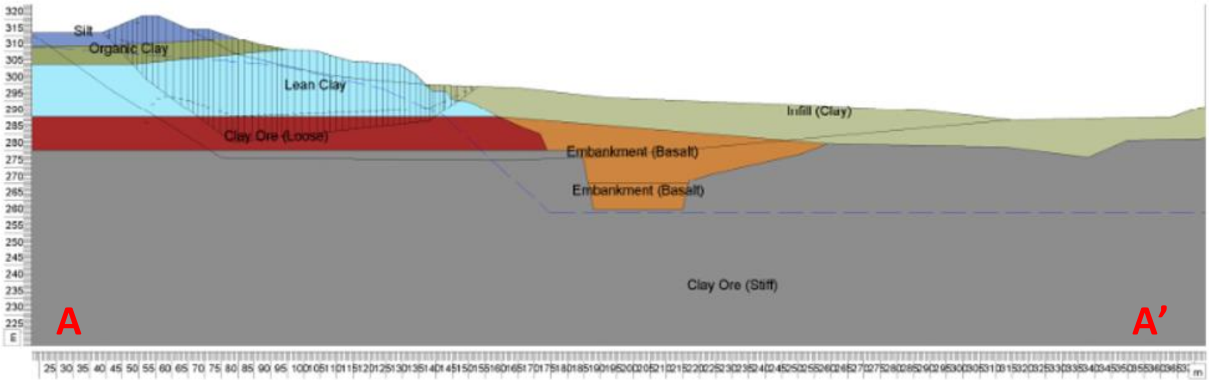

Figure 68: Embankment Placement, (Arthe, 2017). This Lithology is based on the Schematic Cross-Section A-A' as visualised in Figure 26.

Good compaction is fulfilled on soils with correct wetness and layer thickness. Assuming a layer thickness of 25 centimetres, the Sibelco owned CAT Dozer D6 should have a number of 6 passes to compact the cohesive fill correctly. A maximum thickness of 50 centimetres is allowed for correct compaction, (Nowak & Gilbert, 2015). The moisture content of the backfill must be within the range of -2 to +4 % of the optimum moisture content, (Rowe & Badv, 1996). This optimum moisture can be established on the clay's plastic limit, the correlation is visualised in Figure 69.

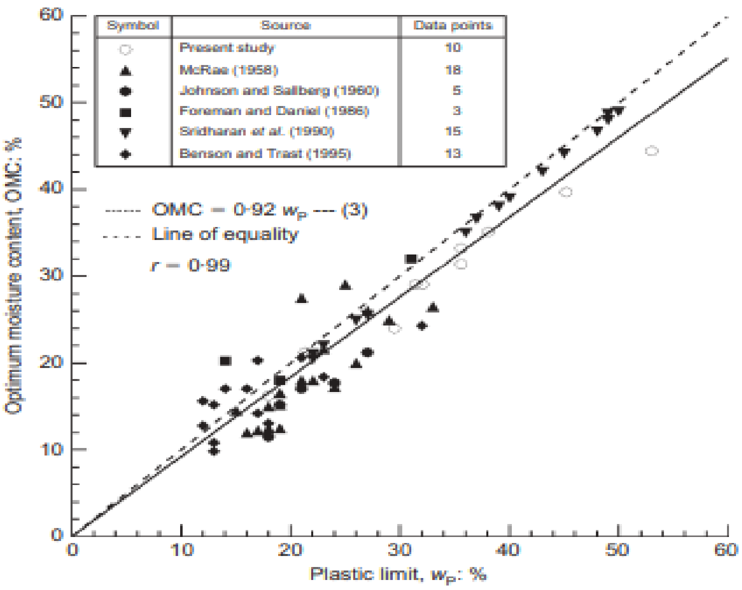

Figure 69: Compaction Characteristics expresses in Plastic Limit versus Optimum Moisture Content, (Sridharan & Nagaraj, 2013).

5 Conclusion

This study examines the degree of continuation of the fractures in an artificial heterogeneous layered system depending on mechanical properties of the layers respectively, influencing the fracture growth. The study generates a better understanding of fracture propagation of inter-bedded systems for the mining and petroleum sector.

The slope stability of Westerwald Clay Quarries is influenced by inter-bedding of thin sand layers. Surface and slope fractures within the clay formation originated from a high observed hydrostatic head within the sand layers and a reduced confining stress from mining activities. The ultimate mine planning can be improved by taking the effect of high pore pressures and inter-bedding into account. This study examines the effect of fracture continuation from sand layers into the stiff Westerwald Clay Formation by natural hydraulic fracturing. This effect lowers the factor of safety drastically.

The results show that slope instability is caused by a high hydraulic head within the sand layer, possibly leading to fracture initiation and/or water infiltration into the clay formation weakening the clay's strength. Fracture initiation is a combination of a decrease of confining pressure of the stiff clay by mining activities and a constant natural hydraulic pressure difference at the interface of the permeable sand and non-permeable clay formation. Slope stabilisation occurs by artificial water pumping or natural water dissipation through the possible formed cracks. At the presence of in-slope water dissipation, the slope stability is decreased by embankments of low permeable backfill and increased by high permeable backfill. The formation of slope cracks caused by natural hydraulic fracturing can be avoided by active water dissipation by pumping or by embankments of any type if there is no presence of in-slope water dissipation.

Inter-bedded systems are common target locations for an unconventional reservoir system. Improvement in recovery from these tight systems often depends on the extent and continuity of fractures through heterogeneous interfaces. This study examines the propagation and continuity of the fractures in an artificial heterogeneous layered system depending on the mechanical properties of the layers.

The results show that hydraulic fracture initiated in the weakest layer are arrested at the interface, whereas fractures initiated in mechanically stronger layers prograde through the interface with weaker formation. Hydraulic fractures are initiated by a pressure difference that exceeds the critical tensile stress. The confining pressure controls the critical tensile stress and therefore the required hydraulic pressure difference. Hydraulic fracturing within the mechanically stronger formation is advisable at inter-bedded systems. The fracture energy needs to be large enough to reach a desired fracture density in the mechanically stronger layer. A fracture will be created or enlarged in the mechanically weaker formation after interface penetration. Fracturing propagation through the interface from mechanically weak to strong is possible by hydraulic pressuring the weaker formation's global pore pressure, creating a pressure difference at the interface.

6 Recommendations

As a result of this work, five recommendations are suggested Paul J.S.A. van Oosterhout in order to improve the understanding of fracture propagation of inter-bedded systems for the mining and petroleum sector by hydraulic fluid injection. The recommended topics for further research are:

- Rate of fluid penetration from relative higher to lower permeability medium by constant fluid pressure and a decrease in axial pressure; This topic relates to the effect of natural in-situ water pressures in relation to mining activities.
- Literature research to natural pressuring of small sand clusters in a low permeable medium by compaction; This topic gives inside in origin of higher existing pressures in the higher permeable medium than the lower permeable surroundings.
- Field research to the degree of water infiltration into the low permeable clay surroundings in respect to the moisture content; This topic will give insight to degree of infiltration and natural or mining cause of infiltration if and only if the clay's permeability is determined.
- Shear parameters of the Westerwald clay material by changing moisture content; In relation with the degree of water infiltration in respect to moisture content, strength parameters of a possible failure slope can be determined in greater detail.
- Hydraulic fracturing experiments on the possibility of fracturing low-permeable specimen by slow pressurization of the high permeable medium; Normally hydraulic fractures are induced by a local pressure difference by high flow rate within one lithology. In this case, the fractures are established on the interface by slowly pressurizing the entire permeable specimen. A hydraulic fluid pressure difference will be created at interface rather than in one lithology.

7 References

Abramson, L., Lee, T., Sharma, S. & Boyce, G., 2002. Slope Stability Analysis Methods. In: *Slope Stability and Stabilization Methods.* New York: John Wiley and Sons, pp. 15-36.

American Society for Testing and Materials, 1996. *Standard Test Method for One-Dimensional Consolidation Properties of Soils,* West Conshohocken: ASTM Standards.

Anon., 2000. *Standard Test Methods for Liquid Limit, Plastic Limit and Plasticity Index of Soils,* West Conshohocken: ASTM .

Arthe, 2017. *The Hohewieße Quarry,* Houten: Arthe.

ASM International, 2004. *Introduction to Tensile Testing,* Materials Park: ASM International.

ASTM International, 1995. *Standard Test Method for Unconfined Compressive Strength of Intact Rock Core Specimens,* West Conshohocken: ASTM International.

ASTM International, 1998. *Standard Test Method for Particle-Size Analysis of Soils,* West Conshohocken: ASTM.

ASTM International, 2000. *Standard Test Methods for Liquid Limit, Plastic Limit and Plasticity Index of Soils,* West Conshohocken: ASTM International.

ASTM International, 2009. *C1605 Standard Test Methods for Chemical Analysis of Ceramic Whiteware Materials using Wavelength Disperce X-Ray Fluorescence Spectrometry,* West Conshohocken: ASTM International.

ASTM International, 2014. *D2166 Standard Test Method for Unconfined Compressive Strength of Cohesive Soil,* West Conshohocken: ASTM International.

ASTM International, 2014. *D3080 Direct Shear Test of Soils Under Consolidated Drained Conditions,* West Conshohocken: ASTM International.

ASTM International, 2014. *Standard Test Method for Direct Shear Test of Soils Under Consolidated Drained Conditions,* West Conshohocken: ASTM International.

ASTM International, 2014. *Standard Test Methods for Laboratory Determination of Water (Moisture) Content of Soil and Rock by Mass,* West Conshohocken: ASTM International.

Bardet, J. P., 1997. *Experimental Soil Mechanics.* Upper Saddle River: Prentice Hall.

Bertoti, G., 2018. *AES1840 Advanced Structural Geology [Powerpoint slides].* [Online].

Brocks, W. & Steglich, D., 2006. *Engineering Mechanics,* Geesthacht: Institute for Materials Research.

Byron Bird, R., E. Stewart, W., N. Lightfoot, E. & J. Klingenberg, D., 2013. *Introduction Transport Phenomena.* Wisconsin: Wiley.

Chuprakov, D., Melchaeva, O. & Prioul, R., 2013. Hydraulic Fracturing Propagation Across a Weak Discontinuity Controlled by Fluid Injection. *Effective and Systainable Hydraulic Fracturing,* pp. 157-181.

Controls Group, 2019. *Liquid Limit Penetrometers.* [Online]
Available at: https://www.controls-group.com/eng/soil-testing-equipment/liquid-limit-penetrometers_.php

Crain, R., 2015. *Elastic Constants and Mechanical Properties.* [Online]
Available at: https://www.spec2000.net/10-elastic.htm

Decker, R. & Clemence, S., 1981. *Laboratory Study of Hydraulic Fracturing in Clay,* London: ISSMGE.

Dong, Y. et al., 2011. Investigation of Soil Shear-Strength Parameters and Predictions of the Collapse of Gully Walls in the Black Soil Region of Northeastern China. *Physical Geography,* pp. 161-178.

Eijkelkamp, 2019. *Augering & Soil Sampling Equipment.* [Online]
Available at: https://en.eijkelkamp.com/products/augering-soil-sampling-equipment/sample-ring-kit-model-e.html

Ellen Macarthur Foundation, 2013. *Towards the Circular Economy,* Sail Loft: Ellen Macarthur Foundation.

Frederick University, 2017. *What Effect does Pore Water in Soil have on Shear Strength.* [Online]
Available at:
http://staff.fit.ac.cy/eng.ls/lectures/ACEG220/ACEG220%20Lecture%203%20Pore%20water%20and%20soil%20strength.pdf

Frohlich, O. K., 1953. The Factor of Safety with Resprect to Sliding of a Mass of Soil Along the Arc of a Logarithmic Spiral. *Proceedings of the Third International Conference on Soil Mechanics and Foundation Engineering,* pp. 230-233.

G.U.B. Ingenieur AG, 2011. *OU Niederahr/Hahner kreuz Standsicherheitsuntersuchung Tongrube Pfeul,* Ransbach-Baumbach: Sibelco Deutschland GmbH.

GEO-SLOPE International, 2012. *Stability Modeling with SLOPE/W,* Alberta: GEO-SLOPE International Ltd..

Helgeson, D. E. & Aydin, A., 1991. Characteristics of Joint Propagation Across Layer Interfaces in Sedimentary Rocks. *Journal of Structural Geology,* pp. 897-911.

Hollanders, S., 2019. *Chemical XRF,* Dessel: Sibelco.

Kaixi, X., Ajmera, B., Tiwari, B. & Hu, Y., 2016. *Effect on Long Duration Rainstorm on Stability of Red Clay Slopes,* s.l.: Crossmark.

Kresse, O. et al., 2013. Effect of Flow Rate and Viscosity on Complex Fracture Development in UFM Model. *Effective and Systainable Hydraulic Fracturing,* pp. 20-22.

Kuntz, A., 1996. *Westerwald Potter's History.* [Online]
Available at: http://www.corzilius.org/Narratives/WesterwaldPottery_English.htm

Kurakose, B., Mathews Abraham, B., Sridharan, A. & T. Jose, B., 2017. *Water Content Ratio: An Effective Substitute fore Liquidity Index for Prediction of Shear Strength of Clayes,* Switzerland: Springer International Publshing.

Labuz, J. & Zang, A., 2012. Mohr-Coulomb Failure Criterion. *Rock Mechanics and Rock Engineering,* pp. 975-979.

Li, D., Yin, K., Glade, T. & Leo, C., 2017. *Effect of over-consolidation and Shear Rate on the Residual Strength of Soils of Silty Sand in the Three Gorges Reservoir,* s.l.: Springer Nature.

Lo, K. Y., 1961. *Stress-Strain Relationship and Pore Water Pressure Characteristics of a Normally-consolidated Clay,* Paris: 5th Internatinal Conference on Soil Mechanics and Foundations Engineering.

Munira, R. et al., 2015. The Effect of Interbedding on Shale Reservoir Properties. *Marine and Petroleum Geology,* Issue 67, pp. 154-169.

Nowak, P. & Gilbert, P., 2015. *Earthworks.* Londen: Institution of Civil Engineers.

Nowak, P. & Gilbert, P., 2015. *Earthworks.* Londen: Institution of Civil Engineers.

Oosterhout, P. v., 2017. *Geotechnical Testing Methodologies to aid in the Interpratation of in Situ Deformation Data,* Delft: Technical University Delft.

Quantachrome Corporation, 2019. *Gas Pycnometers,* Boynton Beach: Quantachrome Corporation.

Regelink, J. A., 2018. *Influence of Mechanical Contrast and Confining Pressure on Fracture Behaviour in Layered Rocks,* Delft: Delft University of Technology.

Rowe, K. R. & Badv, K., 1996. Use of a Geotextile Separator to Minimize Intrusion of Clay into a Coarse Stone Layer. *Geotextiles and Geomembranes,* pp. 73-93.

Roylance, D., 2008. *Mechanical Properties of Materials.* s.l.:s.n.

Sibelco Deutschland GmbH, 2013. *Geo Meeting Introduction,* Ransbach-Baumbach: Sibelco NV.

Simsolid, 2019. *Material Properties.* [Online]
Available at: https://www.simsolid.com/faq-items/material-properties/

Skels, P. & Bondars, K., 2015. *Testing of Landslide Triggering Mechanism by Pore Pressure Inflation with Back Pressure Shear Box,* Durham: Proceedings of the 24th European Young Geotechnical Engineers Conference.

Soltanzadeh, M., 2015. *A Primer on the Geomechanics behind Fracturing Pressure Curves,* Calgary: PetroGem Inc..

Sridharan, A. & Nagaraj, H., 2013. Plastic Limit and Compaction Characteristics of Fine Grained Soil. *Ground Improvement,* pp. 17-22.

Taheri-Shakib, J., Ghaderi, A. & Hashemi, A., 2015. Analysis of Interaction Between Hydraulic and Natrual Fractures. In: Intech, ed. *Fracture Mechanis - Properties, Patterns and Behaviours.* Bergharen: InTech, pp. 193-213.

Tanzen, R., Sultana, T., Islam, M. & Khan, A. J., 2016. *Determination of Plastic Limit using Cone Penetrometer,* Chittagong: Proceedings of 3rd International Conference on Advances in Civil Engineering.

Terzaghi, k., 1925. Principles of Soil Mechanics. *Engineering News-Record,* Volume 95, pp. 19-27.

Turcotte, D. L. et al., 2016. Fracking in Tight Shales: What is It, What does It accomplish, and What are its Consequences. *Annual Review of Earth and Planetary Sciences,* Issue 44, pp. 321-351.

University of Neuchâtel, 2008. *The Concise Encyclopedia of Statistics,* Neuchâtel: Springer.

Vásárhelyi, B. & Ván, P., 2006. Influence of Water Content on the Strength of Rock. *Engineering Geology,* pp. 70-74.

Volume Graphics, 2019. *myVGL.* [Online]
Available at: https://www.volumegraphics.com/en/products/myvgl.html

Xu, C. et al., 2015. Behaviour of Propagating Fracture at Bedding Interface in Layered Rocks. *Engineering Geology,* pp. 33-41.

Yuen, K., Graham, J. & Janzen, P., 1998. Weathering-Induced Fissuring and Hydraulic Conductivity in a Natural Plastic Clay. *NRC Canada,* pp. 1101-1108.

Zuyu, C., Hongliang, M., Faming, Z. & Xiaogang, W., 2011. A Simplified Method for 3D Slope Stability Analysis. *Canadian Geotechnical Journal,* pp. 675 - 683.

APPENDICES

A Sample Specification

A sample specification based on field density, moisture content, atterberg limits and shearbox data is given within this Appendix

A.1 Sample Locations Stemmer

A total of nine samples have been gathered ranging from basaltic rocks to topsoil. The sample location is visible in Figure 4 and is numbered A until E. Specific sample information has been given in Table 14 and Table 15. The basaltic and red baked clay specimen is not in the scoop of this research and are mentioned for sampling registration.

Table 14 visualises the taken samples and information regarding its location, description, field density and moisture content.

Table 14: Sample Specification of Stemmer

Material	Code [-]	Moisture [ratio]	Field Density [kg/m^3]	Location [Figure 4]	Description [Type, Colour, Friability, Other]
Top Soil	[GE-DE-MA-001]	0.27	$1.68 * 10^3$	A	Sandy clay, brown/black, non-sticky, small peddles within the soil
Clay	[GE-DE-MA-002]	0.19	$2.04 * 10^3$	A	Clay, brown/beige, very sticky, plastic,
Basalt	[GE-DE-MA-003]	-	-	A	Basalt, Black/grey, brittle, hard
Clay	[GE-DE-MA-004]	0.12	$2.20 * 10^3$	E	Clay, yellow/orange, stiff, brittle, feels very waxy
Clay (Baked)	[GE-DE-MA-005]	-	-	B	Baked Clay, red, brittle, hard
Basalt	[GE-DE-MA-006]	-	-	C	Basalt, Black/grey, brittle, hard, same material as [GE-DE-MA-003] but different location
Clay (Baked)	[GE-DE-MA-007]	0.17	-	D	Baked Clay, red, brittle, hard, same material as [GE-DE-MA-005] but different location
Clay	[GE-DE-MA-008]	0.04	$2.16 * 10^3$	D	Clay, white, stiff, brittle, breaks/powders easily during sampling
Clay	[GE-DE-MA-009]	0.12	$2.20 * 10^3$	D	Same sampling layer as [GE-DE-MA-004] but different location

Table 15 visualises performed tests on the specimen, namely atterberg limit, undisturbed shearbox and amount of undisturbed ring specimen of a diameter of 5.0 centimetres and a length of 6.2 centimetres.

Table 15: Performed tests on Specimen of the Stemmer Quarry

Material	Code [-]	Atterberg Limit [yes/no]	Ring Sampled [number]	Shearbox [yes/no]
Top Soil	[GE-DE-MA-001]	Yes	5	Yes
Clay	[GE-DE-MA-002]	Yes	5	Yes
Basalt	[GE-DE-MA-003]	No	0	No
Clay	[GE-DE-MA-004]	Yes	5	Yes
Clay (Baked)	[GE-DE-MA-005]	No	0	No
Basalt	[GE-DE-MA-006]	No	0	No
Clay (Baked)	[GE-DE-MA-007]	No	0	No
Clay	[GE-DE-MA-008]	Yes	0	No
Clay	[GE-DE-MA-009]	yes	5	Yes

A.2 Atterberg Limits

The Atterberg Limits of the clays used for simulation are shown as Liquid Limit, Plastic Limit and Plasticity index within Table 16.

Table 16: Atterberg Limits of the Relevant Clay Specimen

Material	Code [-]	Liquid Limit [Ratio]	Plastic Limit [Ratio]	Plasticity Index [-]
Top Soil	[GE-DE-MA-001]	-	0.23	-
Clay	[GE-DE-MA-002]	0.36	0.20	0.15
Clay	[GE-DE-MA-004]	0.44	0.31	0.12
Clay	[GE-DE-MA-008]	0.29	0.24	0.05
Clay	[GE-DE-MA-009]	0.49	0.35	0.15
Clay	[GE-DE-LI-014]	0.61	0.45	0.16
Clay	[GE-DE-LI-007]	0.41	0.34	0.07

Liquid Limit is determined as the moisture content at an impact of twenty millimetres as visualised in the Graphs below (Figure 70 till Figure 75).

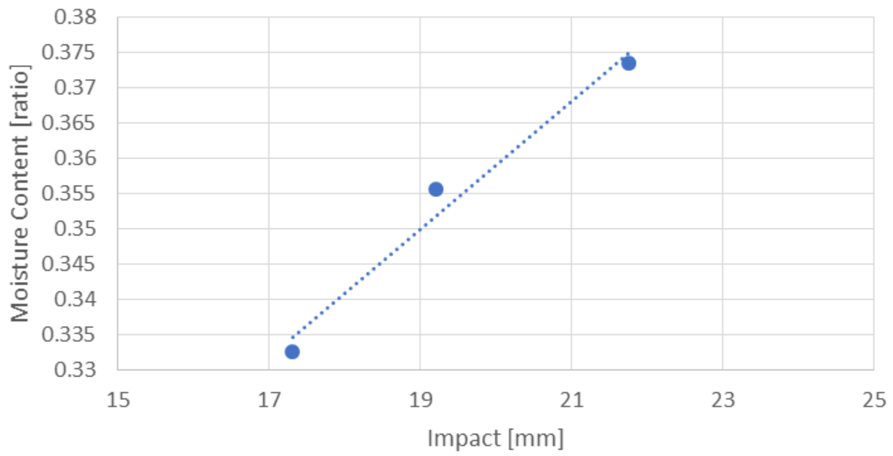

Figure 70: Liquid Limit [GE-DE-MA-002]

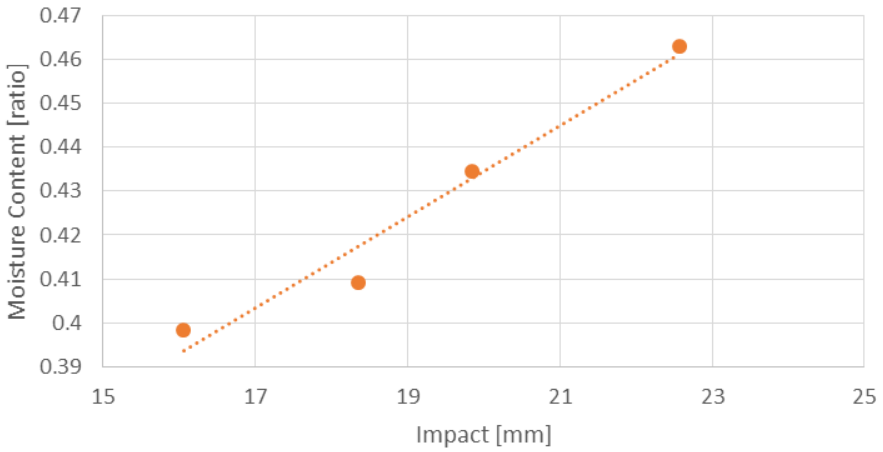

Figure 71: Liquid Limit [GE-DE-MA-004]

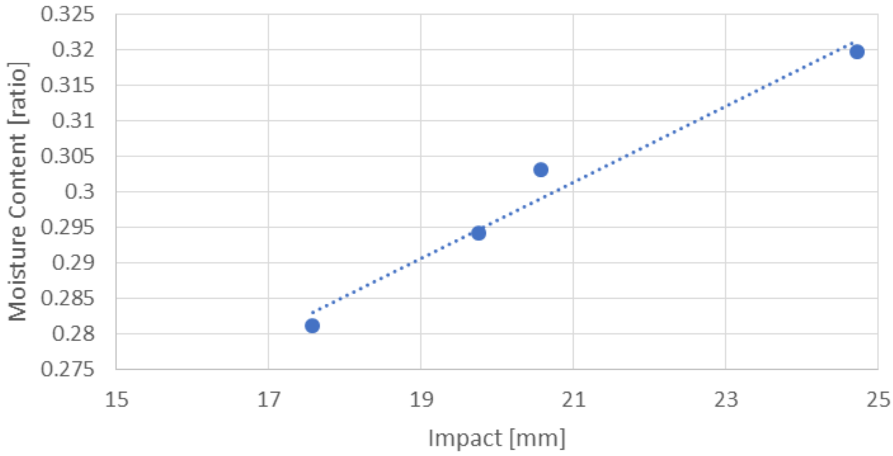

Figure 72: Liquid Limit [GE-DE-MA-008]

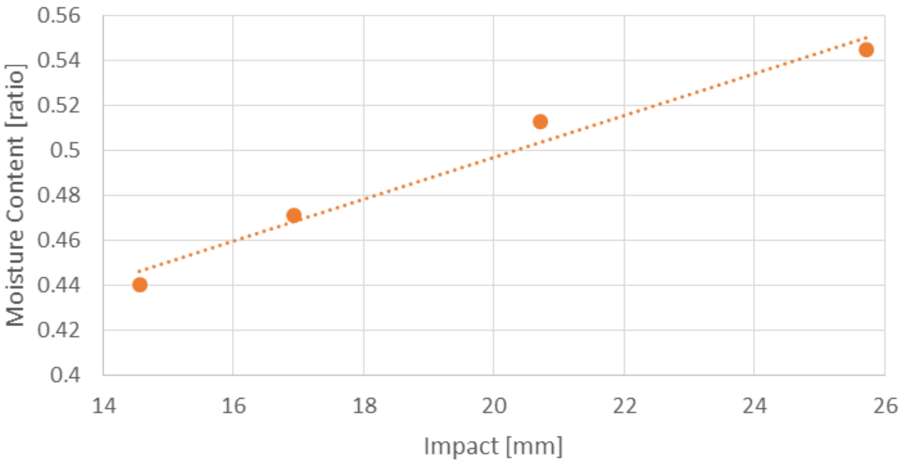

Figure 73: Liquid Limit [GE-DE-MA-009]

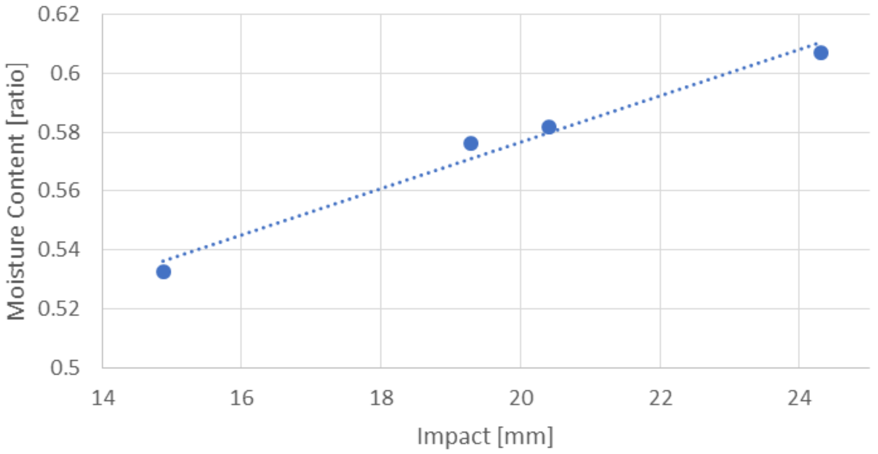

Figure 74: Liquid Limit [GE-DE-LI-014]

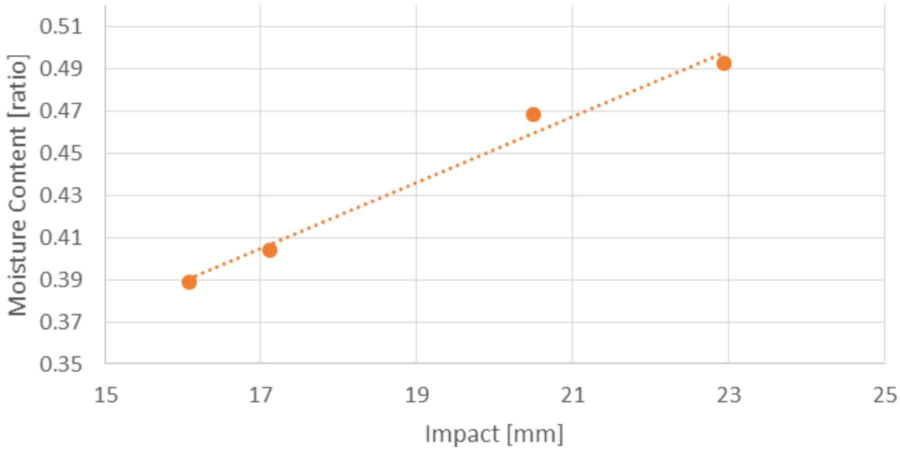

Figure 75: Liquid Limit [GE-DE-LI-007]

A.3 Individual Shearbox Graphs

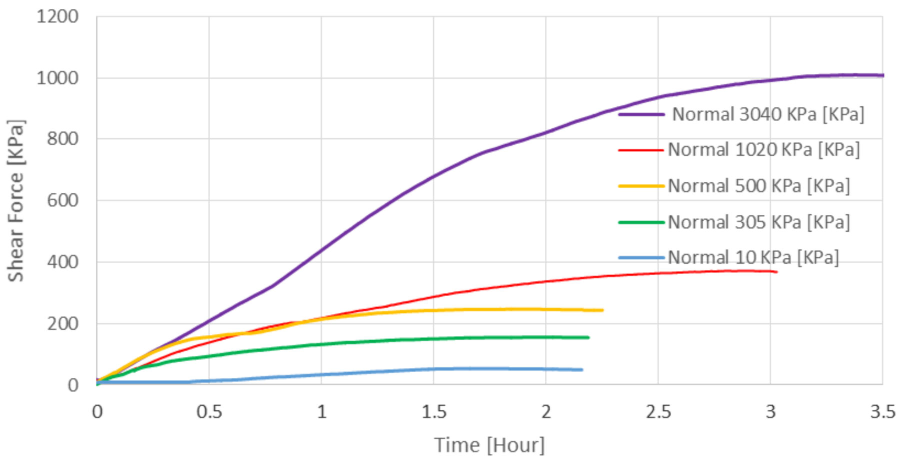

Figure 76: GE-DE-MA-001

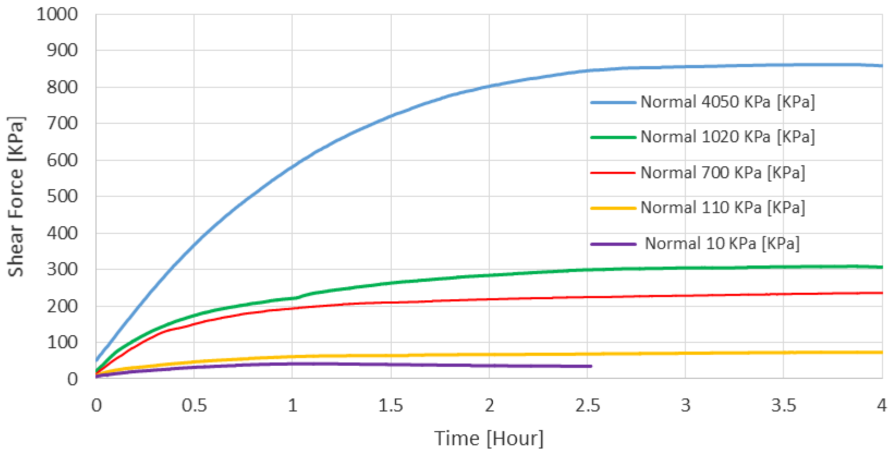

Figure 77: GE-DE-MA-002

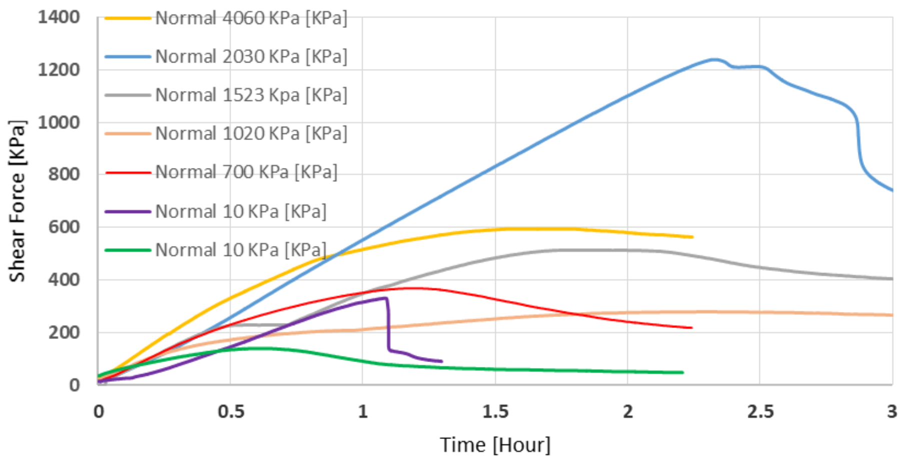

Figure 78: GE-DE-MA-004

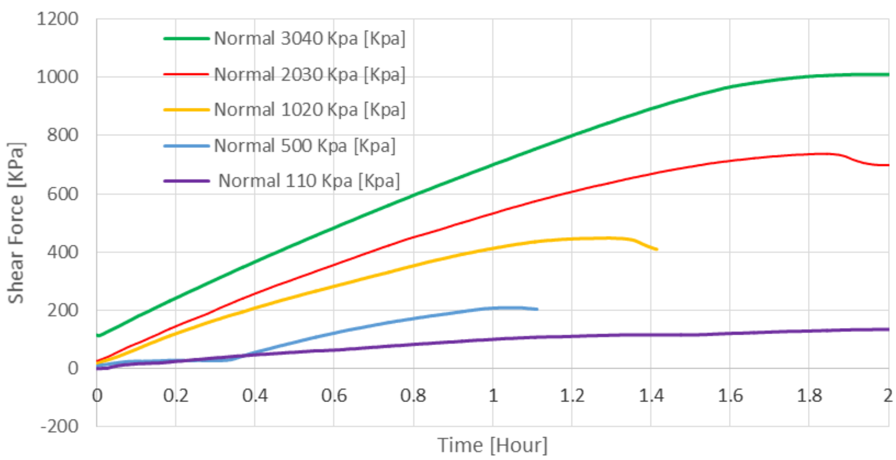

Figure 79: GE-DE-MA-009

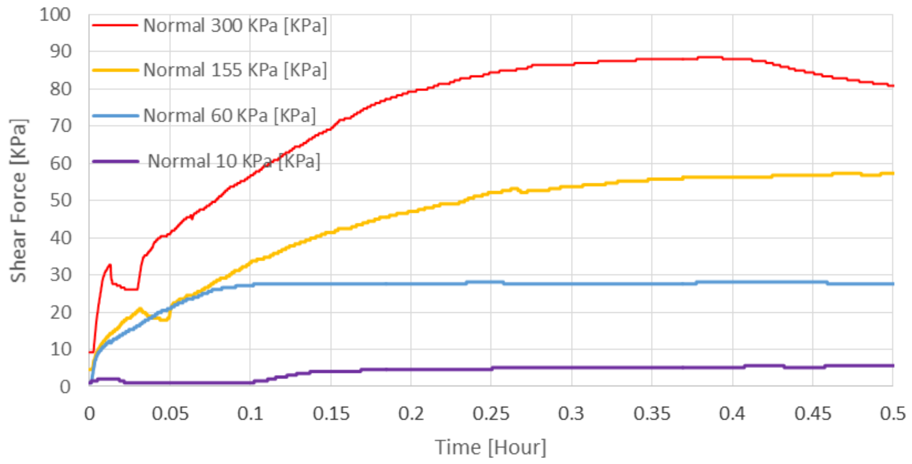

Figure 80GE-DE-LI-007, Carried-Out without Underwater Conditions at Low Normal Load

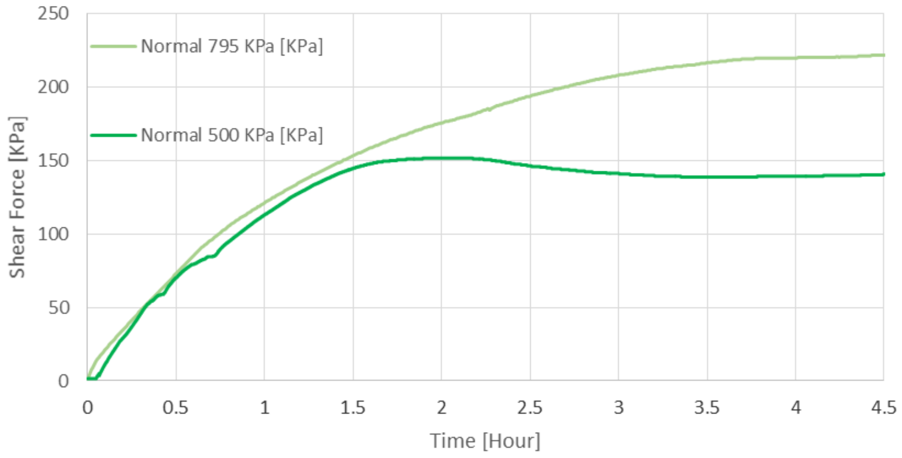

Figure 81: GE-DE-LI-007, Carried-Out without Underwater Conditions at High Normal Load

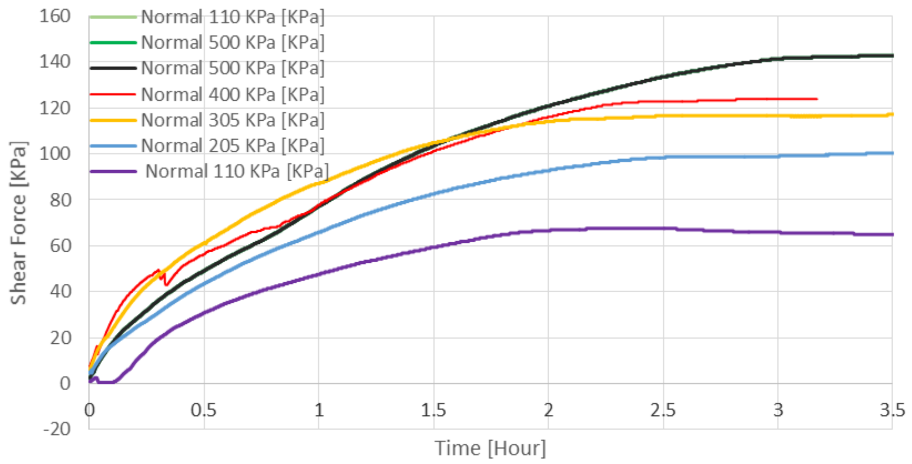

Figure 82: GE-DE-LI-007, Carried-Out with Underwater Conditions at High Load

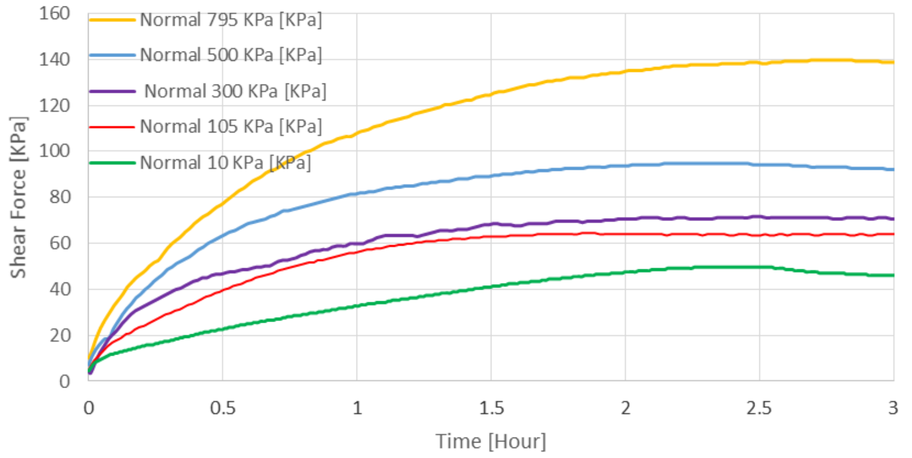

Figure 83: GE-DE-LI-008

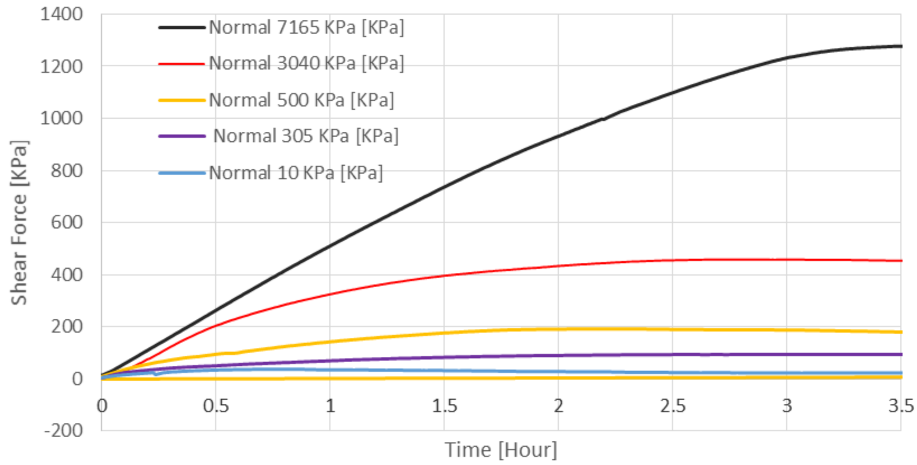

Figure 84: GE-DE-HO-014 with Field Density of 1.440 $* 10^3 \ kg/m^3$

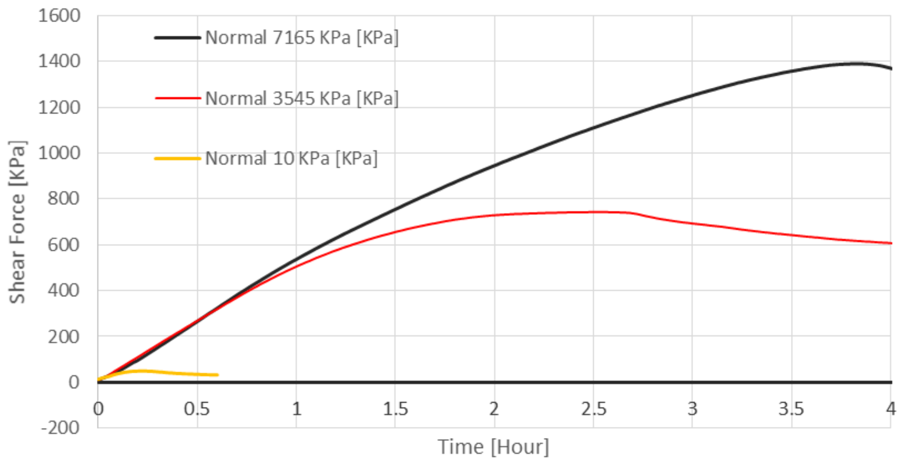

Figure 85: GE-DE-HO-014 with Field Density of 1.660 $* 10^3 \ kg/m^3$

A.4 Sample Configuration and Dimensional Measurements

Table 17: Sample Configuration. HFB; High Porosity Fontaine Bleau, AIN; Ainsa Sandstone, LFB; Low Porosity Fontaine Bleau and BEN; Bentheimer Sandstone

Sample	Layer 1	Layer 2	Layer 3
1	HFB1	AIN1	HFB2
2	AIN2	LFB2	AIN3
3	HFB4	BEN6	HFB5
4	LFB4	HFB3	LFB5
5	LFB6	BEN7	LFB9
6	AIN7	BEN5	AIN8
7	HFB7	LFB3	HFB8
9	AIN5	LFB1	AIN6
11	LFB7	AIN9	LFB8
12	HFB9	AIN10	HFB10
14	HFB11	BEN2	HFB12
15	BEN11	AIN11	BEN12
16	AIN12	LFB15	AIN13
17	LFB11	HFB14	LFB12
19	LFB13	BEN15	LFB14
20	AIN14	BEN16	AIN15

Table 18: Sample Dimensional Measurements. HFB; High Porosity Fontaine Bleau, AIN; Ainsa Sandstone, LFB; Low Porosity Fontaine Bleau and BEN; Bentheimer Sandstone

Sample	Height (average) [mm]	Width (average) [mm]	Weight (average) [gram]	Porosity [%]
AIN1	20.12	29.6	36.92	1.64
AIN2	19.65	29.6	36.09	1.64
AIN4	19.62	29.6	35.70	2.88
AIN5	19.95	29.6	36.48	2.34
AIN6	20.32	29.6	37.11	2.46
AIN7	20.45	29.6	37.34	2.36
AIN8	19.55	29.6	35.81	2.23
AIN9	21.33	29.6	39.04	2.24
AIN10	20.57	29.6	37.35	3.09
AIN11	21.70	29.6	39.83	1.82
AIN12	19.90	29.55	36.32	2.34
AIN13	20.30	29.6	37.19	1.93
AIN14	19.77	29.6	36.26	1.56
AIN15	19.70	29.6	36.04	2.04
HFB1	21.53	21.53	35.63	9.60
HFB2	22.10	22.10	36.78	8.92
HFB3	22.65	22.65	37.21	10.12
HFB4	21.20	21.20	35.04	9.44
HFB5	21.75	21.75	36.30	8.69
HFB7	22.45	29.65	37.07	9.63
HFB8	19.80	29.65	32.51	10.19
HFB9	21.72	29.65	36.13	8.84
HFB10	22.20	29.65	36.62	9.46
HFB11	21.95	29.65	36.50	8.86
HFB12	21.90	29.65	36.54	8.68
HFB14	21.85	29.65	36.05	9.64
LFB1	21.55	29.7	37.58	4.79
LFB2	21.35	29.7	37.23	4.73
LFB3	22.90	29.7	40.21	3.91

LFB4	21.25	29.7	37.00	4.80
LFB5	20.90	29.7	35.98	5.70
LFB6	23.40	29.7	40.95	4.32
LFB7	21.45	29.7	37.34	4.83
LFB8	21.90	29.7	37.61	6.27
LFB9	21.13	29.7	36.35	6.17
LFB11	20.85	29.7	29.7	5.73
LFB12	22.28	29.7	29.7	4.69
LFB13	22.40	29.7	29.7	4.21
LFB14	21.10	29.7	29.7	4.68
LFB15	21.13	29.7	29.7	6.38
BEN2	20.25	29.55	27.89	24.73
BEN5	23.55	29.55	32.52	24.56
BEN6	20.05	29.60	27.74	24.71
BEN7	19.70	29.55	27.17	24.86
BEN11	20.10	29.55	27.68	25.20
BEN12	20.20	29.60	27.94	25.56
BEN15	23.15	29.55	31.80	25.39
BEN16	21.00	29.58	29.06	25.0

B Scripts for Slope Stability Simulation Programme Stabilité

Different codes will be given within this Appendix in order to reproduce the slope stability analysis within Stabilité, a programme by the University of Liege.

Simulation 1:

```
[DONNEE]
Version=Talus WinVersion2010
Titre = hohewiese
nb_couche =5
nb_glissement =18
nappe = oui
nb_survert =0
nb_surhori = 0
acc_sismVert = 0
acc_sismHori = 0
prec_iter = .01
num_couche_surpression = 5
Multi color glissement=1
Decalage profil=0.0
Decalage profilY=0.000
[C-COUCHE 1 : COUCHE 1]
0.2 27 1.9 1.9 0 0 1
0 262
100 262
101 280
287 280
0 0
# 235 280 Clay ore (Stiff)
[C-COUCHE 2 : COUCHE 2]
2.5 17.5 1.9 1.9 0 0 1
101 280
108 280
125 290
287 290
0 0
# 235 290 Clay ore (Loose)
[C-COUCHE 3 : COUCHE 3]
0.5 22.5 1.9 1.9 0 0 1
125 290
190 311
235 305
287 305
0 0
# 235 305 Lean Clay
[C-COUCHE 4 : COUCHE 4]
0 15 1.9 1.9 0 0 1
190 311
204 315
240 312
287 312
0 0
# 235 312 Organic Clay
[C-COUCHE 5 : COUCHE 5]
9 19 1.9 1.9 0 0 1
204 315
213 318
221 318
228 321
234 321
245 317
287 317
0 0
# 235 317 Silt
[SXX-surV]
1 5 43.9 20 20 40 40 1
[SXX-surV]
2 43.9 140.9 20 0 40 60 1
[N-nappe]
0 261
100 261
108 261
125 275
190 298
204 302
213 305
228 308
234 308
245 306
287 306
0 0
# 245 316 Water
[GL-C 0--> Cx:125.845 Cy:362.661
R:100.05]
95.29 267.39
108.85 264.07
122.73 262.66
136.68 263.20
150.42 265.68
163.68 270.04
176.20 276.21
187.74 284.05
198.08 293.43
207.01 304.16
214.36 316.03
219.99 328.80
0 0
# 0 0 GLx
[GL-C 1--> Cx:132.68 Cy:396.563
R:134.474]
95.29 267.39
113.63 263.44
132.34 262.09
151.06 263.35
169.42 267.20
187.07 273.58
203.65 282.34
218.86 293.33
232.39 306.33
243.98 321.09
253.40 337.31
0 0
# 0 0 GLx
[GL-C 2--> Cx:139.515 Cy:437.501
R:175.765]
95.29 267.39
119.39 262.89
143.89 261.79
168.30 264.11
192.15 269.80
214.98 278.76
236.34 290.81
255.81 305.71
273.02 323.18
0 0
# 0 0 GLx
[GL-C 3--> Cx:126.247 Cy:366.162
R:101.141]
95.83 269.71
109.55 266.41
123.59 265.06
137.69 265.67
151.56 268.24
164.94 272.72
177.57 279.01
189.20 287.00
199.61 296.54
208.58 307.42
215.96 319.45
221.58 332.39
0 0
# 0 0 GLx
[GL-C 4--> Cx:133.082 Cy:401.425
R:136.888]
95.83 269.71
114.52 265.80
133.58 264.54
152.62 265.94
171.29 269.98
189.21 276.57
206.04 285.60
221.45 296.88
235.14 310.20
246.84 325.29
0 0
# 0 0 GLx
[GL-C 5--> Cx:139.918 Cy:444.045
R:179.829]
95.83 269.71
120.52 265.27
145.59 264.31
170.55 266.84
194.91 272.83
218.20 282.15
239.97 294.62
259.80 310.00
277.28 327.99
0 0
# 0 0 GLx
[GL-C 6--> Cx:126.649 Cy:369.881
R:102.441]
96.36 272.02
110.28 268.76
124.51 267.46
138.78 268.16
152.82 270.84
166.35 275.45
179.11 281.89
190.84 290.05
201.33 299.76
```

210.36 310.83
217.76 323.06
0 0
0 0 GLx
[GL-C 7--> Cx:133.485 Cy:406.631 R:139.637]
96.36 272.02
115.46 268.16
134.90 267.00
154.32 268.56
173.34 272.80
191.57 279.65
208.68 288.97
224.32 300.58
238.20 314.25
250.04 329.73
0 0
0 0 GLx
[GL-C 8--> Cx:140.32 Cy:451.088 R:184.385]
96.36 272.02
121.71 267.64
147.42 266.84
172.99 269.62
197.93 275.94
221.75 285.66
243.98 298.60
264.19 314.51
281.99 333.08
0 0
0 0 GLx
[GL-C 9--> Cx:127.052 Cy:373.848 R:103.982]
96.90 274.33
111.04 271.11
125.50 269.88
139.98 270.67
154.21 273.48
167.92 278.23
180.83 284.85
192.69 293.20
203.28 303.12
212.38 314.42
219.82 326.87
0 0
0 0 GLx
[GL-C 10--> Cx:133.887 Cy:412.23 R:142.771]
96.90 274.33
116.45 270.53
136.34 269.48
156.18 271.21
175.59 275.69
194.19 282.82
211.61 292.47
227.52 304.45
241.61 318.53
253.60 334.44
0 0
0 0 GLx
[GL-C 11--> Cx:140.722 Cy:458.703 R:189.506]
96.90 274.33
122.98 270.03
149.41 269.40
175.68 272.45
201.26 279.13
225.66 289.30
248.41 302.77
269.06 319.27
287.22 338.49
0 0
0 0 GLx
[GL-C 12--> Cx:127.454 Cy:378.102 R:105.802]
97.43 276.65
111.84 273.46
126.56 272.30
141.29 273.21
155.76 276.16
169.67 281.09
182.76 287.91
194.78 296.48
205.48 306.64
214.67 318.20
222.15 330.92
0 0
0 0 GLx
[GL-C 13--> Cx:134.289 Cy:418.282 R:146.35]
97.43 276.65
117.50 272.90
137.90 271.98
158.23 273.90
178.09 278.64
197.10 286.09
214.88 296.12
231.10 308.53
245.43 323.07
0 0
0 0 GLx
[GL-C 14--> Cx:141.124 Cy:466.977 R:195.279]
97.43 276.65
124.35 272.42
151.59 271.98
178.62 275.33
204.93 282.42
230.00 293.09
253.33 307.15
274.48 324.32
0 0
0 0 GLx
[GL-C 15--> Cx:127.856 Cy:382.687 R:107.944]
97.97 278.96
112.70 275.81
127.72 274.74
142.74 275.77
157.48 278.89
171.63 284.02
184.94 291.07
197.13 299.91
207.98 310.36
217.27 322.21
224.81 335.24
0 0
0 0 GLx
[GL-C 16--> Cx:134.691 Cy:424.858 R:150.446]
97.97 278.96
118.63 275.27
139.61 274.49
160.48 276.64
180.86 281.67
200.34 289.49
218.54 299.95
235.11 312.83
249.72 327.90
0 0
0 0 GLx
[GL-C 17--> Cx:141.526 Cy:476.017 R:201.81]
97.97 278.96
125.82 274.82
153.97 274.59
181.88 278.28
209.01 285.82
234.82 297.07
258.82 311.79
280.53 329.72
0 0
0 0 GLx

Simulation 2

```
[DONNEE]
Version=Talus WinVersion2010
Titre = hohewiese
nb_couche =5
nb_glissement =12
nappe = oui
nb_survert =0
nb_surhori = 0
acc_sismVert = 0
acc_sismHori = 0
prec_iter = .01
num_couche_surpression = 5
Multi color glissement=1
Decalage profil=0.0
Decalage profilY=0.000
[C-COUCHE 1 : COUCHE 1]
0.2 27 1.9 1.9 0 0 1
0 262
100 262
101 280
287 280
0 0
# 235 280 Clay ore (Stiff)
[C-COUCHE 2 : COUCHE 2]
2.5 17.5 1.9 1.9 0 0 1
101 280
108 280
125 290
287 290
0 0
# 235 290 Clay ore (Loose)
[C-COUCHE 3 : COUCHE 3]
0.5 22.5 1.9 1.9 0 0 1
125 290
190 311
235 305
287 305
0 0
# 235 305 Lean Clay
[C-COUCHE 4 : COUCHE 4]
0 15 1.9 1.9 0 0 1
190 311
204 315
240 312
287 312
0 0
# 235 312 Organic Clay
[C-COUCHE 5 : COUCHE 5]
9 19 1.9 1.9 0 0 1
204 315
213 318
221 318
228 321
234 321
245 317
287 317
0 0
# 235 317 Silt
[SXX-surV]
1 5 43.9 20 20 40 40 1
[SXX-surV]
2 43.9 140.9 20 0 40 60 1
[N-nappe]
0 261
100 261
108 261
135 305
190 305
204 305
213 305
228 308
234 308
245 306
287 306
0 0
# 245 316 Water

[GL-C 0--> Cx:125.845 Cy:362.661
R:100.05]
97.97 283.49
118.63 281.49
139.61 280.49
160.48 281
187.74 284.05
198.08 293.43
207.01 304.16
214.36 316.03
219.99 328.80
0 0
# 0 0 GLx
[GL-C 1--> Cx:132.68 Cy:396.563
R:134.474]
97.97 283.49
118.63 281.49
139.61 280.49
160.48 281
203.65 282.34
218.86 293.33
232.39 306.33
243.98 321.09
253.40 337.31
0 0
# 0 0 GLx
[GL-C 3--> Cx:126.247 Cy:366.162
R:101.141]
97.97 283.49
118.63 281.49
139.61 280.49
160.48 281
189.20 287.00
199.61 296.54
208.58 307.42
215.96 319.45
221.58 332.39
0 0
# 0 0 GLx
[GL-C 4--> Cx:133.082 Cy:401.425
R:136.888]
97.97 283.49
118.63 281.49
139.61 280.49
160.48 281
206.04 285.60
221.45 296.88
235.14 310.20
246.84 325.29
0 0
# 0 0 GLx
[GL-C 6--> Cx:126.649 Cy:369.881
R:102.441]
97.97 283.49
118.63 281.49
139.61 280.49
160.48 281
190.84 290.05
201.33 299.76
210.36 310.83
217.76 323.06
0 0
# 0 0 GLx
[GL-C 7--> Cx:133.485 Cy:406.631
R:139.637]
97.97 283.49
118.63 281.49
139.61 280.49
160.48 281
208.68 288.97
224.32 300.58
238.20 314.25
250.04 329.73
0 0
# 0 0 GLx
[GL-C 9--> Cx:127.052 Cy:373.848
R:103.982]
97.97 283.49
118.63 281.49
139.61 280.49
160.48 281
180.83 284.85
192.69 293.20
203.28 303.12
212.38 314.42
219.82 326.87
0 0
# 0 0 GLx
[GL-C 10--> Cx:133.887 Cy:412.23
R:142.771]
97.97 283.49
118.63 281.49
139.61 280.49
160.48 281
194.19 282.82
211.61 292.47
227.52 304.45
241.61 318.53
253.60 334.44
0 0
# 0 0 GLx
[GL-C 12--> Cx:127.454 Cy:378.102
R:105.802]
97.97 283.49
118.63 281.49
139.61 280.49
160.48 281
182.76 287.91
194.78 296.48
205.48 306.64
214.67 318.20
222.15 330.92
0 0
# 0 0 GLx
[GL-C 13--> Cx:134.289 Cy:418.282
R:146.35]
97.97 283.49
118.63 281.49
139.61 280.49
160.48 281
197.10 286.09
214.88 296.12
231.10 308.53
245.43 323.07
0 0
# 0 0 GLx
[GL-C 15--> Cx:127.856 Cy:382.687
R:107.944]
97.97 283.49
118.63 281.49
139.61 280.49
```

160.48 281
171.63 284.02
184.94 291.07
197.13 299.91
207.98 310.36
217.27 322.21
224.81 335.24
0 0
0 0 GLx
[GL-C 16--> Cx:134.691 Cy:424.858
R:150.446]
97.97 283.49
118.63 281.49
139.61 280.49
160.48 281
180.86 282.49
200.34 284.49
218.54 299.95
235.11 312.83
249.72 327.90
0 0
0 0 GLx

Simulation 3:

```
[DONNEE]
Version=Talus WinVersion2010
Titre = hohewiese
nb_couche =5
nb_glissement =1
nappe = oui
nb_survert =0
nb_surhori = 0
acc_sismVert = 0
acc_sismHori = 0
prec_iter = .01
num_couche_surpression = 5
Multi color glissement=1
Decalage profil=0.0
Decalage profilY=0.000
[C-COUCHE 1 : COUCHE 1]
0.2 27 1.9 1.9 0 0 1
0 262
100 262
101 280
287 280
0 0
# 235 280 Clay ore (Stiff)

[C-COUCHE 2 : COUCHE 2]
2.5 17.5 1.9 1.9 0 0 1
101 280
108 280
125 290
287 290
0 0
# 235 290 Clay ore (Loose)
[C-COUCHE 3 : COUCHE 3]
0.5 22.5 1.9 1.9 0 0 1
125 290
190 311
235 305
287 305
0 0
# 235 305 Lean Clay
[C-COUCHE 4 : COUCHE 4]
0 15 1.9 1.9 0 0 1
190 311
204 315
240 312
287 312
0 0
# 235 312 Organic Clay
[C-COUCHE 5 : COUCHE 5]
9 19 1.9 1.9 0 0 1
204 315
213 318
221 318
228 321
234 321
245 317
287 317
0 0
# 235 317 Silt
[SXX-surV]
1 5 43.9 20 20 40 40 1
[SXX-surV]
2 43.9 140.9 20 0 40 60 1
[N-nappe]
0 261
100 261
108 261
135 305
190 305
204 305
213 305
228 308
234 308
245 306
287 306
0 0
# 245 316 Water
[GL-C 0--> Cx:125.845 Cy:362.661
R:100.05]
97.97 283.49
118.63 281.49
139.61 280.49
160.48 281
187.74 284.05
198.08 293.43
207.01 304.16
214.36 316.03
219.99 328.80
0 0
# 0 0 GLx
```

Stemmer:

```
[DONNEE]
Version=Talus WinVersion2010
Titre = stnwwf_1
nb_couche =8
nb_glissement =5
nappe = oui
nb_survert = 0
nb_surhori = 0
acc_sismVert = 0
acc_sismHori = 0
prec_iter = .01
num_couche_surpression = 8
Multi color glissement=1
Decalage profil=0.000
Decalage profilY=0.000
[C-COUCHE 1 : COUCHE 1]
0 25 1.6 1.6 0 0 1
0 30
300 30
300 0
0 0
# 20 20 Pitflloor
[C-COUCHE 2 : COUCHE 2]
9.9 31 1.9 1.9 0 0 1
50 30
60 40
70 40
80 50
90 50
100 60
110 60
120 70
300 70
300 30
0 0
# 90 45 Bench 1-4 LFC
[C-COUCHE 3 : COUCHE 3]
14.3 23.7 1.9 1.9 0 0 1
130 70
140 80
150 80
160 90
300 90
300 70
0 0
# 140 80 Bench 5-6 ColC
[C-COUCHE 4 : COUCHE 4]
5.1 27.8 1.9 1.9 0 0 1
170 90
180 100
300 100
300 90
0 0
# 140 100 Bench 7 RFC
[C-COUCHE 5 : COUCHE 5]
0 25 1.6 1.6 0 0 1
190 100
200 110
300 110
300 100
0 0
# 150 110 Bench 8 Sa

[C-COUCHE 6 : COUCHE 6]
0 40 2.3 2.3 0 0 1
210 110
217 117
300 117
300 110
0 0
# 220 117 Bench 9 Basalt
[C-COUCHE 7 : COUCHE 7]
7 21 1.9 1.9 0 0 1
227 117
234 124
300 124
300 117
0 0
# 230 124 Bench 10 Loam
[C-COUCHE 8 : COUCHE 8]
0 40 2.3 2.3 0 0 1
234 124
241 131
300 131
300 124
0 0
# 240 131 Bench 11 Basalt
[OBJ- objet 1]
231.3 241.3 231 241 136 32567 0 0
# 210 150 110kV
[N-nappe]
0 18
50 18
55 19
60 20
65 21
70 23
235 115
240 116
245 117
300 117
0 0
# 120 63 Nappe
[GL-PARAB: 1--> X1:42.891 Y1:30.174
X2:221.728 Y2:131.876]
42.89    30.17
55.67    30.69
68.44    32.25
81.21    34.84
93.99    38.48
106.76   43.15
119.54   48.85
132.31   55.60
145.08   63.38
157.86   72.20
170.63   82.06
183.41   92.96
196.18   104.89
208.95   117.87
221.73   131.88
0 0
# 0 0 GLP 1
[GL-PARAB: 2--> X1:42.891 Y1:30.174
X2:231.728 Y2:131.876]
42.89    30.17
56.38    30.69
69.87    32.25
83.36    34.84
96.84    38.48
110.33   43.15
123.82   48.85
137.31   55.60
150.80   63.38
164.29   72.20
177.77   82.06
191.26   92.96
204.75   104.89
218.24   117.87
231.73   131.88
0 0
# 0 0 GLP 2
[GL-PARAB: 3--> X1:42.891 Y1:30.174
X2:241.728 Y2:131.876]
42.89    30.17
57.09    30.69
71.30    32.25
85.50    34.84
99.70    38.48
113.90   43.15
128.11   48.85
142.31   55.60
156.51   63.38
170.71   72.20
184.92   82.06
199.12   92.96
213.32   104.89
227.53   117.87
241.73   131.88
0 0
# 0 0 GLP 3
[GL-PARAB: 4--> X1:42.891 Y1:30.174
X2:251.728 Y2:131.876]
42.89    30.17
57.81    30.69
72.72    32.25
87.64    34.84
102.56   38.48
117.48   43.15
132.39   48.85
147.31   55.60
162.23   63.38
177.14   72.20
192.06   82.06
206.98   92.96
221.89   104.89
236.81   117.87
251.73   131.88
0 0
# 0 0 GLP 4
[GL-PARAB: 5--> X1:42.891 Y1:30.174
X2:261.728 Y2:131.876]
42.89    30.17
58.52    30.69
74.15    32.25
89.78    34.84
105.42   38.48
121.05   43.15
136.68   48.85
152.31   55.60
167.94   63.38
183.57   72.20
199.20   82.06
214.83   92.96
230.47   104.89
246.10   117.87
261.73   131.88
0 0
# 0 0 GLP 5
```

Final Stage Hohewieße

[DONNEE]
Version=Talus WinVersion2010
Titre = hohewiese
nb_couche =6
nb_glissement =12
nappe = oui
nb_survert =0
nb_surhori = 0
acc_sismVert = 0
acc_sismHori = 0
prec_iter = .01
num_couche_surpression = 5
Multi color glissement=1
Decalage profil=0.0
Decalage profilY=0.000
[C-COUCHE 1 : COUCHE 1]
0.2 27 1.9 1.9 0 0 1
0 262
100 262
101 280
287 280
0 0
235 280 Clay ore (Stiff)
[C-COUCHE 2 : COUCHE 2]
2.5 17.5 1.9 1.9 0 0 1
101 280
108 280
125 290
287 290
0 0
235 290 Clay ore (Loose)
[C-COUCHE 3 : COUCHE 3]
0 40 1.9 1.9 0 0 1
20 262
90 285
100 290
125 290
0 0
35 270 Gravel Embankment
[C-COUCHE 4 : COUCHE 4]
0.5 22.5 1.9 1.9 0 0 1
125 290
190 311
235 305
287 305
0 0
235 305 Lean Clay
[C-COUCHE 5 : COUCHE 5]
0 15 1.9 1.9 0 0 1
190 311
204 315
240 312
287 312
0 0
235 312 Organic Clay
[C-COUCHE 6 : COUCHE 6]
9 19 1.9 1.9 0 0 1
204 315
213 318
221 318
228 321
234 321
245 317
287 317
0 0
235 317 Silt
[SXX-surV]
1 5 43.9 20 20 40 40 1
[SXX-surV]
2 43.9 140.9 20 0 40 60 1
[N-nappe]
0 261
60 261
125 280
135 305
190 305
204 305
213 305
228 308
234 308
245 306
287 306
0 0
245 316 Water
[GL-C 0--> Cx:125.845 Cy:362.661
R:100.05]
60 286
90 284
97.97 283.49
118.63 281.49
139.61 280.49
160.48 281
187.74 284.05
198.08 293.43
207.01 304.16
214.36 316.03
219.99 328.80
0 0
0 0 GLx
[GL-C 1--> Cx:132.68 Cy:396.563
R:134.474]
60 286
90 284
97.97 283.49
118.63 281.49
139.61 280.49
160.48 281
203.65 282.34
218.86 293.33
232.39 306.33
243.98 321.09
253.40 337.31
0 0
0 0 GLx
[GL-C 3--> Cx:126.247 Cy:366.162
R:101.141]
60 286
90 284
97.97 283.49
118.63 281.49
139.61 280.49
160.48 281
189.20 287.00
199.61 296.54
208.58 307.42
215.96 319.45
221.58 332.39
0 0
0 0 GLx
[GL-C 4--> Cx:133.082 Cy:401.425
R:136.888]
60 286
90 284
97.97 283.49
118.63 281.49
139.61 280.49
160.48 281
206.04 285.60
221.45 296.88
235.14 310.20
246.84 325.29
0 0
0 0 GLx
[GL-C 6--> Cx:126.649 Cy:369.881
R:102.441]
60 286
90 284
97.97 283.49
118.63 281.49
139.61 280.49
160.48 281
190.84 290.05
201.33 299.76
210.36 310.83
217.76 323.06
0 0
0 0 GLx
[GL-C 7--> Cx:133.485 Cy:406.631
R:139.637]
60 286
90 284
97.97 283.49
118.63 281.49
139.61 280.49
160.48 281
208.68 288.97
224.32 300.58
238.20 314.25
250.04 329.73
0 0
0 0 GLx
[GL-C 9--> Cx:127.052 Cy:373.848
R:103.982]
60 286
90 284
97.97 283.49
118.63 281.49
139.61 280.49
160.48 281
180.83 284.85
192.69 293.20
203.28 303.12
212.38 314.42
219.82 326.87
0 0
0 0 GLx
[GL-C 10--> Cx:133.887 Cy:412.23
R:142.771]
60 286
90 284
97.97 283.49
118.63 281.49
139.61 280.49
160.48 281
194.19 282.82

211.61 292.47
227.52 304.45
241.61 318.53
253.60 334.44
0 0
0 0 GLx
[GL-C 12--> Cx:127.454 Cy:378.102
R:105.802]
60 286
90 284
97.97 283.49
118.63 281.49
139.61 280.49
160.48 281
182.76 287.91
194.78 296.48
205.48 306.64
214.67 318.20
222.15 330.92
0 0
0 0 GLx
[GL-C 13--> Cx:134.289 Cy:418.282
R:146.35]
60 286
90 284
97.97 283.49
118.63 281.49
139.61 280.49
160.48 281
197.10 286.09
214.88 296.12
231.10 308.53
245.43 323.07
0 0
0 0 GLx
[GL-C 15--> Cx:127.856 Cy:382.687
R:107.944]
60 286
90 284
97.97 283.49
118.63 281.49
139.61 280.49
160.48 281
171.63 284.02
184.94 291.07
197.13 299.91
207.98 310.36
217.27 322.21
224.81 335.24
0 0
0 0 GLx
[GL-C 16--> Cx:134.691 Cy:424.858
R:150.446]
60 286
90 284
97.97 283.49
118.63 281.49
139.61 280.49
160.48 281
180.86 282.49
200.34 284.49
218.54 299.95
235.11 312.83
249.72 327.90
0 0
0 0 GLx